CONTROLLED GROWTH AND PROPERTY MEASUREMENT OF ONE-DIMENSIONAL OXIDE NANOSTRUCTURES FOR ENERGY APPLICATIONS

by

Tao Sheng

A dissertation submitted to the faculty of
The University of North Carolina at Charlotte
in partial fulfillment of the requirements
for the degree of Doctor of Philosophy in
Optical Science and Engineering

Charlotte

2015

Approved by:

____
Dr. Haitao Zhang

____
Dr. Tsinghua Her

____
Dr. Michael Fiddy

____
Dr. Stuart Smith

____
Dr. Yu Wang

ABSTRACT

TAO SHENG. Controlled growth and property measurement of one-dimensional oxide nanostructures for energy applications. (Under the direction of DR. HAITAO ZHANG)

Transition metal oxides (TMOs) exhibit rich structures and useful properties and could be used in applications of solar energy harvesting (*e.g.*, photoelectrochemistry, photocatalysis, and photovoltaics) and energy saving (*e.g.*, electrochromism and photochromism). Nano-engineering of these TMOs could produce a variety of nanostructures, modify the electronic and optical properties, and potentially enhance the performances and extend their applications into new regimes. To fully harvest the advantages of these materials, a scalable growth method and a comprehensive understanding towards the growth-structure-property relation must be established. This doctoral study focused on one-dimensional (1D) nanostructures of tungsten trioxide (WO_3) and molybdenum trioxide (MoO_3). This dissertation synthesized 1D WO_3 and MoO_3 nanostructures using the chemical vapor deposition (CVD) approach, characterized the morphologies and structures, and measured the optical properties of the as-prepared nanostructures. This dissertation consists of three main parts, each centering on WO_3, MoO_3, and WO_3-WS_2, respectively. Systematical investigation of the WO_3 nanostructure prepared by the CVD method with tungsten powders as precursor led to the following accomplishments: *a*) the discovery of $Na_5W_{14}O_{44}$ nanowires (NWs); *b*) a knowledge of the delicate role of sodium in tungsten source powders; and *c*) a seeded growth method to produce high quality WO_3 NWs. Enlightened by the intricate interactions between sodium content and tungsten oxide, this dissertation extended the vapor-liquid-solid strategy in to MoO_3 1D nanostructure growth and discovered two morphologies of MoO_3: long nano-belts and micro-towers. Careful observation in extensive experiments identified the catalytic role of sodium hydroxide during the growth of MoO_3 and readily proved that the catalytic behavior also exists with other alkali metal compounds. The third part of this work moved the investigation center from growth to structure and property characterization. A novel integrated structure-property (transmission electron microscopy-Raman spectroscopy, TEM-Raman) study was performed on WO_3-WS_2 core-shell NWs, allowing for the observation of high resolution TEM imaging, Raman spectroscopy, and photoluminescence spectroscopy on individual nanowires. The TEM-Raman combined results further illustrated that the profiles of resonant Raman spectra exhibit strong dependence on the wall number of WS_2. This Raman fingerprints can provide a rapid approach for the optical identification of few-walled WS_2 tubular structures.

In summary, this study explored methods for controlled and scalable growth of 1D WO_3 and MoO_3 nanostructures based on both vapor-solid and vapor-solid-solid approaches, characterized the structure-property relations to rationalize nanostructure synthesis for energy applications, and presented preliminary results for the device fabrications using the WO_3 and MoO_3 nanostructures.

ACKNOWLEDGMENTS

Studying in UNC Charlotte has been an unique and rewarding experience for myself, which I shall recall frequently for a long time to come. So I am grateful to all the people here I have spent time with. Dr. Haitao Zhang has been an excellent advisor to me. I enjoyed the time learning a new set of skills, discussing research questions, and obtaining important life lessons from him. I thank Dr. Davies for the help she gave when I joined the Optical Science and Engineering program; I thank Dr. Terry Xu for allowing me to work in her lab since 2012, within which I finished most of the crystal growth work. I also thank Dr. Yong Zhang for the access to Raman instrument in his group, without which my research would be seriously diminished. I appreciate the financial supports of GASP in UNC Charlotte, the research assistantship from National Science Foundation (DMR-1006547), and the teaching assistantship from Physics and Optical Science department. I also appreciate the Department of Mechanical Engineering and Engineering Science and the Center for Optoelectronics and Optical Communications at UNC Charlotte for supports in multiuser facilities. I would also like to thank all my friends and/or research partners I have met in Charlotte: Dr. Bob Cao, Dr. Jianwei Wang, Liqin Su, Henan Liu, Jinghua Ge, Siang Yee Chang, Zhe Guan, and Youfei Jiang.

Most important, I am grateful to my parents who support my decisions as always.

TABLE OF CONTENTS

LIST OF FIGURES

LIST OF TABLES

LIST OF ABBREVIATIONS

BSE	backscattering electron
CB	conduction band
CBM	conduction band minimum
CCD	charge coupled device
CDW	charge density wave
CEBD	convergent electron beam diffraction
CL	cathodoluminescence
CNT	carbon nanotube
CS	crystallographic shearing
CVD	chemical vapor deposition
DP	diffraction pattern
DRS	diffuse reflection spectroscopy
E-beam	electron beam
EC	electrochromic
ECD	electrochromic device
EDX	energy dispersive X-ray spectroscopy
EELS	electron energy loss spectroscopy
FL	few-layer
FWHM	full width at half maximum

HRTEM	high resolution TEM
IPA	isopropyl alcohol
KMT	Kubelka-Munk theory
LA	longitudinal acoustic
LBM	layer breathing mode
MFP	mean free path
ML	monolayer
NHE	normal hydrogen electrode
NT	nanotube
NW	nanowire
PL	photoluminescence
PVD	physical vapor deposition
SAED	selected area electron diffraction
sccm	standard cubic centimeters per minute
SE	secondary electron
SEM	scanning electron microscopy
SERS	surface-enhanced Raman scattering
SWNT	single-walled nanotube
TA	transverse acoustic
TEM	transmission electron microscopy

TMDC	transition metal dichalcogenide
TMO	transition metal oxide
VB	valence band
VBM	valence band maximum
VLS	vapor-liquid-solid
VS	vapor-solid
VSS	vapor-solid-solid
XRD	X-ray diffraction

CHAPTER 1: INTRODUCTION

1.1 Background and Motivation: Nanomaterials for Energy Applications

Transition metals generally refer to any element in the d-block of periodic table, and transition metal oxides (TMOs) mean the chemical compounds that consist of at least one transition metal element and oxygen. Similarly, transition metal dichalcogenides (TMDCs) are compounds that combine at least one transition metal with chalcogen elements from group VIA (S, Se, Te, Po).[1] Both tungsten (W) and molybdenum (Mo) belong to Group VIB transition metal with outer shell electrons configuration as $4d^5 5s^1$ and $5d^4 6s^2$, respectively. This study focused on the following three materials: molybdenum oxide (MoO_3), tungsten oxide (WO_3), and tungsten disulfide (WS_2).

The two metal oxides, MoO_3 and WO_3, have been studied for decades for energy related applications, e.g., photoelectrochemistry,[1] photocatalysis,[2, 3] photovoltaics,[4] and electrochromism.[5, 6] WS_2 has also been investigated in various morphologies, i.e., thin films, nanotubes, and 2D atomic layers recently. WS_2 exhibits potentials in solar cells,[7] water cleavage,[8] and field effect transistors.[9] Heterostructures formed between TMO and TMDC provide another degree of freedom to fine tune the band structures, which could enhance the solar energy harvesting performances.[10]

---

[1] Oxygen also belongs to group VIA, but is often treated separately.

1.1.1 Electrochromism for Energy Saving

Commercial buildings in U.S. consumed approximately 35% of the electricity usage.[11] And traditional windows in the buildings account for up to 40% of the total heating, cooling, and lighting consumption, which is of low energy efficiency. Smart window is an energy efficient answer by allowing for separate control of the visible and NIR illumination/transmission. Several solutions have been proposed in both academia and industry to develop smart windows, including liquid crystal, suspended particles, and electrochromic materials.[12] Previous efforts show the electrochromic materials is the most promising component in smart window design in comparison to other options,[13] in that it requires little power to switch between bleaching and coloration status (changing the optical transmission) and the failure mode is being clear instead of opaque, which is of great importance in commercial applications.

Electrochromism, where the optical property of the materials is changed upon applying low DC voltage (<5 V), has been found in numerous inorganic and organic substances, e.g., V_2O_5, WO_3, and NiO for the former group, and prussian blue and polyaniline for the latter one. This study covers two inorganic metal oxides, WO_3 and MoO_3. Detailed electrochromic mechanism will be discussed in Chapter 1; a brief review of electrochromism study on WO_3 is presented here.

Prototype ECD usually consists of a stacked configuration, as shown in Fig. 1a. Typical transmission spectra of the prototype ECD based on WO_3 thin film are shown in Fig. 1b,[12] where optical transimission T in bleaching and coloration states exhibit dynamic changes. The reflectance spectra of WO_3 ECD strongly depends on the device design.[14] As to the

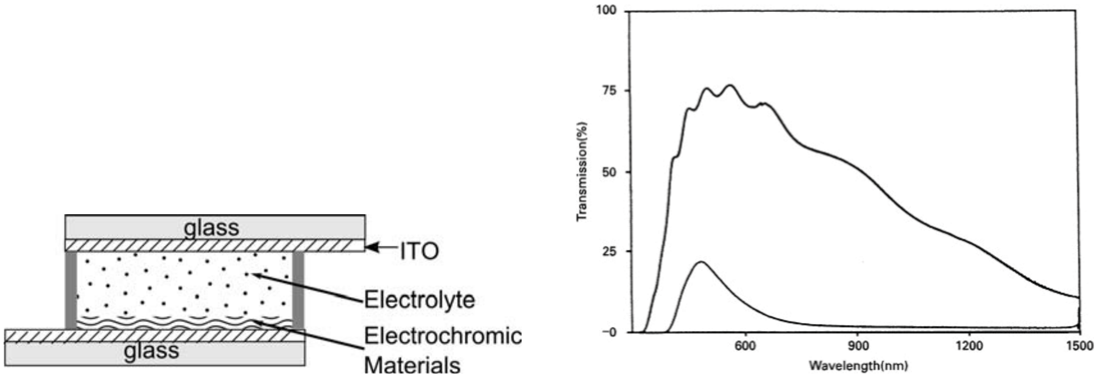

(a) (b)

Figure 1: ECD prototype and its transmission properties. (a) Schematic diagram of electrochromic device (ECD), and (b) optical transmission in color and bleached states, reproduced from [12]

absorption, it was deduced that the infrared part was absorbed to a large extent, which was radiated again. Assuming the emission property of ECD being that of the blackbody, Fig. 2 displays the wavelength distribution of spectral radiance, where the spectra span from 3 μm up to 30 μm, with peaks around 8 $\sim$ 10 μm. Further thermal engineering is needed to better regulate this infrared radiation.

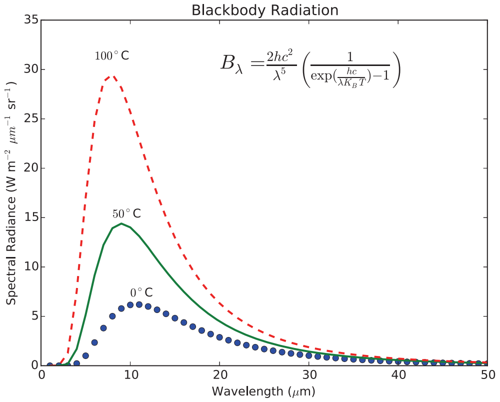

Figure 2: Spectral radiance of blackbody at 0, 50 and 100 °C predicated by Planck's Law.

The successful deployment of ECD based on WO_3 relies on several factors:[15]

- low cost transparent conductive materials with low resistivity;
- low cost ion electrolyte of poor electron mobility;

- high yield growth method of WO_3 and integration with other manufacturing process;
- life cycle $> 10^5$ for long time outdoor usage.

The deficiency of ECD based on amorphous or polycrystalline WO_3 film was the accumulation of ions at the film surface preventing further intercalation,[16] which led to low coloration efficiency and short life time. In contrast, nano-structured single crystalline WO_3 could bypass this limitation, as detailed in Sec. 1.1.3.

1.1.2 Photocatalysis for Solar Energy Harvesting

Photocatalytic activity occurs at the semiconductor-electrolyte interface where charge carriers (electrons or holes) are produced in a semiconductor illuminated by photons of energy exceeding that of the band gap, then drift and generate free radicals, i.e. OH·, enabling further reactions. A much desired goal is water splitting using photocatalytic activity from solar energy. Semiconductor is in the center of photoelectrochemical cell design for water splitting, e.g. the band gap should be within 2.0 ~ 3.0 eV, and conduction band (CB) edge should be more negative than reduction potential of H^+/H_2, whereas the valence band (VB) top should be more positive than the oxidation potential of H_2O/O_2.[17, 18] The valence band holes (h^+) oxidize water to oxygen, and conduction band electrons propel hydrogen generation, as depicted in Eq. 1.

$$4h^+ + 2H_2O \rightarrow O_2 + 4H^+ \tag{1a}$$
$$4H^+ + 4e^- \rightarrow 2H_2 \tag{1b}$$

As shown in Fig. 3, WO_3 has CB edge positioned slightly more positive than the reduction potential of H^+/H_2 versus normal hydrogen electrode (NHE) and VB edge much more positive than the oxidation potential of H_2O/O_2; therefore, photo-cleavage of water cannot

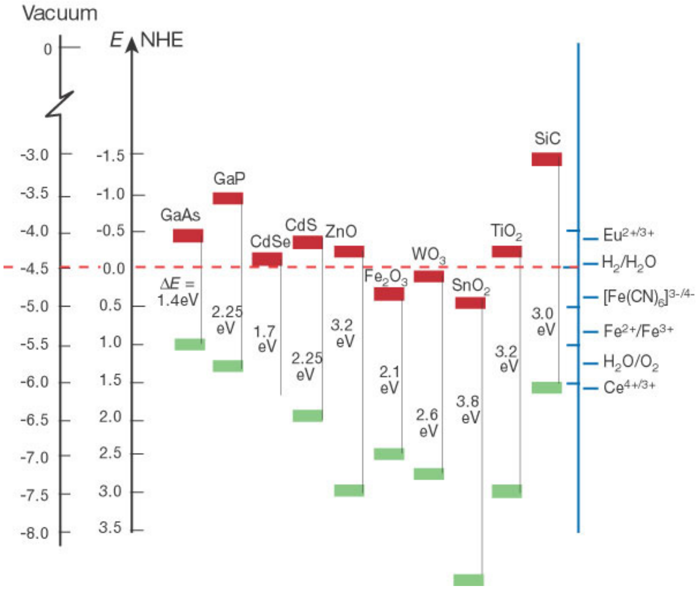

Figure 3: Band position of WO_3 in contact with aqueous electrolyte at pH 1. Reproduced from Ref.[19]

be accomplished by WO_3 alone. Nevertheless, a tandem cell approach by WO_3 film and dye-sensitized TiO_2 has been demonstrated with an efficiency of 4.5%.[20] It is worth noting that green plants also have two photosynthetic systems connected in series, one for oxidation of water into oxygen and the other for fixation of carbon dioxide. Moreover, favorable oxygen evolution of WO_3 has brought good performance in degradation of organic compounds.[2, 21, 22] The formation of long-lived holes is recognized as a key requirement.[23] Besides, WO_3 is remarkably stable in acid ($pH < 5$), making it a significant candidate for treating water pollutants caused by organic acids.[24]

1.1.3 Advantages of Nano-Engineering

Several differences are noted between bulk materials and nanostructured materials. Nanostructured materials possesses gigantic surface area in comparison to its bulk counterpart of the same volume; for instance, given 1 gram SiO_2 nanoparticles in diameter of 10 nm and assuming the density being 1.2 g/cm^3, the estimated surface area will be 1×10^6 cm^2.

This huge surface-to-volume ratio is generally a favorable feature for catalytic reactions, which predominately occur on the surface.[25] Other features due to nanostructure include *a*) surface energy state, thereby band structure modification; *b*) quantum confinement effect; and *c*) different charge-separation and transport mechanism. Overall, these features usually promise enhanced performance.

In regarding to the contents of this study, electrochromic applications based on TMO nanowires will benefit from the reduced diffusion depth by eliminating the deficiency of ions accumulation in amorphous oxide thin film devices, which in turn leads to shorter response time and higher coloration efficiency.[26, 27] And photocatalytic applications using TMO nanostructures could harvest the huge surface area on which unsaturated bonds reside, thereby enabling a much higher efficiency.[10, 28, 29] To fully use nano-engineering, one must just be as aware of the limitations as one is of its advantages; for example, an obvious disadvantage is the difficulty of device fabrication using nanomaterials due to the size and requirements of new integration processes. There also exist some uncertainty as to the energy band modification present in nanostructures, which could be either useful or not depending on the application.[18]

1.2 Scope and Dissertation Outline

To fully harvest the advantages of these TMO and TMDC one-dimensional nanomaterials, a scalable growth method and a comprehensive understanding of the growth-structure-property relation must be established in the first place. This study primarily focuses on the WO_3 and MoO_3 nanostructure synthesis, the growth mechanism study, crystal structures characterization, and optical properties measurement.

The materials studied in this dissertation are tungsten oxides (WO_3), molybdenum oxides (MoO_3),and tungsten disulfide (WS_2). Experimental tools will be mentioned in Chapter 2, including the CVD apparatus and substrate treatments for growth, electron microscopes and optical spectrometers for characterization. Chapter 3 is devoted to tungsten oxides (WO_3) and sodium tungsten oxides ($Na_5W_{14}O_{44}$) nanowires, where the role of sodium in metallic tungsten precursors are thoroughly investigated; a potentially scalable growth method is also developed. Chapter 4 turns to molybdenum oxide (MoO_3) growth using alkali metal compounds as catalysts. In Chapter 5, a heterostructure based on WO_3 nanowires (NWs) is studied. Emphasis will be placed on the characterization of individual WO_3-WS_2 core-shell NW. This dissertation is concluded with summary and future work.

CHAPTER 2: EXPERIMENTAL TOOLS

In this study, the nanostructures were grown in a home-built chemical vapor deposition (CVD) system and characterized using both electron microscopy and optical spectroscopy methods, including scanning electron microscopy (SEM), X-ray diffraction (XRD), energy dispersive X-ray spectroscopy (EDX), transmission electron microscopy (TEM), Raman and UV-Vis spectroscopy. A detailed description is given to the CVD system. General sample and substrate preparation methods are also briefly introduced. For mature processes and techniques, the contents are limited to the extent where experienced material researchers could repeat the experiments performed here. Some details are mentioned in particular to perform the nanostrucutres characterization in a proper way.

2.1 Synthesis Equipments and Processes

2.1.1 Home-built Chemical Vapor Deposition System

The syntheses were accomplished in a home-made hot-wall CVD system. The reaction chamber and a schematic drawing of whole system can be visualized in Fig. 4. The reaction chamber consists of fused silica tube and a thermal furnace. The furnace is made by two semi-cylindrical ceramic fiber heaters (WATLOW, Inc.) with power density from 0.8 to 4.6 W cm^{-2}. Quartz tube (Quartz Sci, Inc.) of 1 inch diameter is inserted into the furnace serving as the reaction chamber. A mechanical pump is connected to maintain the low pressure environment inside the chamber. The length of heating zone is 6 inch, with 1 inch cooling zone extending outward on each side. Carriers gas argon (Ar) and reactant gas oxygen (O_2)

are regulated by mass flow controllers.

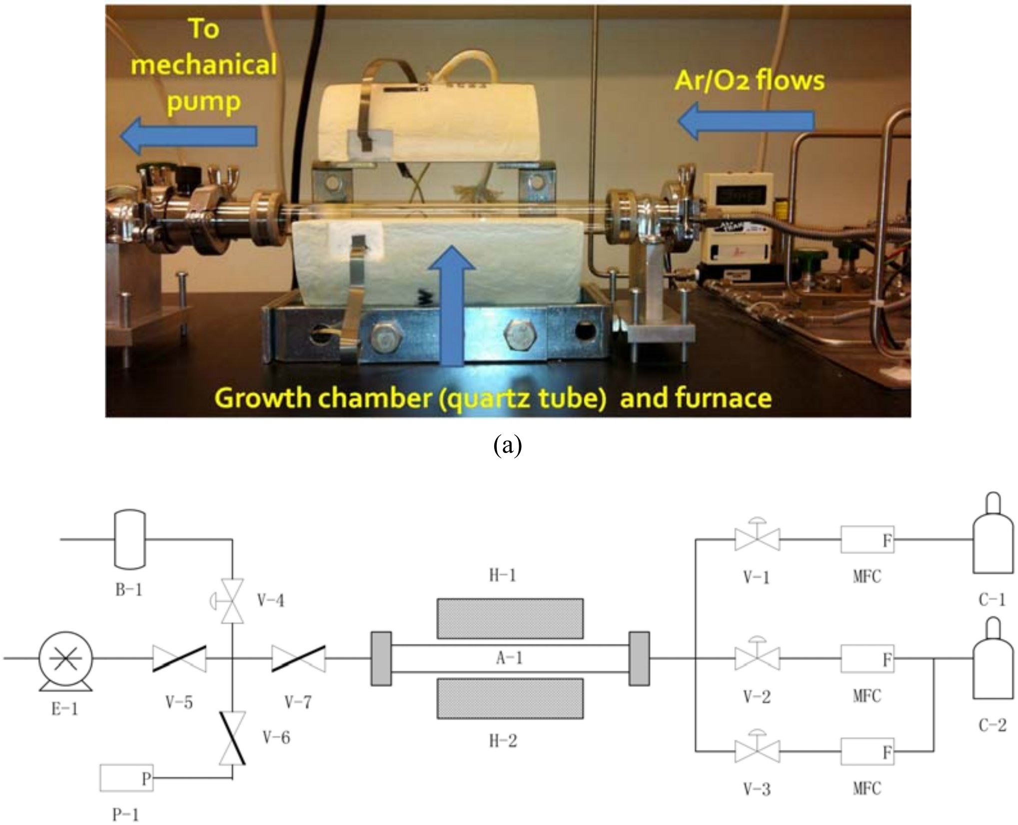

(a)

(b)

Figure 4: Home-built low-pressure chemical vapor deposition system. (a) Photograph of reaction chamber. (b) Sketch of CVD system, where A1: quartz tube; B1: bubbler; C1-2: gas cylinders; E1: mechanical pump; H1-2: ceramic heater; MFC: mass flow controller; P1: pressure gauge; V1-4: needle valves; V5-7: butterfly valves.

The controllable parameters of this CVD system include the central heating temperature, the absolute gas flow, amount of source materials, and the location of substrates. The operation capability is summarized in Table 1. The heating temperature T profile measured at different settings in ambient environment is shown in Fig. 5. There exists a uniform heating zone in the center area, spanning over about 2 inch; then T descends gradually within the 6 inch heating zone and decreases rapidly at the rest part. In this study, a zero position referred as 0 inch is defined at the upstream edge of reaction chamber covered by the

Table 1: Home-built CVD parameters

			Flow	
	Temperature	Pressure	Ar	O_2
	°C	mTorr	sccm	sccm
Range	RT - 1100	10 mTorr -1 atm	0 - 100	0 - 30
Resolution	±1	correlated to flow	1	0.1

furnace. In typical growth, the substrates are positioned just outside the downstream heating zone, since within this region the vapor of growth species undergoes a rapid temperature gradient, and precipitation occurs. After the chamber is heated to target temperatures, the source material (tungsten and molybdenum powders) placed in the furnace center is oxidized and evaporated. The growth species, transported by carrier gas, bombard both substrate and chamber wall. Some will be adsorbed by the substrate and become adatoms, while some may remain as gas molecules, waiting for another event. On the hot substrate, adatoms diffuse and do not settle down until finding an appropriate location where equilibrium is favored. Detailed growth conditions will be introduced in the corresponding experimental

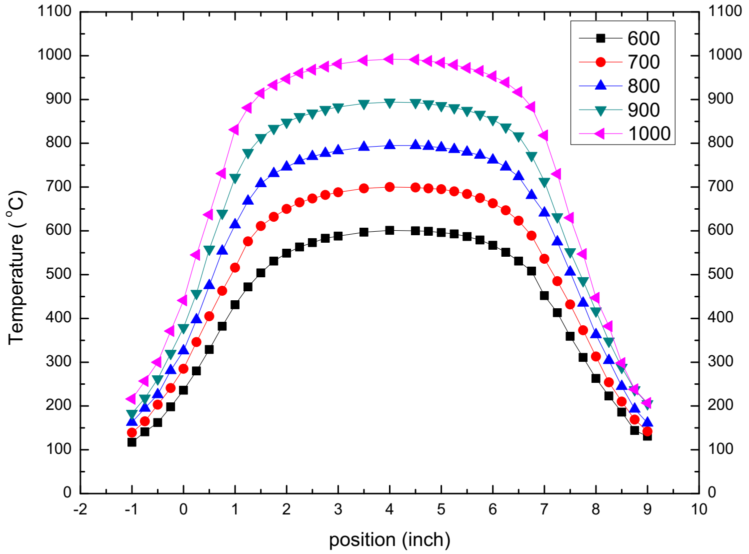

Figure 5: Temperature profile of home-built CVD in ambient environment.

section of Chapter 3, 4, and 5.

2.1.2 Substrates Treatments

Silicon (Si) and 1 μm silicon dioxides on Si wafer (SiO_2-Si) (University Wafer Inc.) were primarily used. Other substrates were also employed, i.e. Mica[2], glass (Fisher Scientific, microscope slide, 12-549),[3] and stainless steel. Si and SiO_2-Si substrates were first cut into rectangular pieces and then ultrasonically cleaned (Branson 1510R-MTH) with acetone and alcohol for about 15 min, each followed by blow-drying with nitrogen gas. After solution cleaning, the substrate surface is usually hydrophobic. Depending on the specific experimental requirement, a hydrophilic surface may be required. A plasma cleaner (Kurt J Lesker, Plasma-Preen 862) was used to render a hydrophilic Si surface, where reaction among e, O^+, $O_2{}^+$, O^{--},O_2 occurs, and OH-terminated surface followed.[30] The treatment proceeds at 2 Torr O_2 for 3 min. Glass substrate cleaning procedure was the same as that of Si. Mica substrates were cleaved right before the growth without extra cleaning steps. In addition, substrates can be coated with a thin layer of metal before growth. This process will be covered in Sec. 2.1.3.

2.1.3 Magnetron Sputtering

Sputtering, a process in which atoms are ejected from a solid target material by bombarding it with energetic particles, is a well established physical vapor deposition (PVD) process with a high degree of controllability. The high energy and controllable parameters of sputtering can result in the growth of well-structured and crystalline films. Further, sputtering can be easily implemented as a roll-to-roll process for large-scale manufacturing. It is widely

---

[2] $K(Al_2)(Si_3Al)O_{10}(OH)_2$

[3] Typical composition is 72.6% SiO_2, 0.8% B_2O_3, 1.7% Al_2O_3, 4.6% CaO, 3.6% MgO and 15.2% Na_2O

utilized for deposition of WO_x in industry.

In this work, magnetron sputtering (Denton Vacuum Desk IV) was used to coat thin layer of metals onto cleaned substrates. As shown in Fig. 6, the metal target is the cathode, and the specimen is anode. A dc voltage is applied to ionizes the argon gas, and a permanent magnet behind the target focuses the gas plasma onto the target and also deflect electrons from the sample. These ions are then accelerated to bombard the target foils, knocking out active atoms which subsequently deposit onto the substrates. Ar^+ ions are accelerated to target foils. The pressure of Ar^+ has two functions: to sputter off the target ions and to influence the mean free path (MFP). These collisions between target ions and Ar^+ lead to almost all arrival angles, thus uniform coverage. The sputtering yield is number of target ions released per ions hitting on target. If Ar^+ ion energy is less than 100 eV, the yield is zero; if larger than 10 keV, implantation of Ar^+ into target foils occurs. Usually, yield between 1 and 2 is desired. The MFP in sputtering is on order of 3 cm (assuming pressure of 30 mTorr). With

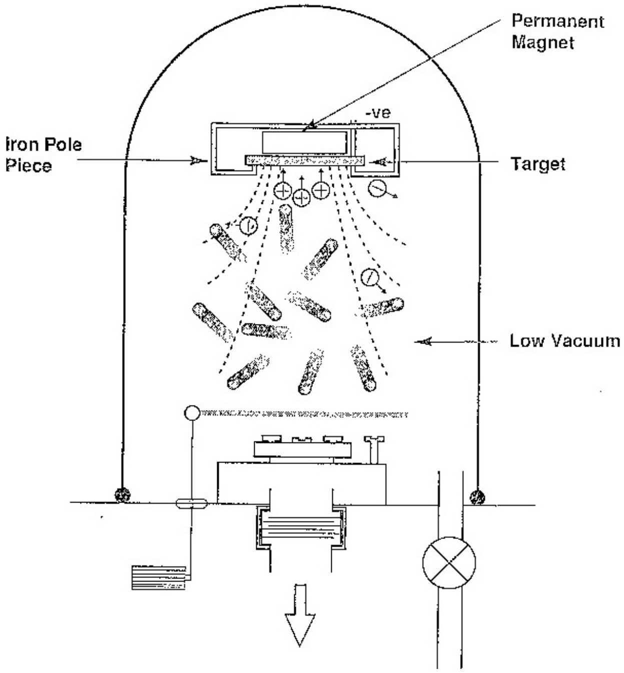

Figure 6: Schematic drawing of magnetron sputtering system. Reproduced from Ref.[31]

source-to-substrate distance as 5 cm, average number of collisions is about 5/3~2.

A common purpose of sputter coating is to facilitate SEM observation. Pure gold target can be used for low-magnification studies; a platinum target will deliver satisfactory result for medium-to-high resolution studies. For high-magnification studies, a target of gold-palladium alloy is a good choice because the epitaxial growth is limited.[31]

2.2 Characterization Tools

2.2.1 Scanning Electron Microscopy (SEM)

The SEM instrument used in this study is JEOL JSM-6480. The electron beam (E-beam) source is a tungsten filament heated at about 2800 K.[32] The acceleration voltage can be up to 30 kV. After acceleration, electron beam strikes the sample mounted on specimen stage producing rich signals, as illustrated in Fig. 7. Depending on the energy and scattering angle, the out-coming electrons from specimen can be grouped into backscattering electron (BSE) and secondary electron (SE), respectively. SE is generated from the emission of valence band electrons. And due to the limited energy (< 50 eV), the emission from deep region is mostly

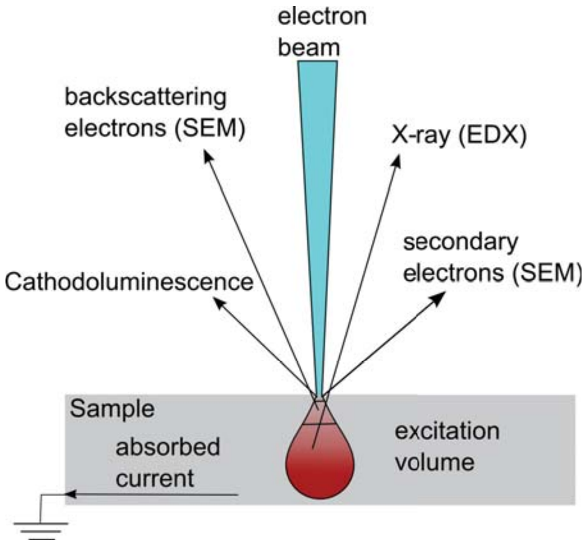

Figure 7: Schematic drawing of electron-matter interactions in SEM.[33] Some processes are not shown, such as Auger emission.

absorbed again; only those electrons that are at the vicinity of specimen surface can escape. Hence, the SE image is topographical sensitive. The emission efficiency is strongly affected by the geometry (tilting angle of specimen surface) and voltage potential (charging effect), so does the contrast in SE image. On the other hand, backscattered electron could have large energy close to that of incident E-beam. The scattering cross section strongly depends on atomic number Z, thus allowing for the compositional analysis. The X-ray emission stems from inner shell transition of the constitutive atoms, and cathodoluminescence arises from band gap transition.

In this study, secondary electron images were mainly used to reveal the morphology of the samples. Unless otherwise noted, the SEM images were acquired using 10 kV acceleration voltage, 10 mm working distance, and 30 spot size.

Charge effect could arise on the samples grown in this study, leading to anomalous contrast on the images. Several measures could be taken to alleviate this adverse influence, including adjusting the acceleration voltage, tilting the specimen, and coating a thin layer of metal. Sometimes when an area is scanned for a long time at high magnification, the surrounding region could appear brighter after switching to a lower magnification. This is a sample contamination, due to the E-beam induced polymerization and deposition of hydrocarbon molecules in the vicinity of that smaller area.

2.2.2 Energy Dispersive X-ray Spectroscopy (EDX)

Energy dispersive X-ray spectroscopy provides compositional information attaining to the studied sample because of the characteristic X-ray emission from each constitutive element. EDX unit is usually attached to another electron microscopy, SEM or TEM. In this study, the SEM-attached EDX was primarily used. The X-ray detector (INCA 7573-M, 10 mm^2 Si cooled by liquid nitrogen) is equipped with a super thin window enabling light element detection, such as boron. Typical working parameters of EDX detection in this study include 20 kV acceleration voltage, 10 mm working distance, and 60 s analysis time.

To obtain quantitative results on EDX spectra, special attentions should be paid to the following aspects: *a*) elemental distribution in an X-ray generation area is uniform; *b*) the specimen surface is flat; *c*) the electron beam enters perpendicular to the specimen; and *d*) a reference sample consisting of identical elements and known ratio is used. Even for qualitative analysis, ambiguity exists when the K lines of lighter elements overlap with L lines of heavier elements; for instance, Na-K_α (1.041 keV) interferes with L_α lines of Zn (1.009 keV) and Cu (0.928 keV). Overall spectra and growth conditions should be weighted against possible wrong assignment.

2.2.3 X-ray Diffraction (XRD)

Crystal structures of the as-synthesized specimens in this study were characterized using PANXpert Pro MRD with Cu Kα_{avg} radiation at λ=1.5418 Å. The high energy photon flux (E = 1239.8/0.15148 = 8184.5 eV) was generated by using accelerated electron beam from tungsten filament to bombard Cu target. The $\theta - 2\theta$ configuration was primarily used, as shown in Fig. 8. When striking onto the crystal, these photons are scattered by the lattices. Since the wavelength of X-ray is similar to the lattice spacing, the scattering events interact coherently. Only at specific angles constructive interference occurs, and a diffraction peak registers when the detector is scanned across that angle. The as-synthesized specimens were mounted onto diffractometer in a way that the X-ray will illuminate interested region

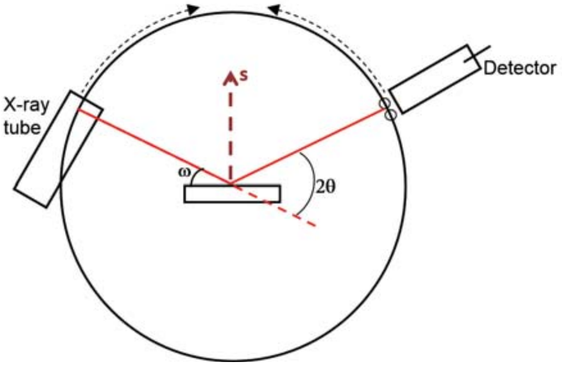

Figure 8: Bragg-Brentano geometry used in XRD configuration.[33]

during the whole scanning. Typical settings used were summarized in Table 2. The 1D

Table 2: XRD settings used in this study

Name	Value	Name	Value
Voltage	45 kV	Current	40 mA
Divergence slit	1/32°(alignment) 1/2°(scanning)	Receiving slit	Parallel collimator
Soller slit	0.04 rad	Collimator	Parallel plate 0.27 rad
Scan range	10 ~ 65°	Step size	0.02°

nanostructures in this study usually grew with preferred orientation; therefore, they cannot be treated as powders. The interpretation of XRD patterns could become difficult somehow. Two possible approaches were suggested to bypass this difficulty: one is using grazing angle XRD which could reveal in-plane domain sizes and orientations;[34, 35] the other is combining XRD with alternative techniques, such as Raman and TEM. The latter approach was pursued in this work.

2.2.4 Transmission Electron Microscopy (TEM)

TEM qualifies as a powerful and versatile tool for material characterization. Akin to the electron-materials interaction introduced in Sec. 2.2.1, various signals are generated when the thin specimen is radiated by electron beam. Besides the selected area electron diffraction (SAED) pattern and high resolution TEM (HRTEM) imaging, other TEM based techniques include convergent electron beam diffraction (CEBD), EDX, electron energy loss spectroscopy (EELS) and cathodoluminescence (CL), etc; therefore, TEM is essentially a signal-generating and detecting tool.[36] Fundamental physics of electron scattering is needed to obtain a comprehensive understanding of these TEM related techniques, and only a brief summary is given here.

Electron scattering is dictated by Coulomb interaction, and can be characterized by the following four aspects: the cross section (scattering probability), differential cross section (scattering angle), mean free path, and inelastic or elastic scattering. The cross section σ in m^2, which when divided by area of targeting atom, represents a probability that scattering event will occur. Differential cross section for an isolated atom is

$$\frac{d\sigma}{d\Omega} = \frac{1}{2\pi \sin\theta} \frac{d\sigma}{d\theta}$$

where 2θ is scattering angle in radians, Ω is solid angle in steradians (sr), and θ is half of the scattering angle. The total cross section is just σ times atom numbers in unit volume. The mean free path is the inverse of σ_{total}, that is $\lambda_{MFP} = 1/\sigma_{total}$.

The spatial distribution of scattering is observed as contrast in images, and angular distribution is viewed in form of diffraction patterns. The positions of diffracted E-beams are determined by size and shape of unit cell, and intensities are governed by distribution, number, and types of atoms in the specimen.

JEOL JEM-2100 TEM with a LaB_6 filament operated at 200 kV was used in this work. A numerical comparison between the scattering events in XRD and TEM is provided to visualize the difference in these two techniques. In both processes, the constructive interference is described by $2d\sin\theta = \lambda$, where d is crystal plane distance, λ is incident wavelength (photon or electron), and θ, again, is half of the scattering angle. Table 3 demonstrates the origin of difference in these two techniques. This small scattering angle determines the way of secondary signal usage in TEM. In analogy to the diffraction-limited resolution in conventional lens optics, the ultimate resolved point distance in TEM should be on the order of electron wavelength used, which is 0.025 Å at 200 kV. Without correction of the spherical aberration, the current resolving power in TEM is on the order of 1.0 Å. The nominal resolution of JEM-2100 is 2.3 Å. Nevertheless, it is much easier to fine tune the power (focal length) of lens in TEM than in conventional optics. This capacity enables other observation approaches that would be rather difficult, if not impossible, to be realized in lens optics, such as generating SAED pattern.

Table 3: Scattering angle difference of Si(111) in XRD and TEM

Si(111) spacing	Source	Wavelength	scattering angle(2θ)
3.135 Å	Cu Kα	1.541 Å	28.45°
3.135 Å	200 kV	0.0251 Å	0.45°

In this study, a JEOL double tilt holder was used to rotate the crystal orientation. TEM images and SAED patterns were acquired using a charge coupled device (CCD) (Gatan, Inc.). EDX spectroscopy was captured by similar Oxford Instrument INCA attachment introduced in Sec. 2.2.2. To make the best out of TEM analysis, one also needs to be aware of the limitations of TEM. Two aspects were pointed out here, namely the small sampling volume and the image interpreting. The former one is inherent and can only be partially overcome by combining TEM with other ensemble characterization tools. As to the latter one, it should be noted that the specimen is usually in focus from top to bottom surface;

therefore the images, diffraction patterns (DPs) and spectra are all averaged through the thickness of specimen. In other words, single TEM image has no depth sensitivity.[36]

2.3 Optical Measurements

2.3.1 Raman Spectroscopy

Raman spectroscopy, a common vibrational spectroscopy, is based on the inelastic scattering of a monochromatic excitation source with photon energy variation range of 100 to 4000 cm^{-1}. This energy difference between incident photon and inelastically scattered photon is closely related to a series of vibrational modes of the sample under observation. Being nondestructive and requiring minimal preparation, Raman spectroscopy is an excellent tools to assess lattice dynamics and to fingerprint species.[37] For instances, characteristic Raman shift can be used to determine material compositions; changes in Raman peak (full width at half maximum (FWHM), frequency shift) are often related to strain; polarization Raman spectra can be used to derive crystal orientation and symmetry.

Some common symbols for symmetry representations are as following:

1. A representation indicates that the functions are symmetric with respect to rotation about the principal axis of rotation.
2. B representations are asymmetric with respect to rotation about the principal axis.
3. E representations are doubly degenerate.
4. T representations are triply degenerate.
5. Subscripts u and g indicate asymmetric (*ungerade*) or symmetric (*gerade*) with respect to a center of inversion.

In this study, Raman measurement was performed using a confocal micro-Raman system

(Horiba Scentific, Labram HR800) with excitation wavelengths at 441, 532, and 632 nm, where the corresponding photon energy is 2.81 eV, 2.33 eV, and 1.96 eV, respectively. For nanowire samples, the laser powers were kept between 0.2 and 0.3 mW, and typical acquisition time was 100 s to avoid possible thermal damage. The spectral resolution is about 1 cm^{-1}, and the depth resolution about 2 μm.

2.3.2 UV-Vis Spectroscopy

UV-Vis-NIR spectrophotometer is a useful tool to obtain optical properties from various samples. Generally speaking, the UV spectrum ranges from 100 nm to 400 nm; visible spectrum spans from 400 nm to 750 nm; and near-IR ranges from 0.75 to 3 μm. Absorption from atmospheric CO_2 becomes significant below 200 nm; therefore 100 to 200 nm region is usually not measured unless some vacuum technique is applied.The cost of fabricating a spectrometer covering the whole NIR region can be quite high. The instrument used in this dissertation (Schimadzu, UV2600Plus) can measure from 220 nm to 1350 nm (5.6 eV to 0.92 eV) with an integrating sphere.

The absorption of materials can be described by Lambert-Beer law: $I = I_0 \exp(-A) = I_0 \exp(-\alpha(\lambda)x)$, where α is the absorption coefficient in unit of cm^{-1}, and x is the optical path in cm. When the sample is in liquid form, it is more convenient to use $A = \epsilon_\lambda C x$, where C is the molar concentration (M = mol/L), and ϵ_λ is the extinction coefficient/molar absorptivity (M^{-1} cm^{-1}). For example, ϵ for methylene blue (MB) is 10^5 M^{-1}cm^{-1} at 660 nm.[38] So by measuring the maximum absorbance of sample with known composition, its concentration can be estimated accordingly.

In the transmission mode, the reflection from materials phase boundary has been compensated with the usage of paired container and solvent. The scattering, however, cannot be eliminated this way. Usually scattering is negligible in molecular disperse media, yet should be considered in colloids or solids when the incident wavelength is comparable to the particle dimension. The size of nanostructures studied in this work is estimated to be 200 to 400 nm after sonication treatment; therefore, scattering effect should be included in the absorbance spectrum.

In fact, there have been ongoing efforts to retrieve particle size profile from the dynamic light scattering, a technique also known as photon correlation spectroscopy. The experimental principle is as following: the sample in liquid solution is illuminated by a laser source and the fluctuations of the scattered light are detected at a known scattering angle θ by a fast photon detector. The fluctuations arise from the Brownian motion of small particles, equivalent to a random variation of scatter distance. By auto-correlation analysis, the decay rate of scattering intensity correlation can be related to the diffusion coefficient of small particles in the solvent.[39] This approach, however, will not be pursued in this work. Instead, the scattering effect of the nanostructured samples is partially circumvented by using diffuse reflection technique.

Diffuse reflectance spectroscopy (DRS) serves as another tool to estimate the sample band gap using Kubelka-Munk theory (KMT).[40] The original KM theory was proposed in 1931[41] and has been popular in the color-related industry, such as painting, pigments, and paper. This method is useful for the analysis of samples of difficultly soluble substances and for samples that will react with the solvents upon being dissolved. It is also particularly applicable when single crystals of the material could not be obtained. Some key points of diffuse reflection spectroscopy (DRS) were recapitulated in this thesis.

The sample is under isotropic diffuse illumination. And the upward flux J and downward flux I are characterized by the KM scattering and absorption coefficients denoted as S and K, respectively; that is

$$\mathrm{d}I = -(K+S)I\mathrm{d}z + SJ\mathrm{d}z, \tag{2}$$

$$\mathrm{d}J = +(K+S)J\mathrm{d}z - SI\mathrm{d}z. \tag{3}$$

Quantities S and K, in unit of percentage of light scattered and absorbed per unit vertical length, have no direct physical meaning. For example, S and K depend on illumination geometry: diffuse or collimated. In the limit of infinite thick sample, the KM equation is given by

$$f(R_\infty) = \frac{(1-R_\infty)^2}{2R_\infty} = K/S, \tag{4}$$

where R_∞ is relative reflectance between sample and standard. In case of dilute species, one can approximate the KM function as $f(R) \propto \frac{\epsilon c}{s}$. When the diffuse scattering condition is fulfilled, K can be related to absorption coefficient α by $K = 2\alpha$. If the scattering coefficient S is fixed with respect to λ, one can then obtain

$$(f(R_\infty)hv)^n \propto (hv - E_g), \tag{5}$$

where n depends on the nature of electronic transition. The diffuse reflection spectroscopy is more proper to characterize nanomaterials because compared with UV-Vis transmission measurement for sample dispersed in liquid media, it takes the scattering effect into consideration. Favorable results have been obtained on the comparison of band gaps using KM model and other methods.[40, 42]

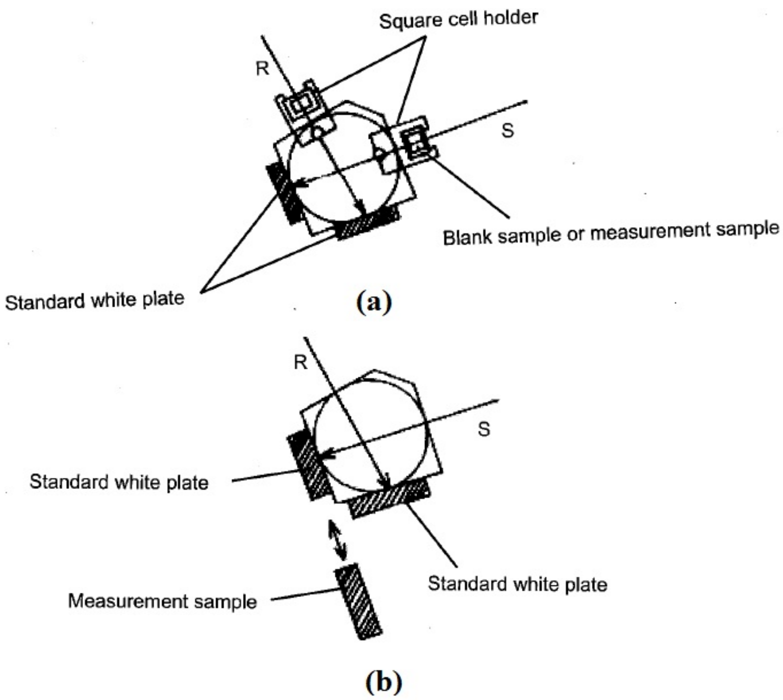

Figure 9: Schematic drawing of (a) UV-Vis and (b) DRS measurement setup adopted from UV2600Plus manual.

In this thesis, UV-Vis and DRS were recorded using Schimadzu, UV2600Plus, with schematic measurement setup shown in Fig. 9. For UV-Vis measurement in transmission mode, the as-synthesized sample was removed from substrates by light sonication (Branson 1510R-MTH, 70W) in ethanol or DI water for 15 second. The dispersion was left for 12 h to enable the possible sedimentation. Then, the dispersion was transferred into one 10 mm quartz cuvette (Thorlabs, W005654) for absorption measurement with another paired cuvette containing pairing liquid only. To carry out diffuse reflectance measurement, an integrating sphere (ISR2600Plus) was used with an incident angle of 0 degree. The baseline reflectance was first recorded with the standard white plate (barium sulfate powder, $BaSO_4$) placed at the exit window on the sample path side, then the target sample was set in for relative reflectance measurement. The $BaSO_4$ powder should be replaced periodically, otherwise the surface might turn yellow. To replace the $BaSO_4$ powder, one should supply new powder into the sample holder for several time, each followed by a compact pressing using the glass rod. Chemical wrapping paper can be inserted between the glass rod and $BaSO_4$ powder to prevent the powder sticking. Nanostructured sample on transparent substrates, i.e. quartz, could be mounted directly with the growth substrate, or ground and spread evenly onto $BaSO_4$ surface.[43]

CHAPTER 3: IMPURITY EFFECTS ON TUNGSTEN OXIDE NANOWIRES

3.1 Introduction

Tungsten oxides (WO_x) is a group of important functional materials with distinctive properties and technology applications. Intense research interest was rekindled by the discovery of electrochromic (EC) effect in 1993.[44] Nano-engineering WO_x bring more possibility and flexibility to its already rich characteristics, therefore resulting in research efforts spanning multiple fields in the scientific community. Besides smart window based on EC effect, tungsten oxides are also well investigated for several other significant applications: photoelectrochemical cell for solar energy conversion and storage, photocatalysis for hydrogen evolution reaction, and chemical and biological sensing based on gasochromic effect. In addition, a few young fields are not thoroughly explored: field emission, optical storage, thermo-electricity, ferro-electricity, and superconductivity. In this chapter, a literature review on tungsten oxides and sodium tungsten oxides is introduced first, with focus on technological applications, crystal structures, and synthesis approaches. Several growth methods were explored in this study to investigate the crystallographic dynamics of tungsten oxides and sodium tungsten oxides nanostructures. The characterization results were presented, followed by in-depth discussion. This chapter is concluded with a brief summary: the impurities effect on the formation of sodium tungsten oxides nanostructures and the seeded growth method for tungsten trioxide NWs of high crystalline quality.

3.1.1 Properties and Applications of Tungsten Oxides

Tungsten trioxide (WO_3) crystallizes in multiple phases. The basic building block is WO_6 octahedra.[4] WO_3 crystal structure consists of WO_6 octahedra joined at their corners, which may be considered as a perovskite structure of $CaTiO_3$ with all Ca^{2+} sites vacant. A representative lattice structure is illustrated in Fig. 10. These distorted WO_6 octahedra adapt different tilting angles in different phases and edge-sharing octahedra also arise.

The temperature-dependent phase transition and corresponding lattice constants in bulk form is summarized in Table 4.[45] WO_3 in monoclinic phase is favored in room temperature; however, a firm assignation of space group to monoclinic phases are still in debate.[46] It is noticed that the lattice parameters obtained via *ab initio* calculation closely match the experimental values.[47] The phase transition scenarios in nanostructured WO_3 are supposed to be more sophisticated. Within Gibbs-Thomson framework, one can generally expect lower transition temperature than their bulk counterparts due to enhanced surface energy. Temperature-dependent Raman spectroscopy provided support for this deduction.[48]

WO_3 is a wide gap n-type semiconductor with valence band top featuring $2p$ states of oxygen and conduction band bottom arising primarily from $5d$ states of tungsten with some mixing of oxygen $2p$ states.[49] Migas et al. maintained there is essentially identical band dispersion near the gap region in case of ϵ-WO_3, δ-WO_3, γ-WO_3 and β-WO_3.[47] When there is oxygen vacancy, the Fermi level moves into the conduction band and the gap shrinks by about 0.5 eV. Migas et al. also pointed out the flat bands at valence band maximum (VBM) and conduction band minimum (CBM) could lead to poor transport of holes and

---

[4] Tungsten, with its electronic configuration as $(Xe)_4f^{14}5d^46s^2$, has empty 5d and 6s orbitals in its +6 oxidation state.

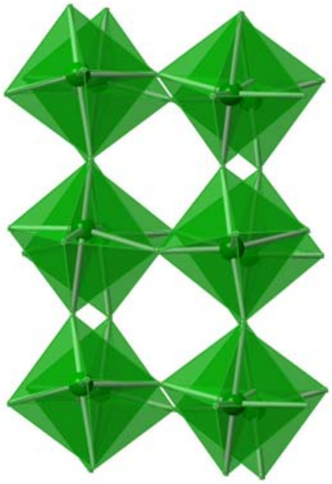

Figure 10: Octahedra model of WO_3

electrons, thus may compromising the function in photoelectrochemical cells.

Besides WO_3, tungsten oxide exists in a series of sub-stoichiometric states. The W_nO_{3n-1} ($n \geq 2$) exhibit {001} crystallographic shearing (CS) structure. Chemical formula corresponding to n=2, 3, 4, 5 and 6 are W_2O_5=$WO_{2.5}$, W_3O_8=$WO_{2.67}$, W_4O_{11}=$WO_{2.75}$, W_5O_{14}=$WO_{2.8}$, and W_6O_{17}=$WO_{2.83}$, which indicates the existence of a oxygen deficient plane at every n row. Actually the value x in WO_x could almost continuously vary within a range of 2.5 to 3. $W_{18}O_{49}$=$WO_{2.72}$ is an exception without {001} CS structure. Moreover, the oxygen deficient planes could extend along directions other than {001}. For instance, the {102} CS planes appears in WO_x where x is within 2.93 to 2.98, and the {103} CS planes for x within 2.87 to 2.93.[50] In WO_x nanorods, the oxygen deficient planes are conductive, each having atomic thickness and separated by several nm of WO_3 layers. Localized surface plasmons could possibly exist on these conductive planes. Therefore, surface-enhanced Raman scattering (SERS) applies and single molecule Raman scattering using individual tungsten oxide nanorod has been demonstrated.[51] Tungsten oxides were probably best

Table 4: List of WO_3 phases

			Lattice constants Å		
Symbol	Temperature (°C)	Phase	a	b	c
ϵ-WO_3	$-140 \sim -50$	monoclinic II	7.378	7.378	7.664
δ-WO_3	$-50 \sim 17$	triclinic	7.309	7.522	7.686
γ-WO_3	$17 \sim 330$	monoclinic I	7.306	7.540	7.692
β-WO_3	$330 \sim 740$	orthorhombic	7.384	7.512	3.846
α-WO_3	> 740	tetragonal	5.25	NA	3.91
h-WO_3	< 400	hexagonal	7.298	NA	3.899

known for the electrochromic effect, meaning the coloration (deep blue) and bleaching (transparent) states of WO_3 are reversibly switched upon forward and backward voltage, and the coloration or bleached states remain after disconnecting the voltage. On basis of this property, ECD of tremendous energy saving potential is conceptualized and some products have already been commercialized (i.e. smart window[5]), although the materials used is not clear.

In the past decades, substantial works have been devoted to understanding the chromogenic phenomena in WO_3. Several key results were highlighted as reviewed in Ref.[13]:

- coloration and bleaching can also be stimulated by other routes, such as by UV irradiation, thermal treating, heating in vacuum, reducing atmosphere, *etc*;
- no electrical coloration occurs in vacuum, but other routes still work;
- coloration is associated with a proportional increase in conductivity;
- coloration spectrum is essentially similar in all cases except small variation in peak position;
- coloration is structural sensitive and most efficient in amorphous films.

---

[5] "We did a case study in five cities, and the average savings in commercial buildings are about 25 percent of the heating, ventilation, and air-conditioning energy use annually," said CEO of View, Inc.

So far there is no unifying model that could reconcile these contradictory experimental observations. Among all the developed models, polaronic absorption is the most widely accepted mechanism for coloration. The concept of polaron was first proposed by Landau in 1933. In ionic or highly polar crystals, such as II-VI semiconductors, alkali halides, and transition metal oxides, the Coulomb interaction between a conduction electron and the lattice ions results in a strong electron-phonon coupling. A new quasi-particle, virtual phonon, can be defined corresponding to the effect of electron pulling nearby positive ions towards it and pushing nearby negative ions away. The electron and its virtual phonons, taken together, can be treated as a new composite particle, called an electron polaron; the hole polaron is defined analogously.[52] In polaron model,[6] the intercalation of M^+ (M = H, Li, or Na) ions into WO_3 films is accompanied with the formation of small polarons (r_p comparable to unit cell size) and formal reduction of some W^{6+} sites to W^{5+}, as depicted in Eq. 6.

$$xM^{+} + xe^{-} + \alpha\text{-}WO_{3-y} \rightarrow \alpha\text{-}M_xWO_{3-y} \tag{6}$$

During the intercalation process, the M^+ ions enter into these vacant sites.[53] Coloration occurs when electron transition occurs from the hole polaron band to the electron polaron band. And the polaron binding energy (E_p) is given by

$$E_p = -\frac{e^2}{2r_p}(\epsilon_\infty^{-1} - \epsilon_{st}^{-1}) \tag{7}$$

---

[6] When a free electron travels through a polar solid, it creates a local lattice displacement (longitudinal optical phonon clouds) due to the coulombic interaction with neighboring ions. This local distortion and the electron together is equivalent to a new elementary exciton of the crystal, and is named as polaron

where ϵ_∞ and ϵ_{st} are optical and static dielectric constants, respectively, and polaron radius r_p, which specifies how far the lattice distortion extends, is related to polaron density N_p by $r_p = \frac{1}{2}\sqrt[3]{\pi/6N_p}$. However, the polaron model has difficulty in estimating r_p. The asymmetric optical absorption spectrum are often characteristic of large polarons, and dielectric constants ($\epsilon_\infty = 6.52, \epsilon_{st} > 50$,[13]) suggests the formation of bipolaron in WO_3. Moreover, polaron model does not take oxygen vacancy into account, which plays a vital role in the nonstoichiometric tungsten oxides. For instance, it is observed that $WO_{3\text{-}y}$ films are metallic and conductive for $y > 0.5$, blue and conductive for $y = 0.3 \sim 0.5$, and transparent and resistive when $y < 0.3$, regardless of the preparation methods.[46]

Therefore, another model in analogy to the F-color center was proposed. Color center model assumes the presence of oxygen vacancy V_O^0 is associated with W^{4+} or $2W^{5+}$ states. This defect level is expected to be inside or near the valence band. When one electron is removed from this level, V_O^0 is converted to V_O^+. The positively charged vacancy exerts Coulombic repulsion to the nearest W-ions, which results in a displacement of the neighboring W-ions and an upward shift of the defect level into the bandgap, thereby creating a color center. The optical transition from V_O^+ to V_O^{2+} (a state within the conduction band) contributes to coloration.[13]

The polaron and color center models both agree on that W^{5+} and its transition is responsible for the coloration; but disagree on how this W^{5+} state and the corresponding energy levels are created (foreign ion reduction in polaron model and oxygen vacancy in color center model). A modified polaron model is proposed to include W^{4+} states in host lattice. Coloration mechanism is represented by Eq. 8 and 9, which described the polaron hopping from one site to another.[46]

$$h\nu + W^{5+}(A) + W^{6+}(B) \rightarrow W^{5+}(B) + W^{6+}(A) + E_{phonon} \quad (8)$$

$$h\nu + W^{5+}(A) + W^{4+}(B) \rightarrow W^{5+}(B) + W^{4+}(A) + E_{phonon} \quad (9)$$

Similar scenario occurs in the gasochromic effect. Two models, double injection and color center, arise to account for the coloration upon exposure to certain gases. Both consent to Eq. 8. But there is a disagreement on the final states. Double injection model supports the formation of tungsten bronze H_xWO_3 while color center model insists on the inward diffusion of oxygen vacancy and outward diffusion of water molecules. Both have been substantiated experimentally;[54] therefore, the exact mechanism in WO_x still requires further investigation.

3.1.2 Review of Synthesis Methods of Tungsten Oxides

As the chemical formula WO_3 suggested, the most straightforward way is heating metallic tungsten (W) in various forms,[55–57] i.e., powders, foils, and wires. Actually WO_x NWs[7] were observed when directly heating W wires.[58] Due to the extreme high melting point of W, it requires high temperature (say, above 1100 °C) to produce large amount of growth species. Therefore scalable growth seems difficult at low temperature range unless other activation mechanisms are used. The dc current heating proved to be a route with potential large yield, where tungsten wire or filament was connected to a current source, and substrate was positioned in proximity to the heated W wire.[59–61] Tungsten oxides powder can also been used as precursor to prepare WO_x NWs.[26, 62] Hydrogen-containing agents (i.e. water, H_2, or methane[63]) were often involved into the reaction.[64, 65] The potential benefit is WO_3 has a much lower melting point (≈ 1470 °C) than that of metallic tungsten.

---

[7] x is between 2 and 3

Meanwhile, organometallic decomposition is another feasible method. Pol et al. obtained $W_{18}O_{49}$ nanorods by thermal dissociation of $WO(OMe)_4$ at 700 °C and WO_3 by further annealing at 500 °C in air atmosphere.[66] Spray pyrolysis is a typical aerosol-assisted CVD technique. Typical process flow is: the precursor solution is pumped to an atomizer and then sprayed through the carrier gas as a fine mist of very small droplets onto heated substrates. Subsequently the droplets undergo evaporation, solute condensation, and thermal decomposition, which then result in film formation.[45] Main reactions include:

$$W + O_2 \rightarrow WO_{3-x} \tag{10}$$

$$W + H_2O \rightarrow W_{3-x} + H_2 \tag{11}$$

Besides, hydrothermal method has been an important route to synthesize a diversity of nanomaterials. Preparation of WO_{3-x} has also been demonstrated hydrothermally.[67, 68] Usually, the precursor (H_2WO_4) is mixed with other reactants (sulfides or certain organic acid) in solution and pH value is adjusted as another control degree of freedom. Then, the solution is transferred into a sealed container (i.e. Teflon autoclave) and maintained at elevated temperature (120 ~ 300 °C) for tens of hours. Finally, the product is separated from the solution and dried, layered $WO_3 \cdot nH_2O$ flakes are usual products. A brief summary of representative synthesis methods is shown in Table 5.

3.2 Experimental

Metallic tungsten powders (W) were utilized as source materials in this work. Four kinds of W powder were used in total, as summarized in Table 6. Two growth configurations were explored, namely non-seeded growth and seeded growth.

Table 5: Summary of tungsten oxide growth methods

Phase	Methods	Highlights	Reference
WO_3	hot W filament (above 1500 °C) in Ar/O_2 flow	Cubic phase, PL, resistivity measured	[60]
	W filament DC heating in NH_3 or N_2/H_2 flow	multi phases, 100mg per batch, stable dispersion in both organic and aqueous solvents	[61]
	W powder heating, Ar/O_2 flow	triclinic phase, CL at 370,415nm, UV-Vis, 3eV	[57]
	WOx film in H_2 and CH_4 flow	monoclinic phase, tungsten carbide is the key	[63]
	$Na_2WO_4 \cdot 2\,H_2O$ by hydrothermal heating to test for line break	3 different morphologies and photodegradation	[69]
	$H_2WO_4 \cdot 2\,H_2O$, H_2O_2 and poly(vinyl alcohol) etc by solvothermal	multi phases deposition of FTO with varied bandgaps	[1]
$W_{18}O_{49}$	KOH etching of W tips followed by heating in Ar flow	oxygen from leakage, VS process	[58]
	$W(CO)_6$, $Me_3NO \cdot 2\,H_2O$ and oleylamine by hydrothermal	RT PL at 350nm and 440nm	[67]

Table 6: Tungsten powder sizes and purities

Name	purity	average size	vendor info
3N	99.9%	17 μm	Alfa Aesar #39749
3N5	99.95%	32 μm	Alfa Aesar #42477
4N5	99.995%	3.3 μm	Materion T-2049
5N	99.999%	1.5 μm	Alfa Aesar #12973

3.2.1 Non-seeded Growth

In a typical non-seeded experiment (Fig. 11), about 2 g tungsten powder (3N) was positioned in the upstream end of a quartz boat, and downstream about 2.5 inch the substrate was stationed. The substrates were p-type, boron-doped and [100]-orientated silicon with about 1 μm thermally-grown silicon oxide layer on the polished side. The substrate cleaning procedures have been elucidated on page 11. The boat was then loaded into the reaction chamber in a way that the powder source was placed in the center of the heating zone, and the substrate upstream end was aligned at 6.5 inch, as defined in Fig. 11. After pumping down, 1 standard cubic centimeters per minute (sccm) O_2 and 10 sccm Ar were admitted into

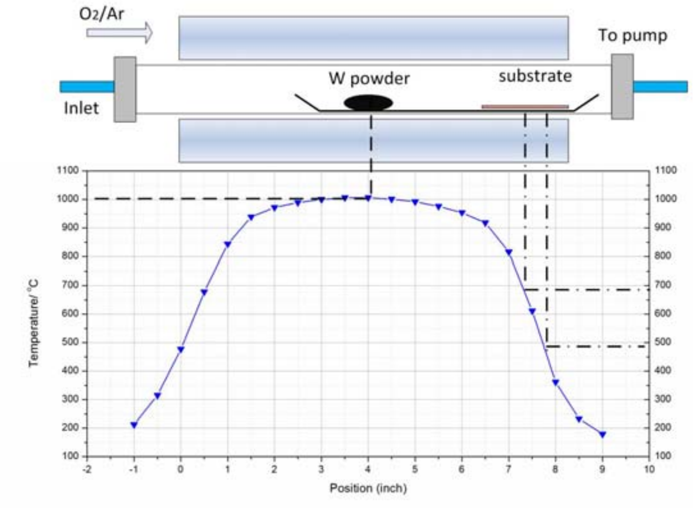

Figure 11: WO_3 NW CVD growth and the temperature profile. The nominal NWs growth temperature were estimated according to the interpolation data. Zero inch location is defined at the upstream edge of furnace.

the chamber, respectively, after which the overall pressure read approximately 110 mTorr. The temperature ramped up to 1000 °C in 30 min and lasted for 4 h, and subsequently the apparatus was allowed to naturally cool to room temperature.

3.2.2 Seeded Growth

In the seeded growth, additional tungsten powders were used on the substrate serving as local seed, on which a dense WO_3 NW array grew. For the tungsten seed particles, 3N powders were used in typical NW growth, and other tungsten powders with different sizes were employed in control experiments, including 3N5, 4N5, and 5N. All reactants were employed as received without further processing.

In a typical growth, high purity tungsten powders were positioned at the upstream end of a quartz boat, with the substrate located ca. 65 mm downstream. The quartz boat was then transferred into the reaction chamber in a way that the tungsten source was located at the center of the reaction chamber. During the growth, the tungsten source was heated at 1000 °C, while the substrate temperature ranged from 800 °C to 400 °C. After the reaction chamber was pumped down to an ultimate pressure of ~ 8 mTorr, 1 sccm oxygen (O_2) and 10 sccm argon (Ar) were introduced into the chamber, respectively. The heating temperature was ramped to 1000 °C in 30 min and lasted for 240 min. Subsequently, the apparatus was allowed to naturally cool to room temperature.

To study the growth mechanism, controlled experiments were performed on the oxidation of the tungsten seed particles dispersed on the substrate. In a typical oxidation experiment, tungsten powders were loaded into the uniform heating zone at the center of the chamber, and the sealed chamber was pumped down to an ultimate pressure of ~ 8 mTorr. Then oxygen flow, varying between 1 sccm to 10 sccm, was admitted from the upstream inlet. With 10 sccm UHP Ar (99.999%) as carrier gas, the overall pressure reached to about 100 mTorr. The heating temperature (500 to 750 °C) was ramped up in 30 min and lasted for 30 min; then, the heating power was turned off, and the chamber was allowed to naturally cool to room temperature.

3.3 Results and Discussion on Tungsten Oxide Nanowires

3.3.1 Tungsten Oxides: Impurities and Residual Effects

The growth dynamics of each source were investigated in the non-seeded growth. In each experiment, the temperature, flow rate, source, and substrate locations were controlled. Another parameter the author found important is the growth number[8] in the same reaction chamber. Usually, one will conduct several runs in the same chamber, and different results may arise with respect to the growth number. With this degree of freedom included, the primary features of the deposition and the associated parameters were summarized in Table 7. The change of metallic W source after growth carries important information about the growth.

Table 7: WO_3 non-seeded growth summary

	Growth Number		
Source	First	Second and more	Sodium(ppm)
3N	Morphology from high to low temperature: islands, dense layer and a few NWs	Dense wires become more and more, sodium tungsten oxides phases dominate	20
3N5	islands in high temperature end and layers in low temperature end	NA	NA
4N5	dense islands, some tiny wires in low temperature end	NA	0.065
5N	similar to those of 4N5	NA	0.05

---

[8] Defined as the order of growth performed in the same reaction chamber

So before examining the deposition on substrates, the SEM images of all powders before and after growth were presented in Fig. 12 and Fig. 13, respectively. Tungsten metal crystallizes in body center cubic (BCC) phase. Overall, the facets were still discernible. The 4N5 and 5N powders shared similar appearance and size distribution (Fig. 12c-d). In contrast, 3N powders were almost half the size of 3N5 ones and had more uniform size distribution as well. Absolute size and its distribution played a key role in its usage as seed, as discussed in Section 3.3.2. After growth, 4N5 and 5N powder (Fig. 13c-d) both developed the round

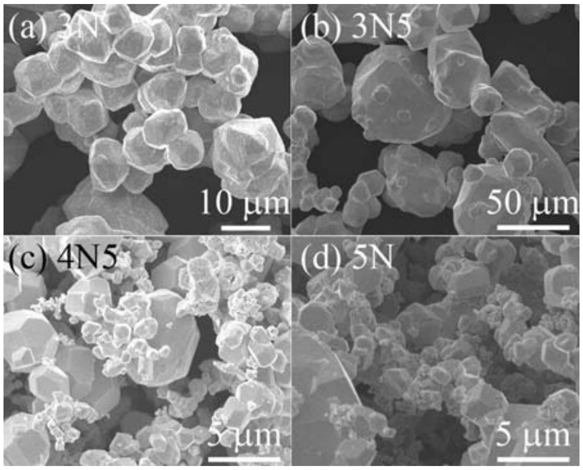

Figure 12: SEM images of W powder before growth for (a) 3N, (b) 3N5, (c) 4N5 and (d) 5N, respectively.

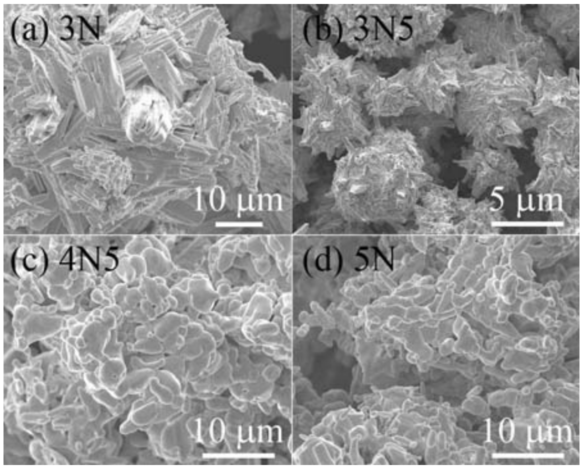

Figure 13: SEM images of W powder after growth for (a) 3N, (b) 3N5, (c) 4N5 and (d) 5N.

edges, while 3N and 3N5 powders (Fig. 13a-b) became bundled rods. This difference mainly arose from the average size, which dictated the degree of oxidation. Another possible reason was the presence of foreign elements in each W powders. As indicated by the certificate of analysis from corresponding vendors, carbon, nickel, iron, and sodium amounts up to tens of ppm in low purity W source.

The sodium contents in 3N powders fundamentally changed the deposition in the non-seeded growth. Typical morphologies of the as-synthesized nanostructures grown on a SiO_2-Si substrate were shown in Fig. 14a. The nanostructures were NWs with lengths up to several hundred microns and diameters about 40 to 500 nm. The deposition of nanowires was generally located on the substrates with the growth temperature ranging from 660 to 420 °C. Enlarged view at higher magnification revealed some nanowires were cylindrical and some were bundled belt. Rectangular microplate structures grew at lower temperature end of substrate, as displayed in Fig. 14b and inset. The chemical compositions of the deposition were analyzed using EDX. A representative EDX spectrum in Fig. 14c show the existence of W, Na, O, and Si signals in the specimen, where the Si signal was from the substrate. The crystal structures of the as-synthesized specimens were examined using XRD. The diffraction peaks were carefully indexed and the deposition was identified as two phases of sodium tungsten oxides and one phase of tungsten oxide, as indicated on Fig. 14d. The two sodium tungsten oxide phases were the triclinic $Na_5W_{14}O_{44}$ phase (ICDD PDF 04-012-4449, a=7.2740 Å, b=7.2911 Å, c=18.5510 Å, α=96.37°, β=90.89°, γ=119.65°) and the triclinic $Na_2W_4O_{13}$ phase (ICDD PDF 04-012-7108, a=11.1630 Å, b=3.8940 Å, c=8.2550 Å, α=90.60°, β=131.36°, γ=79.70°). The tungsten oxide was the monoclinic WO_3 phase (ICDD PDF 01-083-0950, a=7.30084 Å, b=7.53889 Å, c=7.6896 Å, β=90.89°).

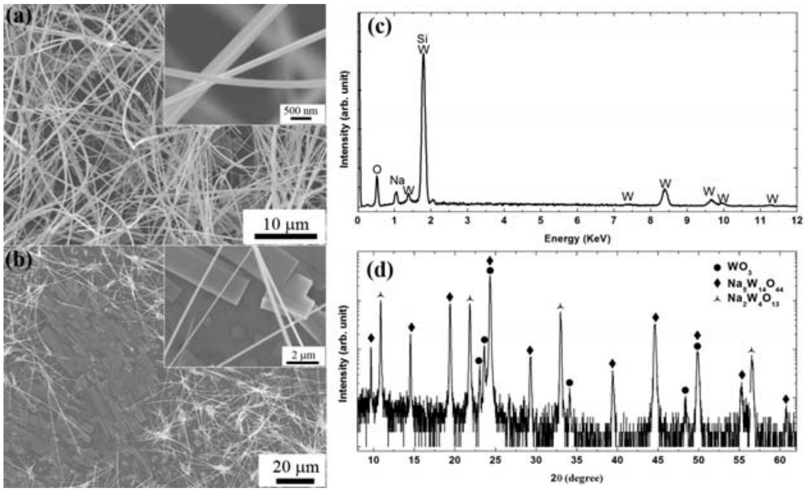

Figure 14: SEM images of (a) dense array of the as-synthesized ultra-long nanowires on SiO_2-Si substrate and (b) rectangular microplates grow among the nanowires. (c) EDS and (d) XRD spectra showing the chemical compositions and phases of the deposition.

XRD measurements revealed the overall structure of the specimen. To obtain detailed information on the crystallinity, composition, and growth direction of the nanostructures, TEM analyses with imaging, electron diffraction, and EDX were performed on more than 20 nanowires. The majority of the nanowires were identified as the $Na_5W_{14}O_{44}$ phase (Fig. 15a-c). The HRTEM image in Fig. 15b revealed that the nanowire exhibited a single-crystalline structure. The corresponding diffraction pattern in the inset of Fig. 15b was recorded in $[\bar{1}10]$ axis. Based on the analyses on a series of diffraction patterns and HRTEM images, the nanowire was confirmed as the triclinic $Na_5W_{14}O_{44}$. The growth direction of $Na_5W_{14}O_{44}$ NWs was determined to be parallel to the (001) plane. EDX measurement (Fig. 15c) show the nanowire consisted of W, Na, and O. No other elements were detected.[9] Small fraction of nanowires were found to be the monoclinic WO_3 phase (Fig. 15d-f). The SAED shown in the inset of Fig. 15e was recorded in [100] zone. The growth direction of the WO_3 nanowire was determined to be perpendicular to the (002) plane with a d-spacing

---

[9] The Cu and C signals come from the supporting Cu grid with lacey carbon and the Cr signal from the tip of JEOL double tilt holder.

of 0.38 nm. EDX spectrum in Fig. 15f indicated the nanowire consisted of W and O without Na or other impurities. The rectangular microplate structures shown in Fig. 14b were also collected for TEM examination. These microplate structures were identified to be the triclinic $Na_2W_4O_{13}$ phase. The SAED in Fig. 15h was recorded in [101] axis. No high-quality HRTEM images were acquired for the $Na_2W_4O_{13}$ plate due to its thickness. The long edge of the plate was identified as parallel to the (010) plane and the short edge parallel to the ($\bar{1}01$) plane. From XRD spectra, the long edge of $Na_2W_4O_{13}$ plate can be figured out as the $\vec{c}$ axis and the short edge is along the $\vec{b}$ axis. Fig. 15i show the plate structure also consisted of W, Na, and O and no other impurities were detected. Normalized to the highest W peak, the Na peak intensity in Fig. 15i was higher than the one in Fig. 15c. This result indicated a higher Na:W ratio for the $Na_2W_4O_{13}$ plate structure than that of $Na_5W_{14}O_{44}$ nanowires, in consistent with the compositions of these two phases.

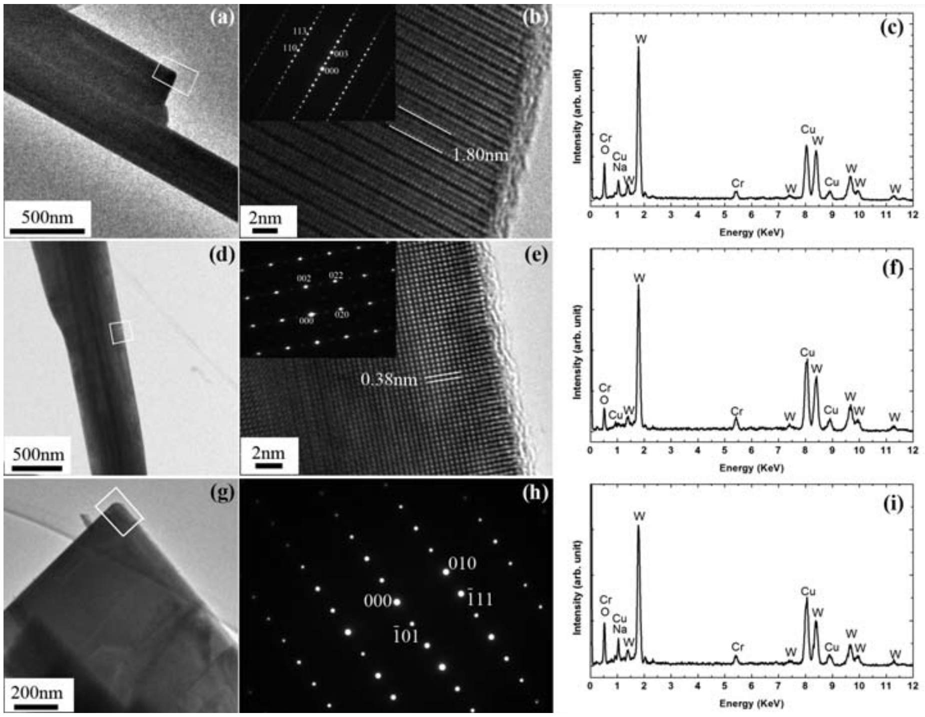

Figure 15: TEM images at low-magnification, HRTEM images, and EDS spectra of a $Na_5W_{14}O_{44}$ NW (a, b, c), a WO_3 NW (d, e, f), and a $Na_2W_4O_{13}$ microplate (g, h, i).

Micro-Raman spectroscopy was also carried out at room temperature in ambient atmosphere to confirm the phases of the microplates and ultra-long nanowires. Fig. 16a show the Raman spectrum of the microplates. The Raman lines at 949, 794-777, 366-263 cm^{-1} closely matched the reported $Na_2W_4O_{13}$ Raman shift.[70] The Raman spectrum from the ultra-long nanowires was shown in Fig. 16b. The spectrum show major peaks in 100-150 cm^{-1}, 650-900 cm^{-1}, and 900-100 cm^{-1} regions. As compared to the reported peak positions (shown by reference lines in Fig. 16b), the nanowires consisted of only little amount of WO_3 or $Na_2W_4O_{13}$ phase. Major peaks at 107, 695, 765, 913, 943, and 965 cm^{-1} cannot be assigned to reference in literatures. According to XRD and TEM analyses, the nanowires were mainly $Na_5W_{14}O_{44}$; therefore these peaks should belong to the $Na_5W_{14}O_{44}$ phase. So far no Raman spectrum has been reported for this phase, hence this is probably the first observed Raman pattern for $Na_5W_{14}O_{44}$.

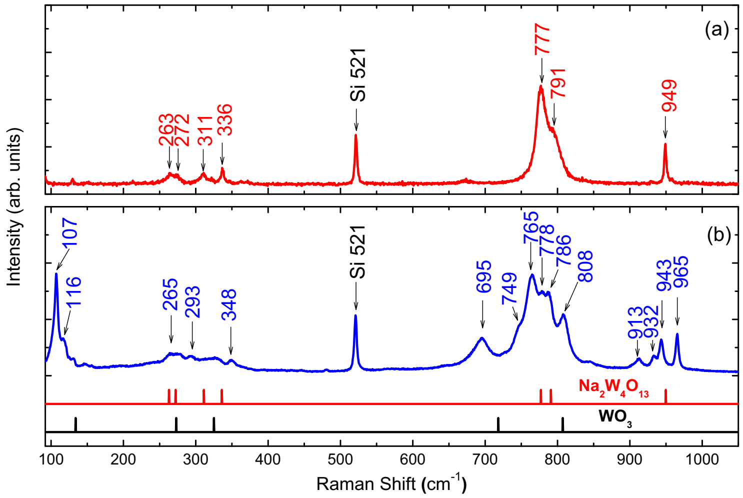

Figure 16: Raman spectra of (a) microplates matching the reported peak positions of the $Na_2W_4O_{13}$ phase, and (b) nanowires with comparisons to the reported major peak positions of WO_3 (shown by black line) and $Na_2W_4O_{13}$ (shown by red line) phases.

Based on the correlation of Raman spectra and crystallographic data of a variety of tungsten bronze, an empirical formula to relate the Raman peaks and W−O bonding lengths has been found as

$$\nu = 25823 \exp(-1.902 \cdot R) \tag{12}$$

where R is tungsten-oxygen bond length in Å, and ν is Raman stretching wavenumber in cm^{-1}.[71] The standard deviation of estimating W−O bond distance from Raman stretching wavenumber was ±0.034 Å. The observed Raman peaks of $Na_5W_{14}O_{44}$ phase were located at 965, 943, 913, 808, 786, 778, 765, 695, and 107 cm^{-1}. Multi-peak Lorentzian fitting was preformed to precisely determine the central maximum. Good fitting was obtained in this study, as shown in Fig. 17. The calculated W−O bond distances using Eq. 12 were then listed in Table 8. The predicted W−O bond lengths agreed very well with the crystallographic value of $Na_5W_{14}O_{44}$ phase.[72] The 107 cm^{-1} peak was probably caused by Na−O bond.

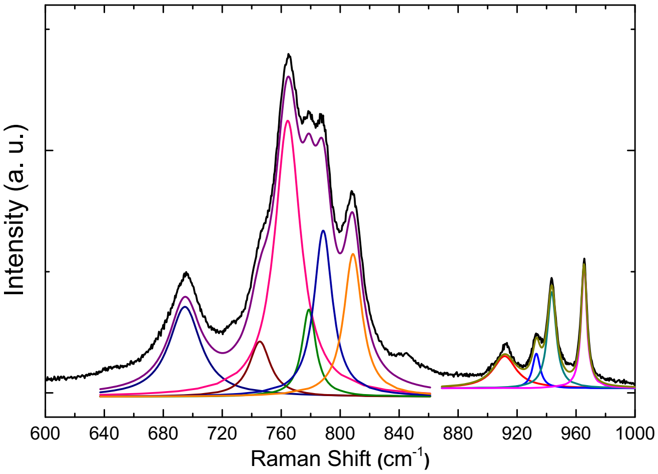

Figure 17: Multi-peak Lorentzian fitting on two major peaks region of $Na_5W_{14}O_{44}$. The peaks sum height difference is caused by different baseline value adopted in each fitting.

For a purpose of comprehensive comparison, the Raman fingerprints of various tungsten oxides and tungstate were listed in Table 9.

Heated at elevated temperatures, the W precursor, quartz tube, and quartz boat were three possible sources for Na. The sodium concentration in 3N source was about 20 ppm, as

Table 8: W−O bond length predication

Fitted center (cm^{-1})	length (Å)	Fitted center (cm^{-1})	length (Å)
694.6	1.900	808.6	1.821
745.4	1.863	911.5	1.758
764.4	1.850	933.0	1.745
778.7	1.840	943.5	1.740
788.4	1.834	965.4	1.728

Table 9: Raman fingerprints of tungsten oxides and sodium tungsten oxides

Phase	Raman Shift (cm^{-1})	Reference
WO_2	287(s), 334(w), 514(m), 600(w), 621(w), 785(vs)	[73]
$W_{18}O_{49}$	broad bands from 750 to 780	[74]
	267(s), 778(s), 969(m)	[75]
m-WO_3	131(m), 265(m), 327(m), 715(s), 807(vs)	[76, 77]
h-WO_3	162(m), 253(m), 320(m), 645, 690(s), 817(vs)	[77]
$WO_3 \cdot H_2O$	230(m), 377(w), 428(w), 650(s), 816(vs), 946(vs)	[77]
$WO_3 \cdot 2\,H_2O$	235, 268(m), 380(w), 662(s), 685(vs), 960(vs)	[77]
Na_2WO_4	94(w), 314(vw), 377(m), 813(m), 930(vs)	[78]
$Na_2W_2O_7$	381(w), 422(w), 763(w), 835(s), 886(m), 948(m), 957(vs)	[79]
$Na_2W_4O_{13}$	263(w), 272(w), 311(w), 366(w), 777(vs), 794(s), 949(m)	[70]
$Na_5W_{14}O_{44}$	107(s),695(m), 765(vs), 913(w), 943(m), 965(m)	this work

Materials in solid state, vw-very weak; w-weak; m-medium; s-strong; vs-very strong

provided by vendor.[10] The Na concentrations in quartz tube and quartz boat (GE 214 quartz, Wilmad Labglass) were 1 ppm and 0.7 ppm, respectively. To verify the major source of Na content, control experiments were employed by using W source with higher purities (4N5 or 5N). These ultra-high purity W sources produced pure tungsten oxide deposition, and no Na content was detected by EDX. These results verified the Na content was mainly from the 3N W powders. In the non-seeded growth experiments, the W source was first

---

[10] Owing to the non-uniform distribution of foreign elements, detection of sodium by EDX is possible although the concentration is below the capacity limit of typical EDX.

slowly oxidized at 1000 °C with 1 sccm O_2, and then the oxidized source was evaporated producing WO_3 and other sub-stoichiometric tungsten oxide vapors. The tungsten oxide vapors produced this way were limited by the slow oxidation, as indicated by *a*) only small amount of the tungsten source was consumed during the growth; and *b*) only the top layer of the tungsten source was oxidized showing a dark blue color after growth. Owing to its low concentration, the exact composition of the Na content in the tungsten source was difficult to probe; however, the evaporation rate of the Na content was expected to be high when heated at 1000 °C. This assumption was supported by the observation that no Na was found in the deposition along the whole substrate in control experiments using the used 3N W source. Put it in another way, this observation indicated that the majority of Na content was already evaporated in previous experiment. Hence, despite of its low concentration in the source, the total amount of Na-based vapors produced during the growth could be significant, resulting in the dominance of sodium tungsten oxide phases in the nanowire growth region.

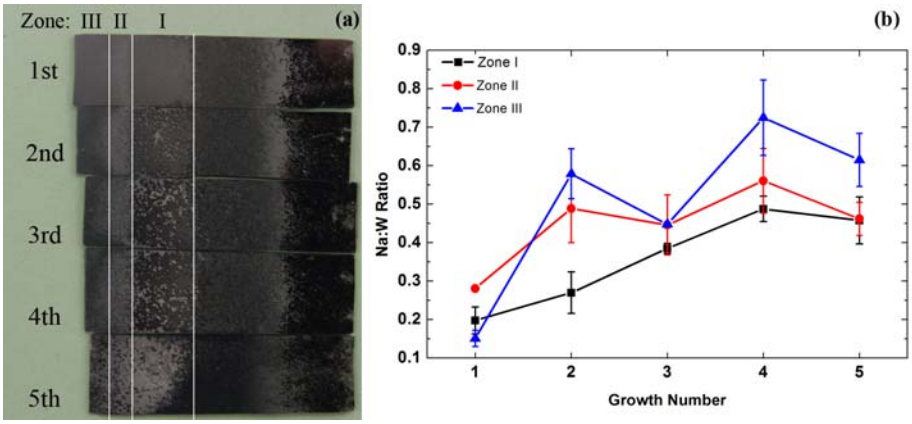

Figure 18: (a) Photograph of a series of specimens grown in the same reaction chamber with the increase of growth number showing different growth zones and corresponding morphology changes. (b) Change of Na/W ratios with the increase of growth number at different growth zones.

As shown by the photograph in Fig. 18a, for a series of growth performed in the same reaction chamber, the morphology of the nanowires changed with the increase of growth number. Three growth zones of nanowires can be identified on basis of the coverage and density of the nanowires, as delimited by the vertical guide line. The growth Zone I was located at high temperature end ranging from 660 to 520 °C, Zone II was from 520 to 470 °C, and Zone III from 470 to 420 °C. Detailed morphological changes were depicted in Fig. 19. For the first growth (Fig. 19a-c) in a new clean reaction chamber, there were only a little nanowires scattered in Zone I (Fig. 19a), ultra-long nanowires were mostly found in Zone II with higher density and coverage (Fig. 19b), and in Zone III the coverage, density, and length of nanowires gradually reduced as the growth location moved downstream (Fig. 19c). With growth number increased to 3 (Fig. 19d-f) and 5 (Fig. 19g-i), the coverage, density, and length of the nanowires increased in all three zones. Zone I saw the most significant morphology changes, as shown by Fig. 18a and Fig. 19g. After the fifth growth in the same

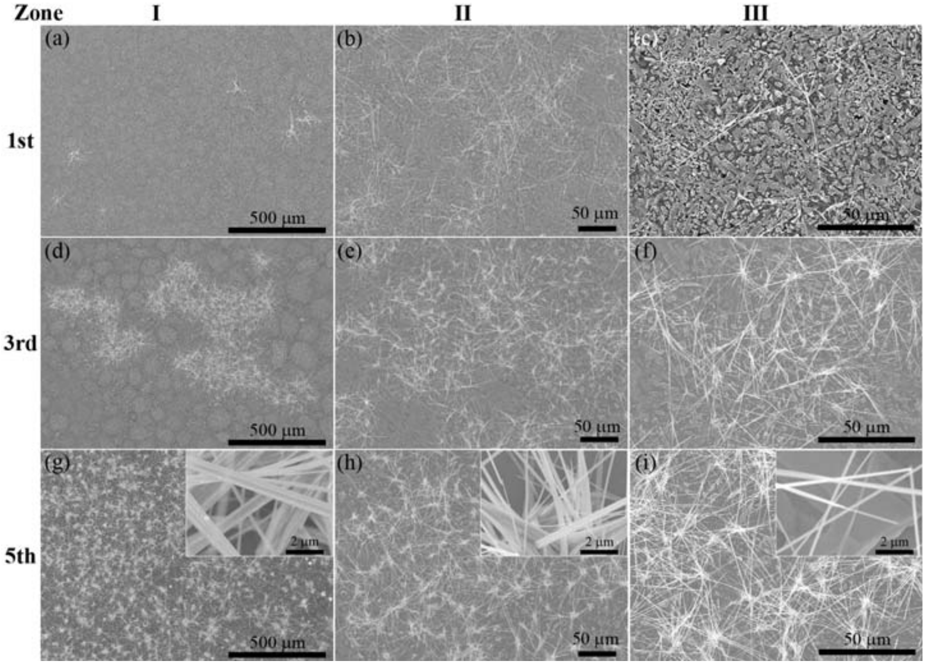

Figure 19: SEM images of morphology evolution of the NWs at different growth zones showing morphology changes with the increase of growth number. The insets show detailed structures of the NWs.

reaction chamber, the deposition of ultra-long nanowires almost covered all three zones. For Zones I and II, no significant morphology change was observed with further increase of the growth number up to 8. However, for Zone III the microplate structures (shown in inset of Fig. 19i) kept increasing significantly with the growth number. EDX study revealed the variation of Na concentration in the deposition with the growth number. Fig. 18b show the variation of the Na/W ratios with the increase of growth number at different nanowire growth zones. Generally, the Na/W ratios at all growth zones increased with the increase of growth number. The large fluctuation of Na/W ratio at Zone III was presumably due to the uneven distribution of Na content with different morphologies at Zone III.

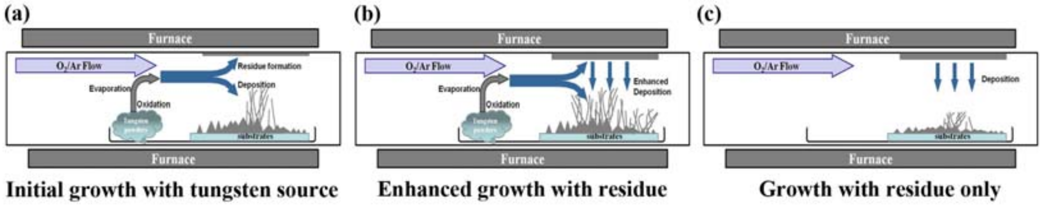

Figure 20: Schematic drawings showing (a) growth with tungsten source in a new tube, (b) enhanced growth with both residue deposition and tungsten source, and (c) growth with residue deposition only.

A mechanism of residue deposition enhanced growth was proposed to explain the morphology evolution of the nanowires with the growth number. Since the CVD setup employed in this thesis was a hot-wall system, deposition formed on the substrate surface as well as on the inner wall of the reaction chamber in the growth area. Residue deposition was found on the quartz tube, which can be distinguished by the color change on the quartz tube after each growth. With the increase of growth number for the same reaction chamber, the residue deposition on the inner wall of the tube also increased. If a clean quartz tube free of any residue deposition was used as the reaction chamber, the vapors were supplied only from the source material forming deposition in the growth area with lower temperature (as shown by the schematics in Fig. 20a). When a quartz tube with residue deposition from previous depositions was used repeatedly as the reaction chamber, the residue deposition heated at growth temperature could also produce vapor locally; therefore, the vapors from both the source materials and the local residue deposition would result in an enhanced growth of nanowires (Fig. 20b). To prove this hypothesis, control experiments were performed utilizing a quartz tube used multiple times previously (e.g. a growth number of 9). The experiments were carried out without any source materials while other growth parameters remained the same. Similar nanowires were found on the substrate in the nanowire growth zones. Without the source materials, the residue deposition from the tube surface was the only possible source that could produce vapors forming nanowires on the substrate (Fig. 20c). This result confirmed the nanowire growth could be enhanced by the presence of the residue deposition and explained the morphology changes of the nanowires with the increase of growth number.

The general trend of Na/W ratios with the growth number can also be explained by the aforementioned effect of residue deposition. The sodium contents from the residue deposition will join the new Na contents from the W source forming deposition. Fig. 21 displayed the XRD spectra of a series of specimens with the growth number increases from 1 to 5. The XRD spectra revealed the relative concentration dynamics of the three phases as the growth number increases. Compared to the WO_3 phase, the $Na_5W_{14}O_{44}$ and the $Na_2W_4O_{13}$ phases increased significantly as the growth number increased from 1 to 5. And in the 5th growth, $Na_2W_4O_{13}$ became the dominated phase in comparison to the other two phases. These results were consistent with the SEM observation (Fig. 19) and the composition change from

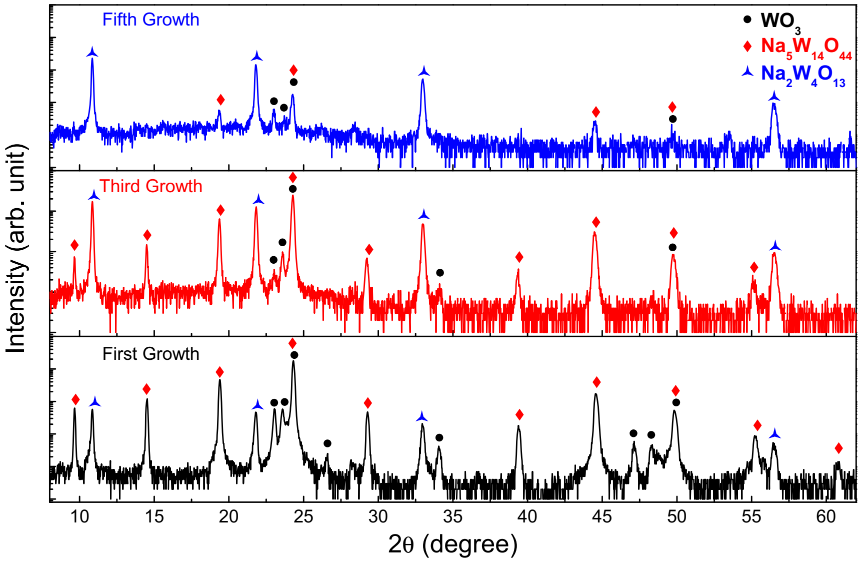

Figure 21: XRD spectra of the as-synthesized specimen with the increase of growth number from 1 to 5.

Table 10: Assignment of XRD peak indices to different phases

WO_3		$Na_5W_{14}O_{44}$		$Na_2W_4O_{13}$	
2θ	hkl	2θ	hkl	2θ	hkl
23.05	0 0 2	9.65	0 0 2	10.85	1 0 0
23.59	0 2 0	14.49	0 0 3	21.8	2 0 0
24.31	2 0 0	19.37	0 0 4	32.97	3 0 0
26.60	1 2 0	24.27	0 0 5	56.45	5 0 0
34.10	2 0 2	29.22	0 0 6		
47.11	0 0 4	39.36	0 0 8		
48.29	0 4 0	44.46	0 0 9		
49.79	4 0 0	49.71	0 0 10		
		55.23	0 0 11		
		60.77	0 0 12		

the EDX measurements (Fig. 18b). Details XRD indices assignment was summarized in Table 10.

The $Na_5W_{14}O_{44}$ phase was further confirmed by a XRD scanning from 4 to 10 degree in $2\theta/\Omega$ configuration. As shown in Fig. 22, two peaks at 4.84° and 9.65° were well resolved, corresponding a lattice spacing of 18.25 Å and 9.16 Å, respectively. This compares favorably with both HRTEM analysis (Fig. 15e) and ICDD PDF 04-012-4449 database reference.

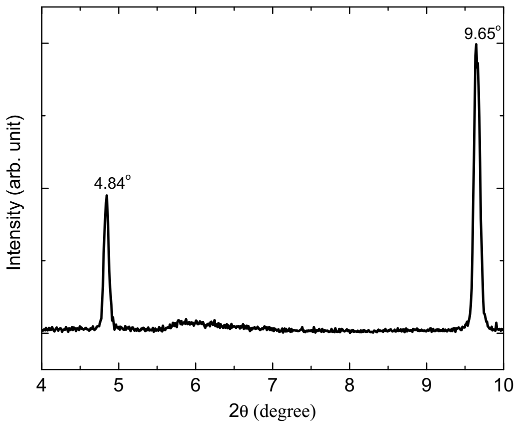

Figure 22: Low angle scan of XRD pattern on the as-grown sodium tungsten oxide sample

The optical transmission and reflection properties of the as-grown $Na_5W_{14}O_{44}$ NWs were evaluated using UV-Vis spectroscopy, as shown in Fig. 23. The sample was prepared on a quartz substrate, which is transparent from 300 to 1300 nm. SEM images (not shown) found dense NWs array growth similar to those on SiO_2-Si substrates, indicating the residue effect was not sensitive to the substrate. The transmission (Fig. 23a) stood at about 70% above 400nm and began to drop significantly for shorter wavelength. This variation was also identified in the diffuse reflection spectrum (DRS) in Fig. 23b, where the reflection

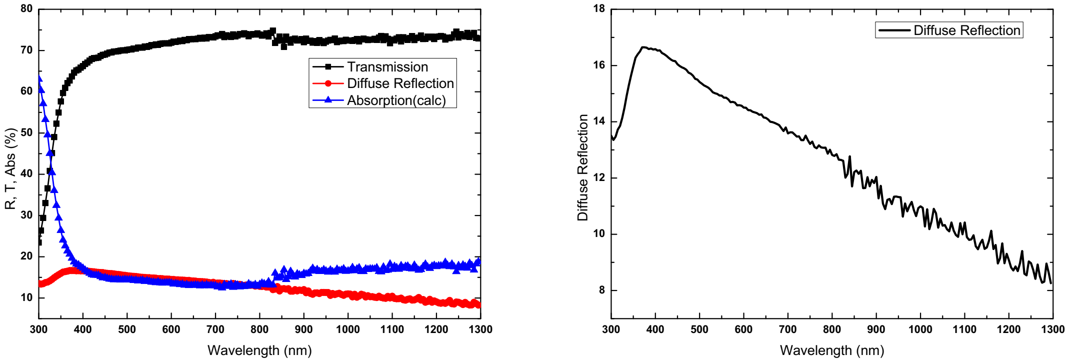

(a) (b)

Figure 23: UV-Vis and DRS of $Na_5W_{14}O_{44}$ NWs on quartz: (a) Optical transmission and (b) diffuse reflection spectra.

reached to a maximum of 16% at 390 nm. One difference was the DRS increased from 1300 nm to 400nm, presumably due to the inverse scattering intensity with NW dimension of 300 nm. The calculated absorption was shown in Fig. 23a, suggesting an energy gap edge at about 380 nm. This was consistent with the observed white sample color; however, the conductivity of $Na_5W_{14}O_{44}$ has not been investigated experimentally. Based on the electron sum rule, the sodium tungsten oxide can be cast into $Na_5W_1^{5+}W_{13}^{6+}O_{44}$, which indicated the W ion valence states were quite close to that in WO_3. Further investigation is needed to vigorously determined the electronic transport properties of $Na_5W_{14}O_{44}$ NWs.

Typical morphologies of non-seeded growth using other powders were shown in Fig. 24 and Fig. 25, respectively. The common feature of these samples was the dominance of islands growth in upstream end and layers growth in downstream end. The exact dimension still show some minor difference, particularly in the low temperature region. The deposition with 4N5 and 5N powders had much smaller grain size than that with 3N5 powders.

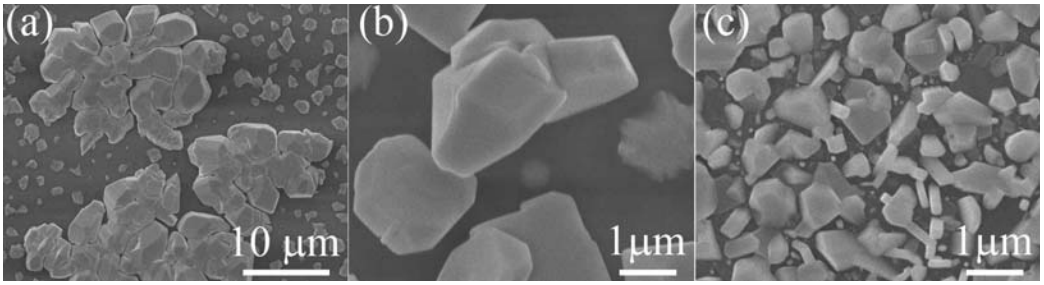

Figure 24: SEM images of WO_3 growth using 3N5 powder showing the morphology variation at (a) 736 °C, (b) 590 °C, and (c) 400 °C.

It was worth pointing out that there were some NWs growth in low temperature end associated with 4N5 growth(Fig. 25c), although not in large scale.

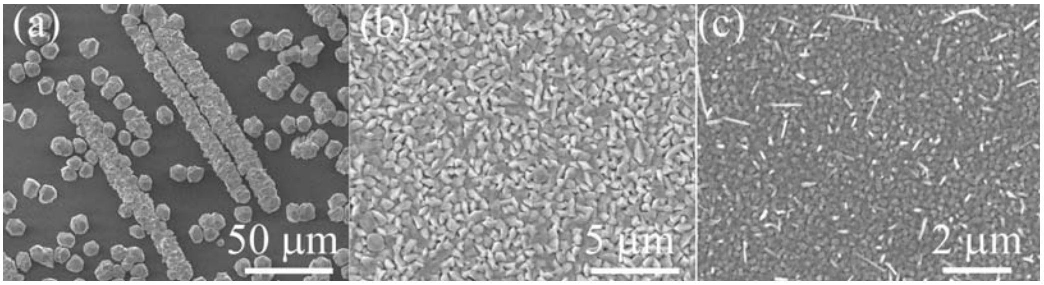

Figure 25: SEM images of WO_3 growth using 4N5 powder showing the morphology variation at (a) 870 °C and (b) 750 °C, and (c) 408 °C. Growth with 5N powders exhibited almost the same morphology as that of 4N5 and is not shown hereby.

3.3.2 Tungsten Oxides: Seeded Growth

As mentioned in Sec. 3.3.1, growth using higher purity tungsten powders primarily produced thin film deposition; and growth using 3N powder was plagued with the impurity effect producing sodium tungsten oxide NW instead of tungsten oxide NW. New growth method was thus explored to obtain WO_3 NWs. In this study, a seeded growth approach was developed and proved to be a successful alternative way.

Understanding the oxidation of tungsten powder was the key to obtain high yield in seeded growth. Oxidation of tungsten had been investigated under diverse conditions, such as at elevated temperature (>1100 °C) and oxygen pressure on the order of Torr,[80] and at temperatures ranging from 20 to 500 °C under atmosphere pressure.[81] WO_x NWs were readily found when tungsten (foil, wire, or powder) was oxidized under various conditions.[57, 65, 82] However, the study on tungsten powder oxidation behavior between intermediate temperature range and under low pressure was still rare. This thesis studied the oxidation of tungsten powders with diverse size within temperature range from 500 to 1000 °C and under several mTorr oxygen partial pressure. It was illustrated that using tungsten powder as seed was an economic approach to obtain high yield of WO_3 nanowires at relatively lower temperature. It was also demonstrated that there was an optimal tungsten powder size under current experimental conditions for the seeded growth. This observation provided some insight on the role of tungsten powder as source material in CVD growth of WO_x.

Commercial available tungsten powders with different size were usually associated with purity variation as well. Four kinds of tungsten powders were used as precursor to prepare WO_3 NWs, as already summarized in Table 6. The dimensions of tungsten powder were obtained by measuring the average size in SEM micrographs. A systematic investigation was performed on the oxidation behavior of tungsten powder to evaluate the temperature effect, size-dependence, and influence of oxygen partial pressure.

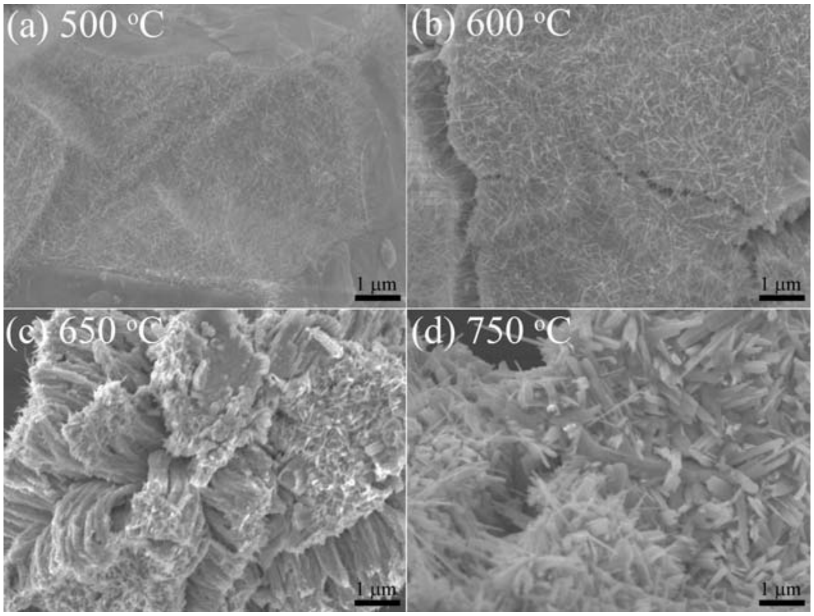

Figure 26: W powder oxidation: temperature effect. SEM graphs of 99.9% (3N) tungsten powder oxidization at different temperatures of a) 500 °C, b) 600 °C, c) 650 °C, d) 750 °C, showing the optimal temperature for local formation of nanowires is between 600-650 °C. Oxygen flow rate is 1 sccm.

Fig. 26 illustrated the effect of temperature on the morphological change and surface nanowires formation of 3N powder. At 500 °C, most tungsten powder retained its original shape and a layer of tiny dense NWs began to grow. When temperature was increased to 600 °C, 3N powder started to crack with longer NWs on the isolated surface. Further increase of temperature led to irregular shapes of tungsten power and aggregation of NWs, giving rise to the nanorods and bunched or bundled structures. It could be determined from the morphology variation that the optimal seeded growth temperature for 3N powder was in the range of 600 to 650 °C.

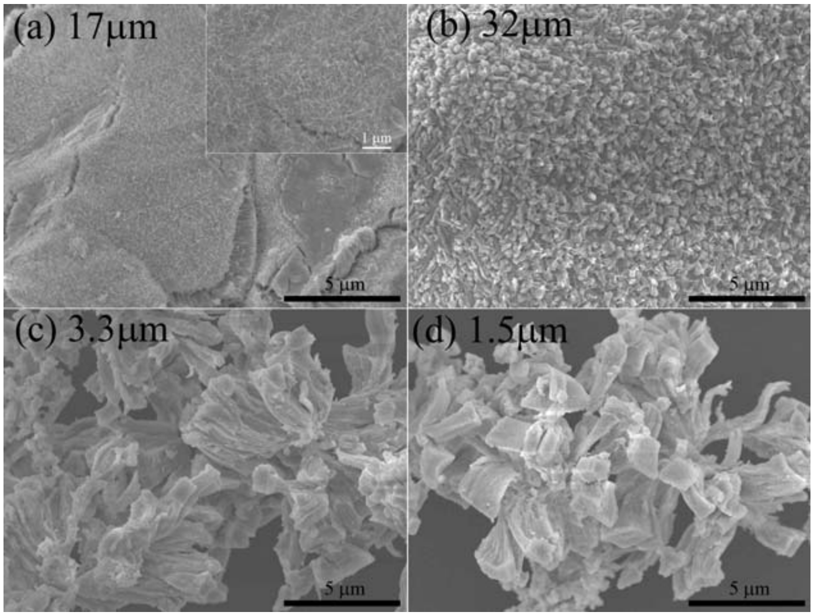

Figure 27: W powder oxidation: size effect. SEM graphs illustrating the oxidization of four different size of tungsten powders at 600 °C and 1 sccm oxygen flow. a) 17 μm, b) 32 μm, c) 3.3 μm, d) 1.5 μm.

Fig. 27 depicted the oxidation of different sizes of tungsten powder under the same experimental conditions. In contrast to the morphology of 3N powder shown in Fig. 26, 3N5 powder surface was primarily covered with sub-micron particles as well as some short tiny NWs; whereas 4N5 and 5N powder were thoroughly oxidized, showing branched flowers feature. This dramatic difference could be explained in terms of surface energy and oxygen diffusion. With smaller dimension, the increased surface-to-volume ratio and short diffusion path both lowered the energy barrier of oxidation.[83] When it came to seeded growth, however, the powder size distribution was an important factor to give uniform NWs deposition. Since the size distribution of 3N powder was more uniform than that of 3N5 powder (Fig. 12), this study used the former as seeds.

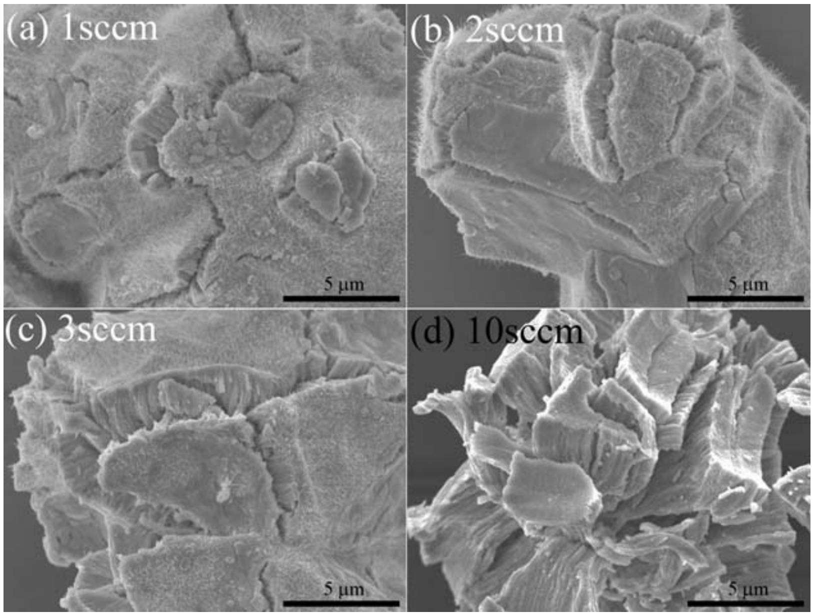

Figure 28: W powder oxidation: oxygen pressure. SEM graphs of 3N tungsten powder oxidization at 600 °C under different rates of oxygen flow: a) 1 sccm, b) 2 sccm, c) 3 sccm, d) 10 sccm. The oxygen partial pressures were 13 mTorr, 23 mTorr, 32 mTorr, and 82 mTorr, respectively with background pressure subtracted.

Fig. 28 depicted the morphology change of 3N powder with respect to varied oxygen partial pressure. When the oxygen flow was lower than 3 sccm, 3N powder almost stayed as the same with cracks separating the dense layer of NWs. When oxygen flow was increased to 10 sccm, the 3N powder exemplified an enlarged version of that for 4N5 or 5N powder under 1 sccm oxygen flow. This observation again was supported by the surface energy explanation.

With all above oxidation experiments, favorable conditions for local growth of NWs were extracted to perform the seeded growth. The growth was performed by placing high purity tungsten powders (4N5 or 5N) in center heating zone and substrate with 3N tungsten powders in downstream location, where the temperature was about 600 °C. The temperature profile, source, and substrate locations remained essentially the same as in Fig. 11 except the presence of 3N powder on substrate. In all experiments, tungsten powders were uniformly distributed by sliding two pieces of substrates, and the growth time was kept at 4 h. As shown in Fig. 29b, a dense NWs array was obtained on tungsten powder seeds with individual wires of length up to 10 μm and diameter about 50 to 200 nm, according to the measurements made in the close-up view. Each tungsten powder stood as independent growth site (Fig. 29a) with film growth on the substrates, a common feature without using tungsten powder as seed under current experimental conditions. It was occasionally observed that NWs growth was initiated adjacent some tungsten powders. This phenomenon was correlated to the local trap of vapor flow since it was more often found among the enclosed area by tungsten powders. It is also found that the diameter of NWs decrease as the distance between powders and upstream edge increases. This is a combination effect of lower temperature and reduced

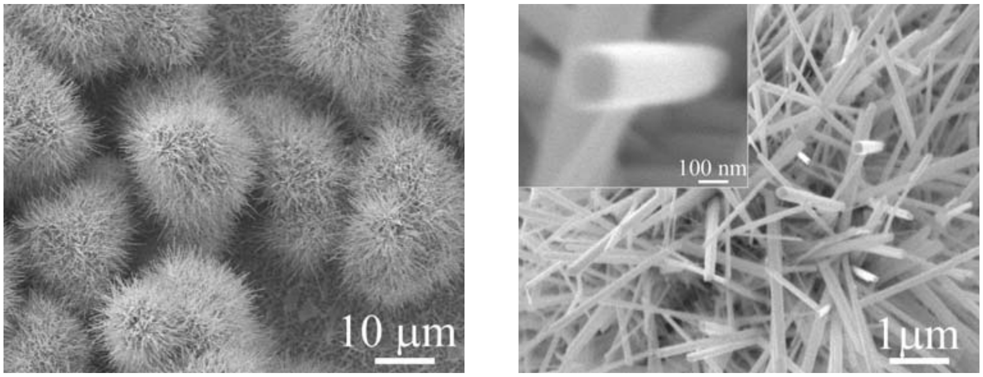

(a) (b)

Figure 29: SEM characterization of WO_3 seeded growth. (a) SEM graphs of WO_3 NWs on SiO_2/Si substrate. (b) A high magnification view showing uniform NW growth and close-up view of one NW.

WO_x growth species supply.

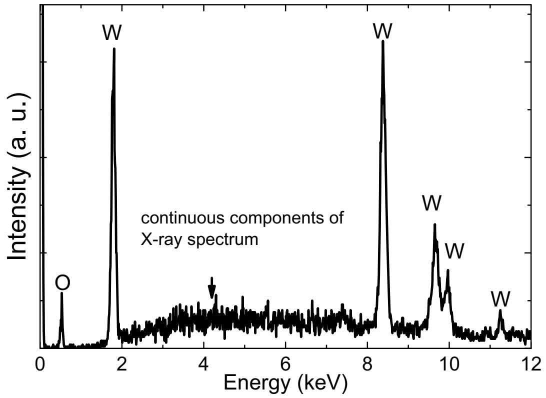

Figure 30: Composition analysis on the WO_3 NWs from the seeded growth with EDX.

EDX analysis on the WO_3 NWs from the seeded growth is shown in Fig. 30. Only W and O elements were detected on the NW array. The background level from 3 to 8 KeV was a manifestation of the continuous components of X-ray spectrum.

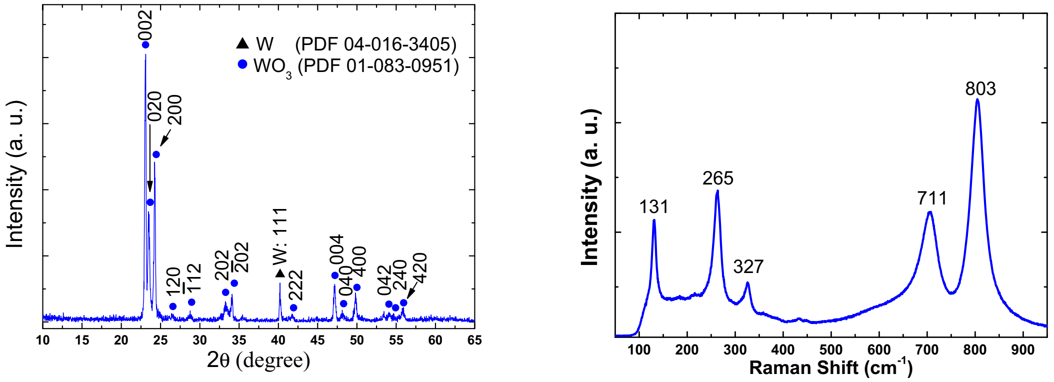

(a)

(b)

Figure 31: Characterization of seeded growth WO_3: XRD and Raman. (a) XRD pattern of as-prepared sample indicating the WO_3 phase and the presence of metallic core, and (b) Raman spectrum on NWs region showing the feature of WO_3.

Fig. 31a displayed the XRD spectrum of one typical sample. The peaks under circular symbol were identified to be the monoclinic WO_3 phase (ICDD PDF 01-083-0950, a=7.3008 Å, b=7.5388 Å, c=7.6896 Å, β=90.89°), while the peak under the triangular symbol was indexed to cubic tungsten phase (ICDD PDF 04-16-3405, a=3.157 Å), in agreement with the EDX analysis (Fig. 30). This indicated during the WO_3 seeded growth of 4 h heating at 1000 °C, the tungsten powder in the low temperature region (600-700 °C) was not entirely oxidized. Micro-Raman scattering spectroscopy was performed on the as-synthesized sample as well. During Raman examination, the laser spot was carefully focused onto the NWs on powders, and several inspections on different positions were observed to ensure the reproductivity of spectra data. As shown in Fig. 31b, five distinct bands were well resolved with peaks located at 131, 265, 327, 711, and 803 cm^{-1}, respectively. This pattern was typical features of WO_3, in consistent with previous study.[76, 84] The high background level probably arose from the metallic core.

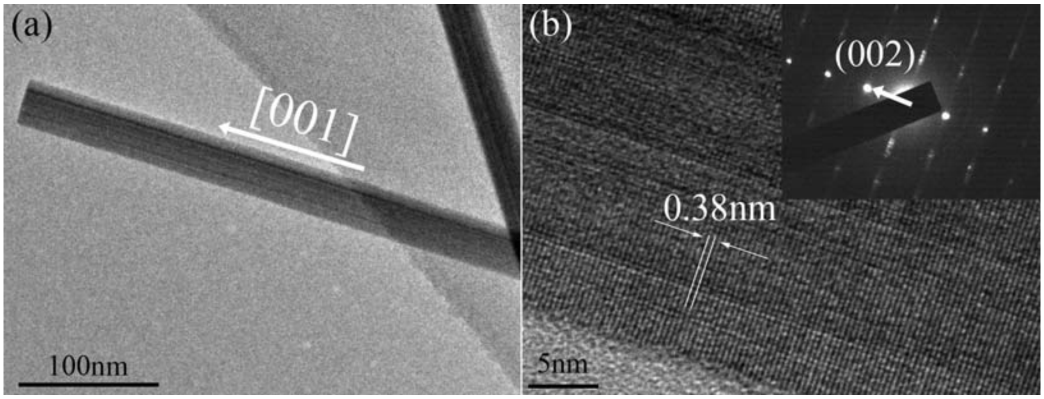

Figure 32: TEM Characterization of WO_3: (a) TEM image of one nanowire with diameter about 40 nm, and (b) HRTEM images showing the spacing is 0.38 nm, corresponding to (002) plane distance.

TEM specimen was prepared by using carbon grid to slightly scratch the as-grown sample. Fig. 32 show the feature of majority NWs. The growth direction was determined to be perpendicular to (002) plane. The streaking in SAED pattern presumably stemmed from stacking defaults during WO_3 NW growth. This study also found some NWs exhibit high crystalline quality, as revealed by the TEM analysis in Fig. 33. The NW grew normal to (002) plane with a measured lattice spacing of 3.79 Å, which was favorably compared to the XRD peak at 23.07° (7.7103 Å). The sharp SAED pattern and clear phase contrast in HRTEM demonstrated strong evidence of good crystallinity. This formation indicated current growth parameters could have promising potential to obtain highly crystalline WO_3 NWs in large scale.

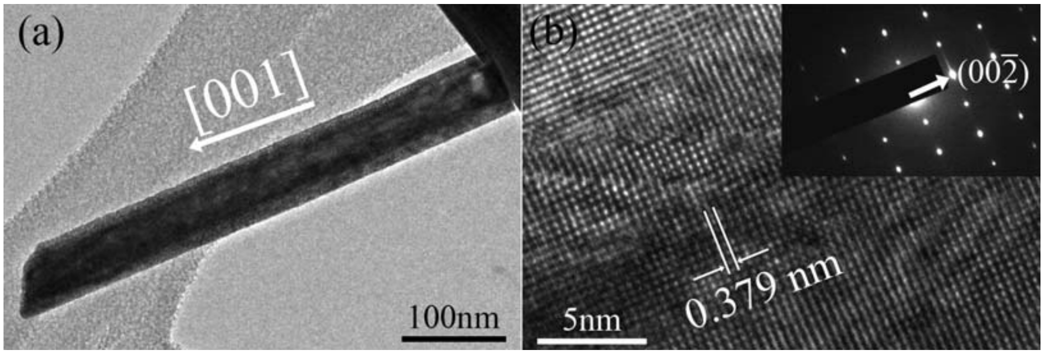

Figure 33: TEM Characterization of WO_3: (a) TEM image of one nanowire, the diameter is about 70 nm, and (b) HRTEM images showing the spacing is 0.379 nm, corresponding to (002) plane distance.

In regarding to the formation of NWs on tungsten powder itself, this study assumed the driving force was related to interfacial strain between W and WO_x. Oxidation of tungsten proceeded slowly at room temperature and an oxide layer of 100 Å was found on the surface of tungsten foils.[81] The tungsten powder used in current study would be covered by a thin oxide layer as well. During oxidation, different oxidation rates existed for different crystallographic orientations on the tungsten powder. Oxidation occurring at boundaries and defects were thermodynamically preferred.[85] Compressive strain gradually accumulated at the tungsten oxide/tungsten interface, which might limit the diffusion rate of oxygen at temperature lower than 500 °C.[83] At elevated temperature, cracks primarily occurred, as observed in Fig. 26. When heated up, tungsten and the oxide shell probably relaxed the strain by converting into sub-stoichiometric NWs, a similar process as suggested by Klinke et al. in the chemically induced strain growth of tungsten oxide NWs.[63] It is worth noting that tungsten oxide nanowires could also formed when WO_3 was reduced.[86] The elongation of WO_x was thermodynamically favorable during the conversion from metallic tungsten to tungsten oxide as well. Local evaporation-condensation process might also contribute to the formation of NWs on tungsten powder.

The enhanced yield of NWs obtained via the seeded growth could be explained by a vapor-solid (VS) mechanism. External supply of growth species condensed onto the powders and substrate simultaneously, promoting the elongation of NWs on powers as well as resulting film growth on substrates. The local NW density in oxidation experiment was much higher than that of seeded growth. It was reasonable to presume that during the seeded growth, several NWs in a small region on powder coalesced, as evidenced by the bundled structures. At last, the author would like to point out that when low purity tungsten powder (3N) was used as source, sodium tungsten oxide nanowires were found to be dominant in the final phase. The details have been published.[87] It seemed surprising that when 3N powder was used as seeds, only WO_3 nanowires were obtained. This result was attributed to the lower temperature and significantly reduced amount of 3N powder used in the seeded growth, compared with the conditions used in Ref.[87]. The source material in the seeded growth is not limited to high purity tungsten powder. Instead, any material that could produce appropriate growth vapor could be employed, indicating the versatility of this approach.

3.3.3 Tungsten Oxides: Other Method

Another interesting approach for WO_3 NW growth were also found in this study, producing WO_3 NWs of high crystalline quality. The method was supposed to be related to the vapor flow dynamic in the deposition region. As shown in Sec. 3.3.1, the non-seeded growth using high purity W powers mostly led to thin film growth on the substrate of 1 inch long. In

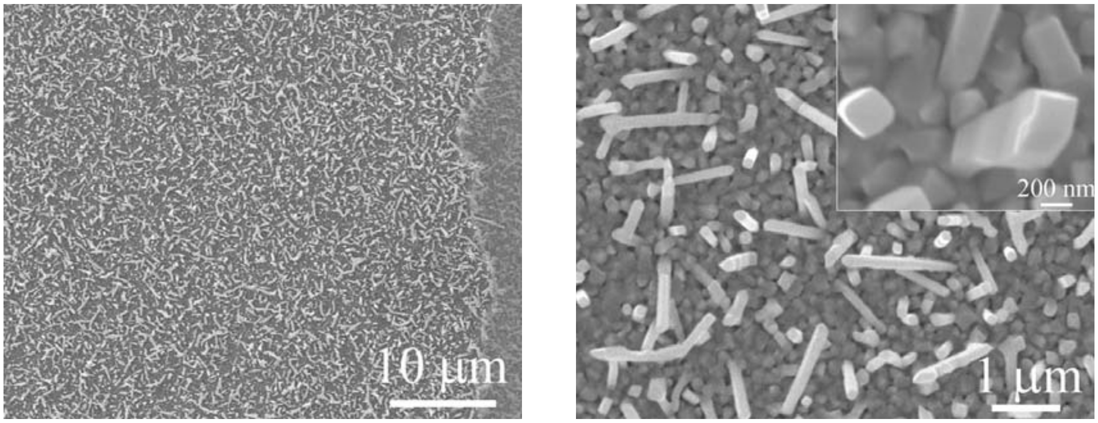

(a) (b)

Figure 34: Characterization of flow growth WO_3: SEM. (a) Low magnification SEM image showing dense array of NWs, and (b) High magnification SEM image of NWs grew out of layer and close-up view on individual wire.

contrast, it was found that when two shorter substrates were closely placed together, the WO_3 NW yield was significantly enhanced in the second substrate located in lower temperature region. For instance, substrate 1 (sub1) was located at 6.75 to 7 inch (Fig. 11 horizontal axis on page 34), and substrate 2 (sub2) was placed in close vicinity of downstream end of sub1. W source was moved to 5 inch, and 0.3 sccm O_2 was used to reduce the WO_x vapor pressure. Deposition on sub1 was characterized by thin film, similar to those shown in Fig. 25b. However, deposition on sub2 (Fig. 34a) was in sharp contrast to that shown in Fig. 25c, although they were both located in the low temperature region of reaction chamber. The NW density was dramatically increased when two separate substrates were employed. The NWs had length about 1 μm to 2 μm and diameter about 200 nm. Close-up view (inset of Fig. 34b) shows the NWs exhibited sharp facets, implying its high crystalline quality.

The growth mechanism here can be explained by aforementioned VS process as well. Both local flow and temperature played an vital role in the formation of dense NW array. Splitting one substrate into two presumably introduced some fluctuation in the vapor flow.

In spite of the high crystalline quality, the WO_3 was not long enough, and the yield was limited by the evaporation of source materials; therefore this approach was not seriously pursued in this study.

3.4 Summary

A systematical investigation of WO_3 nanowire growth using CVD method with tungsten powders as precursor was performed. Four kinds of tungsten powder sources were used, and the sodium impurity effect was throughly studied. $Na_5W_{14}O_{44}$ NW was first reported from this study; the crystal structure was investigated in detail, and HRTEM images were obtained. Besides, the Raman vibrational spectroscopy of $Na_5W_{14}O_{44}$ was also identified. The presence of sodium tungsten oxide phase indicated that the CVD growth of WO_3 was extremely sensitive to Na contents. The insight of WO_3 growth kinetics we have gained from this study could help establish a systematic connection between the interaction of transition metal oxide and alkali metal ions, thereby turning this deleterious effect into a beneficial approach of controlled growth. In fact, favorable results has been observed on both WO_3 and MoO_3 1D nanostructures syntheses using NaOH treated Si substrates. Details will be presented in Chapter 4 and 6, respectively. Moreover, two alternative approaches of WO_3 NWs were also attempted, and the seeded growth method proved effective for large scale growth.

CHAPTER 4: VAPOR-SOLID-SOLID GROWTH OF MOLYBDENUM OXIDE

4.1 Introduction

In this work, a new growth mechanism of molybdenum oxide (MoO_3) 1D structures was discovered, manifest as MoO_3 long nanobelts and micro-towers. The samples were synthesized using a group of alkali metal based catalysts, including NaOH, KI, and Na_2CO_3. In contrast to the sole axial growth found in the conventional catalyst-assisted process, two different growth modes were observed for the 1D MoO_3 deposition: transverse and axial growth. In the transverse mode, the 1D structures grew parallel to the catalyst-deposition interface with catalyst particles on the side surfaces; whereas in the axial mode, the crystal grew perpendicularly to the catalyst-deposition interface. The growth modes were explained by a modified vapor-solid-solid (VSS) mechanism, and the growth kinetics were explored in detail.

The remaining sections are organized as following: a brief review on previous studies of MoO_3 is given first, followed by the synthesis method in this dissertation. Emphasis will be placed on morphological and crystal structure characterization of 1D MoO_3 nanostructures and the verification of proposed VSS mechanism. This chapter concludes with a summary of VSS growth and preliminary results on morphology controlled MoO_3 nanostructures.

4.1.1 Properties and Applications of Molybdenum Oxide

Molybdenum oxide (MoO_3) crystallizes in three phases: orthorhombic α-MoO_3, monoclinic β-MoO_3, and the metastable hexagonal h-MoO_3.[88, 89] α-MoO_3 phase (hereafter

MoO_3) exhibits anisotropic structure with strong bonding along [001] and [100] direction while van der Waals interaction along [010] direction.[90] Due to this unique structure, MoO_3 has been found to have several important properties and a wide range of technological applications, such as electrochromism and photochromism,[91] lubricants,[92] photocatalysts,[93] and gas sensor, including CO,[94] NO_2,[95] H_2,[25] and ethanol.[96] Moreover, other features arise when nanoscale MoO_3 is specifically prepared, e.g. field emission.[97, 98] As a layered hosting material, MoO_3 can be further modified by intercalating with alkali ions[99–101] and even divalent ion.[102] This structural richness has enabled improved performance in Li-ion[103] and sodium-ion batteries.[104] In combination with TiO_2 forming a core-shell structure, these nanoparitcles were reported to lower the photon absorption energy of TiO_2.[105] When MoO_3 was combined with Ag as layered structure, transparent conducting behavior was observed.[106] In addition, MoO_3 has been a good precursor for preparing other useful materials, such as MoS_2 fullerene[107] and few layer MoS_2.[108] Recently, 2D atomic layers attract intensive research efforts, and MoO_3 can be used in fabricating the van der Waals heterostructures.[109]

The coordination number of Mo in MoO_3 is six; thus MoO_6 octahedra are often considered as the building block. As shown in Fig. 35, the layered structure consists of zig-zag rows of edge-sharing MoO_6 octahedra, and the rows are mutually connected by corners. Another point of view emerges when one considers the fact that four of the six surrounding O atoms are at distances from 1.67 to 1.95 Å, while the remaining two are as far as 2.25 and 2.33 Å, MoO_3 could also be considered as chains of MoO_4 tetrahedra connected by the sharing of two oxygen corners with two neighbouring tetrahedra in *c* axis. The infinite chains of MoO_4 tetrahedra form half-layers in the *ac* plane. Two half-layers, which are stapled along

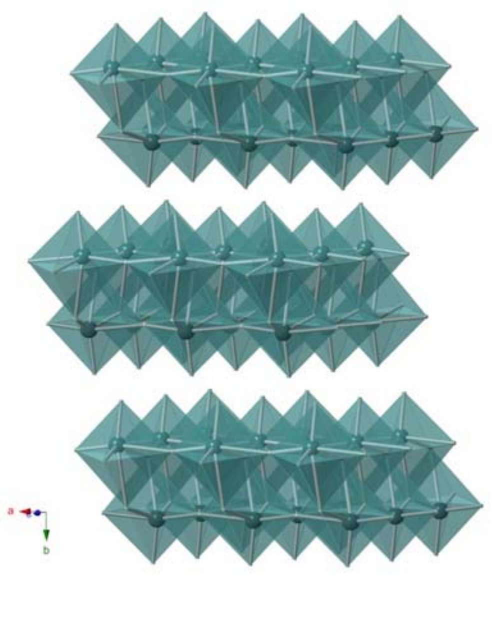

Figure 35: MoO_3 crystal model.

b axis, build up one MoO_3 layer.[110] This view stresses that the MoO_6 octahedra are rather distorted.

It is known that a series of molybdates form when alkali metal ions are incorporated into the MoO_3 lattice, and the structures are summarized in Table 11. Due to the weak cation-oxygen bonding, alkali metal cations only introduce small perturbations into the energies of Mo−O matrix in comparison to cations of other elements. And no mixing of vibrations of the cationic sublattices with that of Mo−O lattices is anticipated. So the structural features of Mo−O polyhedra are dominating factors affecting the vibration frequencies and thermodynamic values of the molybdates.[70]

Molybdenum bronze also exhibits intriguing features; for instance, charge density wave (CDW) states[11] was found in blue bronze $K_{0.3}MoO_3$, which can be prepared by electrolytic reduction of K_2MoO_4 and MoO_3 melt.[111] $K_{0.3}MoO_3$ stays as monoclinic phase at room

---

[11] In CDW states, conductivity is non-Ohmic above a threshold electric field.

Table 11: Crystal structures of alkali metal molybdates and tungstates

formula	structure
$A_2O{:}MO_3{}^{a}$	isolated tetrahedral MO_4 anions
$A_2O{:}2\,MO_3$	chain-type anions of MO_4 and MO_6
$A_2O{:}3\,MO_3$	chain-type anions of MO_5 and MO_6
$A_2O{:}4\,MO_3$	chain-type anions of MO_6

^{a} A = Li, Na, K, Rb, Cs; M = Mo, W;

temperature with lattice parameter $a = 18.249$ Å, $b = 7.561$ Å, $c = 9.856$ Å, and $\beta = 117.54^{\circ}$ and exhibits a semiconductor-to-metal transition at 180 K. Electrical transport measurements yield an highly anisotropic ratio of DC conductivities of 1:10:1000. Along this high conducting axis, metallic reflection behavior is confirmed by optical measurements. Therefore, this blue bronze $K_{0.3}MoO_3$ is also known as quasi-1D metal.[112]

4.1.2 Review of Synthesis Methods of Molybdenum Oxide

Researchers have been exploring a variety of methods to synthesize different MoO_3 nanostructures. Only a brief introduction will be given here, since these efforts has been well documented in several review articles.[90] Most of these methods can be categorized into two groups: solution-based hydrothermal procedures [113–116] and chemical vapor deposition approaches.[89, 97, 98, 117–119] Both methods have their own merits. Hydrothermal process usually needs lower temperature (<300 °C), but the reaction often requires tens of hours, and the sample requires several post-growth processing steps; whereas vapor deposition demands relatively high temperature (>500 °C) with a few hours reaction time. Both methods are scalable for industrial applications. However, the hydrothermal treatment seems to allow more nanostructures control than does the vapor deposition method. Nanobelts,[113] helical nanosheets, nanoflowers, nanorods,[115] and nanoribbons[116] were obtained by the former one while nanoflakes,[120] nanobelts,[121] and nanowires[10, 98] dominated the product morphology for the latter one. The assistance of Au catalyst in vapor deposition only altered the orientation[119] or served as preferred nucleation sites[122] without producing new MoO_3 structures. Chithambararaj et al. prepared hexagonal MoO_3 nanocrystal via hydrothermal method and demonstrated the photodegradation of methylene blue (MB) under visible light.[123] The efficiency dependence on catalysis/dye ratio, light intensity, and temperature was studied. h-MoO_3 was mostly synthesized using solution methods, where NH_4^+ and OH^- were possible structure directing and stable agents. The band gap of h-MoO_3 estimated from diffusion reflection spectrum is 2.8 ~ 3.0 eV. Hexagonal phase of MoO_3 is readily identified by the XRD pattern (strong peak at $2\theta = 20°$). It is worth noting that in spite of these numerous growth of MoO_3, reports on catalytic growth are still scarce.

4.2 Experimental

The reactants used in this study were listed in Table 12. All reactants were used as received without further processing.

Table 12: Reactants list of MoO_3 growth

Material	Stock No	LOT	Purity	Vendor
NaOH	S318-500	070241	99.8%	Fisher Scientific
NaI	11665	K11W054	99.9%	Alfa Aesar
KI	42857	H06Z051	99.9%	Alfa Aesar
Na_2CO_3	33377	114X012	99.95%	Alfa Aesar
Molybdenum	00932	I07S024	99.9%	Alfa Aesar

Silicon substrate was first cleaned according to the procedures stated in Sec. 2.1.2 on page 11 and directly used in non-catalyst-assisted experiment. In catalyst-assisted growth, hydrophilic Si substrates were first drop-cast with NaOH (or KI, Na_2CO_3) solution (54

μL 10 mM) and then air dried in a chemical fume hood before experiment. Other alkali ions-containing substrates, such as glass (Fisher Scientific, microscope slide, 12-549) and indium tin oxide (ITO) coated glass (Delta Technologies, 25Ω), were cleaned by the same routine except the absence of plasma cleaning and subsequent aqueous solution dipping. Mica was cleaved right before growth without other treatment. In a typical catalytic synthesis (Fig. 36), molybdenum powders were loaded at the center of the reaction chamber with the receiving substrate placed at the downstream. The reaction chamber was first pumped down to ~10 mTorr, and then brought up to ~200 mTorr with 10 sccm O_2 and 10 sccm Ar. The

Table 13: Physical constants of reactants

Material	MP(°C)	BP(°C)	Reference
NaOH	318	1388	[124]
NaI	651	1300	[124]
KI	681	1330	[124]
Na_2CO_3	851	Not determined	[124]
Na_2MoO_4	687	Not available	[124]
MoO_3	795	1155	[124]
MoO_2	1100(decomp)	Not available	MSDS

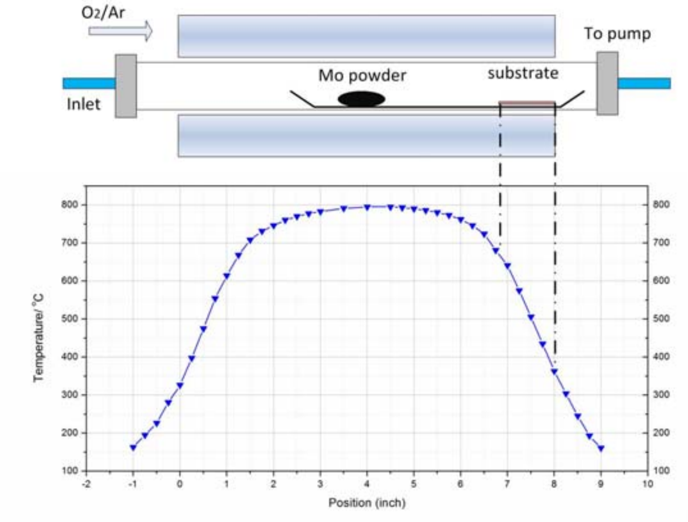

Figure 36: CVD growth setup of MoO_3. The triangular labels were measured points at ambient environment.

heating temperature at the center was ramped up to 800 °C in 30 min and lasted for 120 min. Then the heating power was turned off, and the chamber was allowed to naturally cool to room temperature. During the growth, the growth temperature along the substrate was about 620 °C to 300 °C according to the temperature profile measured at atmospheric pressure. Non-catalytic growth shared the same procedure except the NaOH treatment on Si substrates.

4.3 Results and Discussion on Molybdenum Oxide

In this section, the growth of MoO_3 on bare Si substrates was presented first, followed by catalytic growth, both of which were characterized by SEM, XRD, TEM and EDX. Then the catalytic growth mechanism was investigated using NaOH treated Si substrate. The growth mechanism was probed using two series of control experiments. Then, a VSS growth model was proposed and verified. In the end, this growth model was applied onto other substrates with alkali metal ions, and various MoO_3 nanostructures were produced.

4.3.1 Non-catalytic Growth

For MoO_3 non-catalytic growth, this study observed micro-flakes morphology, as shown in Fig. 37. Most flakes exhibited rectangular shape with average thickness of one micrometer and standard deviation σ_D of 0.34 μm.

As shown in Fig. 38, the crystal structure and phase of the as-synthesized specimen were examined by XRD and Raman. The XRD pattern (Fig. 38a) was readily indexed to the orthorhombic phase of MoO_3 (ICDD PDF 05-0508, a=3.9628 Å, b=13.855 Å, and c=3.6964 Å). The space group is $D_{2h}^{16}(Pbnm)$. This crystal structure is indeed a unique example among transition metal oxides, representing a transitional stage between tetrahedra and octahedral

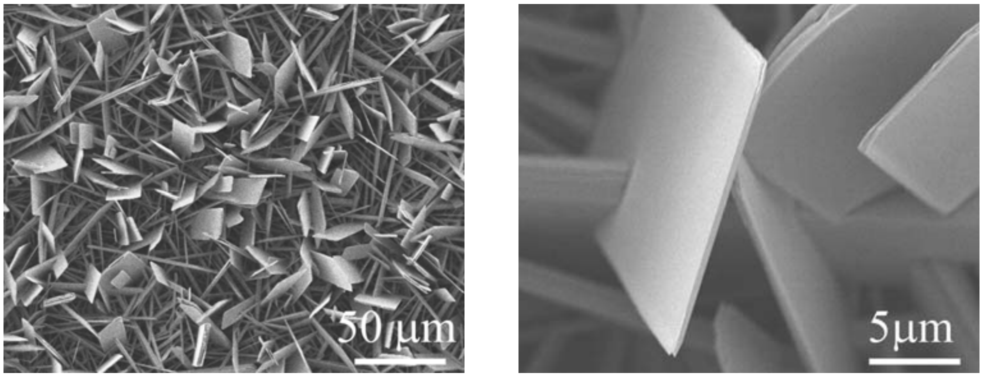

(a) (b)

Figure 37: Representative morphologies of MoO_3 on Si: (a) low magnification and (b) high magnification SEM images of representative depositions of MoO_3 on Si for non-catalytic growth.

coordination.[110] The strongest peak index was (110), suggesting the orientation of MoO_3 was not parallel to the substrate, in consistent with the morphology displayed in Fig. 37a. In contrast, different dominating orientation was observed in the XRD pattern from catalytic growth (Sec. 4.3.3). The Raman spectrum of the as-synthesized specimen also closely

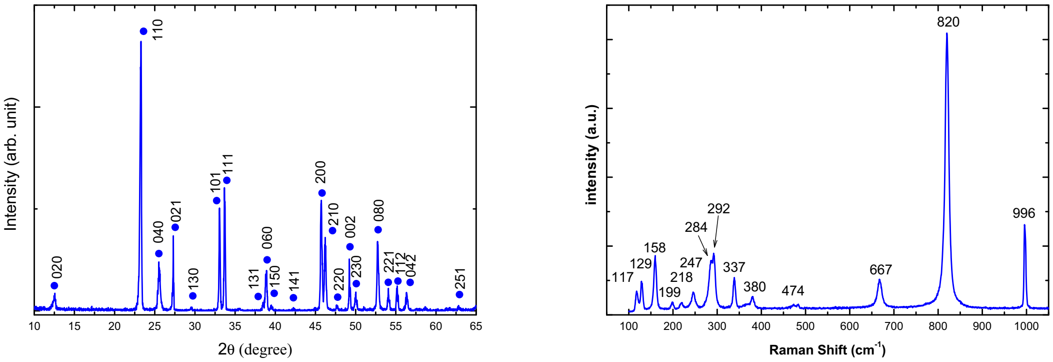

(a) (b)

Figure 38: Crystalline phase characterization of MoO_3 on Si: (a) XRD pattern and (b) Raman spectrum of typical MoO_3 on Si, λ_{ex} = 532 nm.

matched MoO_3 features observed in previous studies.[84, 125] During measurement, the laser spot was carefully focused onto the MoO_3 flakes, and several inspections on different positions were observed to ensure the reproductivity of spectra data. As shown in Fig. 38b, 14 distinct bands were well resolved. The 284 cm^{-1} peak represented the wagging mode for double bond O=Mo=O. The 337 and 380 cm^{-1} peaks were assigned to O−Mo−O bending and scissoring modes, respectively. The 199 cm^{-1} peak and two other weaker peaks at 218 and 247 cm^{-1} represented O=Mo=O B_{2g} twist, A_g chain mode, and O=Mo=O B_{3g} twist mode, respectively. The 667 cm^{-1} peak was assigned to triply coordinated oxygen stretching model resulting from edge-shared oxygen in common to three octahedral. The 819 cm^{-1} peak arose from doubly coordinated oxygen stretching mode between two octahedral. The 996 cm^{-1} peak was from unshared oxygen stretching mode.[126] The Raman symmetry assignment is summarized in Table 14.

Table 14: Experimental Raman peaks assignment of MoO_3 on Si.[126, 127]

this work(cm^{-1})	Sym.		Assignment	
117	B_{2g}		T_c	RCM^a
129	B_{3g}		T_c	RCM
158	A_g/B_{1g}		T_b	RCM
199	B_{2g}	τ	O=Mo=O	twist
218	A_g		R_c	RCM
247	B_{3g}	τ	O=Mo=O	twist
284	B_{2g}		O=Mo=O	wag
292	B_{3g}	δ	O=Mo=O	wag
337	A_g, B_{1g}	δ	O−Mo−O	bend
380	B_{1g}	δ	O−Mo−O	scissor
474	A_g	ν_{as}	O−Mo−O	stretch,bend
667	B_{2g}, B_{3g}	ν_{as}	O−Mo−O	stretch
819	A_g	ν_{as}	O=Mo	stretch
996	A_g	ν_{as}	O=Mo	stretch

^{a} R chain mode;

4.3.2 Catalyst-assisted Growth

All samples in Sec. 4.3.2 were grown for 2 h, the same as that in Sec. 4.3.1. The only difference in growth conditions from Sec. 4.3.1 was the Si substrate treatment. When NaOH was applied onto Si, the deposition morphologies were changed significantly. Fig. 39 show a comparison of the morphology difference between the non-catalyst growth (Fig. 39a) and the catalyst-assisted growth (Fig. 39b-f) revealed by SEM imaging. The non-catalyst growth morphology has been discussed from Fig. 37 on page 69. Several different structures emerged when catalyst was applied, such as nanobelts in Fig. 39d with length up to hundreds of microns and microtowers in Fig. 39f with diameter around 10 μm. A detailed description of these MoO_3 nanostructures has been published and can be found in Ref.[128].

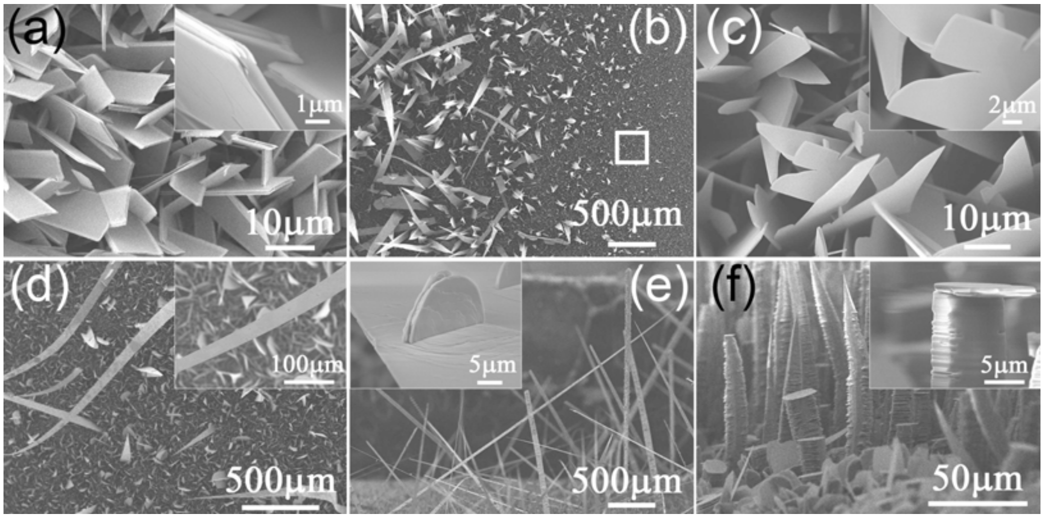

Figure 39: Effect of alkali metal based catalysts on the morphology of MoO_3 depositions: (a) SEM image of rectangular nanoplates grown without catalysts. (b-f) SEM images of different morphologies grown with NaOH catalysts: (b) nanobelts grown on top of dense array of nanoplates,(c) close-up view of the forked nanoplates from an area indicated by the square in Fig. 39, (d) long nanobelts, (e) side-view of ultra-long microbelts, and (f) side-view of microtowers. Insets show detailed features of different MoO_3 structures.

The crystal structures of the as-synthesized specimens were characterized with XRD for the non-catalyst growth (Fig. 40a) and catalyst-assisted growth (Fig. 40b). The calculated lattice parameters and standard database value (ICDD PDF 05-0508) matched favorably, as listed in Table 15. No other phases were found from XRD spectra for both specimens. This result indicated that if there were any catalyst phases present in the catalyst-assisted specimen, they must be of extremely low amount as compared to that of the MoO_3 phase, presumably below the detection limit. The XRD pattern of catalyst-assisted growth shown in Fig. 40b was dominated by the $(0k0)$ family peaks, showing a different preferred orientation from the non-catalytic growth. The reason will be discussed in Sec. 4.3.3. Fig. 40c show low magnification TEM image of a rectangular nanoplate grown without catalysts and the SAED pattern. The nanoplate was exfoliated by ultra-sonication in acetone solution to obtain high-resolution TEM (HRTEM) image; hence, the nanoplate was broken into fragments. The SAED pattern in [010] axis and the HRTEM image (Fig. 40d) show the nanoplate had a (010) top surface and two orthogonal edges along [100] and [001], respectively. For the catalyst-assisted growth, Fig. 40e and Fig. 40f-g confirmed both the forked nanoplate and the nanobelt had a (010) top surface and a growth direction of [001]; while Fig. 40h revealed the microtower grew with (010) layers stacking along a [010] direction. Lattice measurements in Fig. 40d and g indicated a planar distance of 0.38 nm for (100) planes and 0.36 nm for (001) planes. These values were slightly smaller than the standard data for α-MoO_3 and the results from XRD measurements. This deviation in lattice parameters may arise from the error in TEM measurements and/or the lattice distortion of MoO_3 during the electron beam irradiation.[129] These results indicated that all the as-synthesized 1D structures had a layered structure. Raman measurement on the catalytic growth sample revealed similar MoO_3 bands, as already displayed in Fig. 38 on page 69.

Table 15: Lattice parameters of MoO_3 derived from XRD

	a (Å)	b (Å)	c (Å)
Non-catalytic growth	3.963	13.882	3.701
Catalytic growth	3.967	13.865	3.701
PDF 05-0508	3.9628	13.855	3.6964

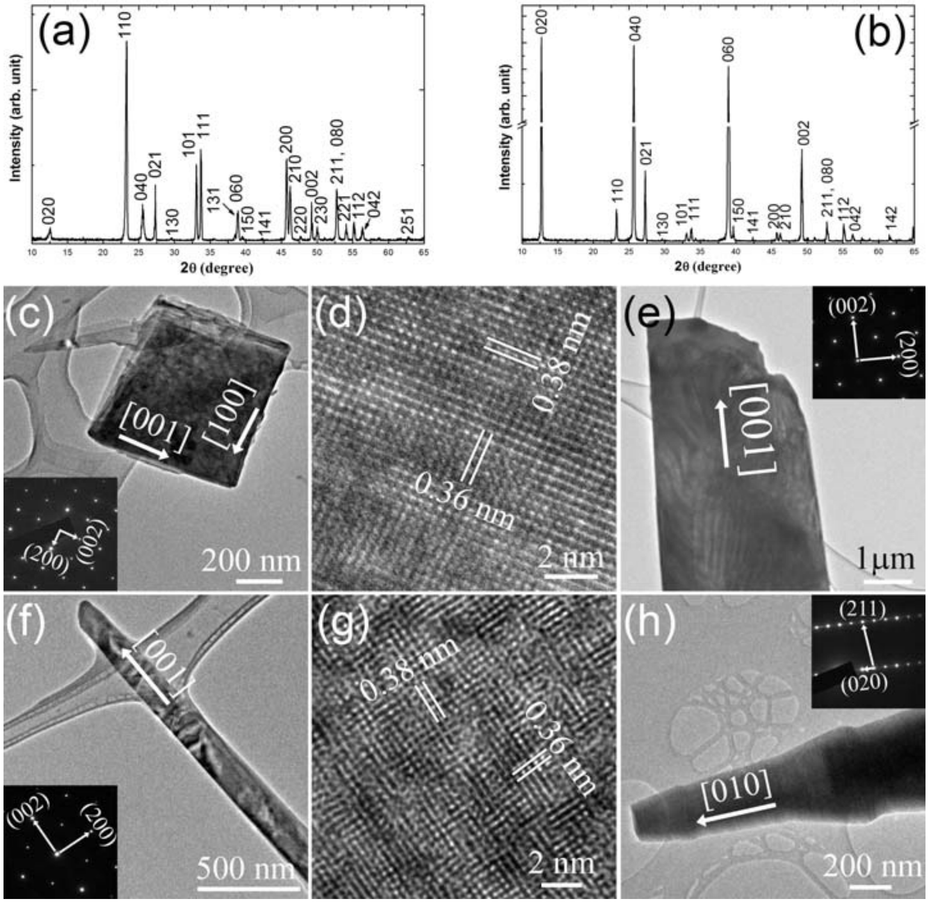

Figure 40: XRD and TEM on MoO_3 growths with and without catalyst. XRD spectra of (a) a specimen grown without catalysts and (b) a specimen grown with NaOH catalysts. (c) Low-magnification TEM image and (d) HRTEM image of nanoplate grown without catalyst. Low-magnification TEM images of (e) forked nanoplate, (f) nanobelt, and (h) microtower, and (g) HRTEM image of nanobelt. Insets show SAED patterns of different MoO_3 1D structures

4.3.3 Growth Mechanism Study

The growth process of the 1D MoO_3 nanoflakes in non-catalytic experiment can be explained by the vapor-solid (VS) mechanism, as proposed in other vapor phase depositions of MoO_3 nanostructures.[130, 131] It has been shown that MoO_3 growth on the NaOH treated Si substrates exhibited dramatic differences. Previous study in our group had found that MoO_3 deposition on ITO glass exhibited new morphologies that were not observed on Si substrates under the same growth conditions, yet the mechanism was not well investigated.[132]

A list of composition difference between glass and Si substrate show the additional elements of Na, K, and Ca, *etc* in glass. Since the concentration of Na is highest among these extra elements, it is most likely that Na content induced the new morphology growth. Therefore, a vapor-liquid-solid (VLS) or analogous mechanism may exist for the MoO_3 growth when alkali metal ions are involved. To provide a proper context, VLS process is briefly introduced here.

VLS was first proposed by Wagner[133] and further developed by Givargizov.[134] This method has become an important strategy for synthesizing 1D nanostructures.[135] Conventionally, a liquid eutectic droplet is formed by catalyst itself or by alloying with the growth material, acting as a trap of growth species. The growth is initialized by supersaturation of the liquid alloy, and subsequently precipitation occurs at the solid-liquid interface. The choice of catalyst usually is among the several noble metals, since they are physically active but chemically stable or inert in most growth scenarios. The growth materials span a wide range, including group IV,[136] group III-V,[137–139] group II-VI,[140] and some metal oxides, such as ZnO,[141, 142] MgO,[143, 144] SiO_2,[145] and TiO_2,[146] to name a few. The catalysts can be Au, Pd, Pt, Ni,[138] Ti, Ga,[145] and even KI. Understanding the interaction between liquid droplet and the solid interface allows for a rich engineering space to fine tune the geometry and structures of the as-grown nanostructures. For instances, the diameter of Si nanowires can be controlled by laser ablated catalyst[147] or well-defined Au nanoparticles.[148] Under proper conditions, axial modulation can produce nanowire superlattices from group IV and III-V materials.[149, 150] Radial composition modulation has also been demonstrated by selectively suppressing VLS process, providing a robust routine for homogeneous or heterogeneous core-shell structures.[151]

Back to the MoO_3 and alkali metal ions, a literature search found that there exists a Na_2MoO_4-MoO_3 phase diagram, as shown in Fig. 41.[152] Note that the phases of the Na-Mo-O system can be written as $Na_2O \cdot nMoO_3$, where n = 1, 2, 3, and 4. Based on this phase diagram, the physical constants of reactants in Table 13, and the growth conditions adopted in this study, it was predicted that the overall reactions occurred in the following sequences. First, Mo powder was oxidized, and MoO_3 vapor was produced and transported to downstream by Ar carrier gas. Then, NaOH reacted with the incoming MoO_3 vapor according to Formula 13.

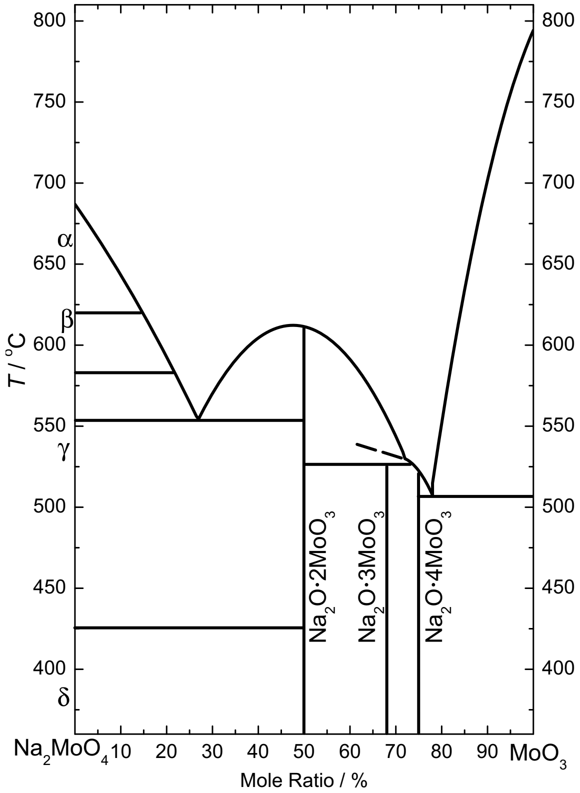

Figure 41: Phase diagram of Na_2MoO_4-MoO_3 reproduced from Ref. [152]

$$NaOH(l) + MoO_3(g) \rightarrow Na_2MoO_4 + H_2O(g) \tag{13a}$$
$$Na_2MoO_4 + nMoO_3 \rightarrow Na_2O \cdot (n+1)MoO_3 \tag{13b}$$

The melting point of Na_2MoO_4 is 687 °C. Based on the open air temperature profile (Fig. 36), the substrate was located in temperature zone between 620 °C and 300 °C. Since the growth temperature range for MoO_3 (525 °C to 300 °C) deposition was mainly below the lowest eutectic temperature of 507 °C, the majority growth of MoO_3 can be explained as a VSS process, which is analogous to the VLS process except that the catalysts remain as solid particles. The actual temperature distribution during growth was different from ambient measurement due to the pressure change and thermal conduction along the Si substrate. It was difficult to acquire the accurate temperatures along the substrate; however, by considering the flow rate, the actual temperature should be higher than that predicted by open air measurement.[153] Thus, VLS mechanism cannot be ruled out completely. The continuous supply of MoO_3 growth species pushed the phase evolution towards high MoO_3 molar ratio end, with n in $Na_2O \cdot nMoO_3$ increasing from 1 to 4. Each site of Na_2MoO_4 continued absorb incoming MoO_3 growth species. MoO_3 precipitated from these seeds when a critical supersaturation concentration was reached, which was about 75% in unit of mole according to Fig. 41. This ratio considerably exceeded that of the usual metal catalyst scenario, such as the Au-Si system. This high solubility accounted for several observations in current experiments: the dimensions of individual deposit was much larger than that of initial particle and the concentration of sodium in final products was extremely low. Based on this aforementioned analysis, the author proposed following hypothesis:

The reaction on NaOH-Si substrate follows the phase diagram, and $Na_2Mo_4O_{13}$ *serves as the catalyst promoting various 1D* MoO_3 *growth in a VSS mechanism.*

In a typical 2 h growth, the MoO_3 weight increase was about 20 mg, which was 1.4×10^{-4} mol. This amount far exceeded the applied NaOH of 5×10^{-7} mol used in the procedure of

Sec. 4.2 on page 66. To capture the early stage growth, the supply of MoO_3 must be reduced in a controlled way. This can be accomplished by tuning two factors: oxygen flow rate and growth time. In this thesis, two series of controlled growth were used to probe the evolution of MoO_3 deposition on NaOH-Si substrate. The first series regulated O_2 flow at 0.1, 1, 3, and 10 sccm with fixed growth time of 15 min. The second series controlled the growth time at 15, 30, 60, and 90 min with fixed O_2 flow of 10 sccm. Two series shared one common growth of 10 sccm O_2 for 15 min.

The oxygen regulated growths were characterized using SEM, EDX, and Raman, as shown in Fig. 42. When O_2 flow was $\leq$ 1 sccm, the deposition show micron size plate growth (Fig. 42a and d). As oxygen flow became higher, the deposition amount increased dramatically, with a morphology of 1D forked plate decorated by triangular shape particles. Micro-Raman scattering was used to probe the phase change during the oxygen regulated growth. The Raman spectra of sodium molybdates was featured with multiple strong peaks located between 800 and 1000 cm^{-1}, which was referred as high-frequency region hereafter. MoO_3 phase show two peaks in this region with the strongest one at about 820 cm^{-1}; $Na_2Mo_2O_7$ phase exhibited four peaks in this region with the strongest one moving to 937 cm^{-1}, whereas $Na_2Mo_4O_{13}$ phase show even more peaks in the high-frequency region with a doublet at 962 and 970 cm^{-1}, respectively.[154, 155] As predicted by the phase diagram (Fig. 41), Raman spectra identified $Na_2Mo_2O_7$ phase in the 0.1 sccm growth (Fig. 42b), and $Na_2Mo_4O_{13}$ phase on the particles in the other three growths (Fig. 42e, h, and k). This observation supported the previous hypothesis about the reaction sequences on NaOH-Si substrate (Formula 13). Element analysis performed on the Raman sites also confirmed the presence of Na, Mo, and O in particles growth and only Mo and O in the plate growth

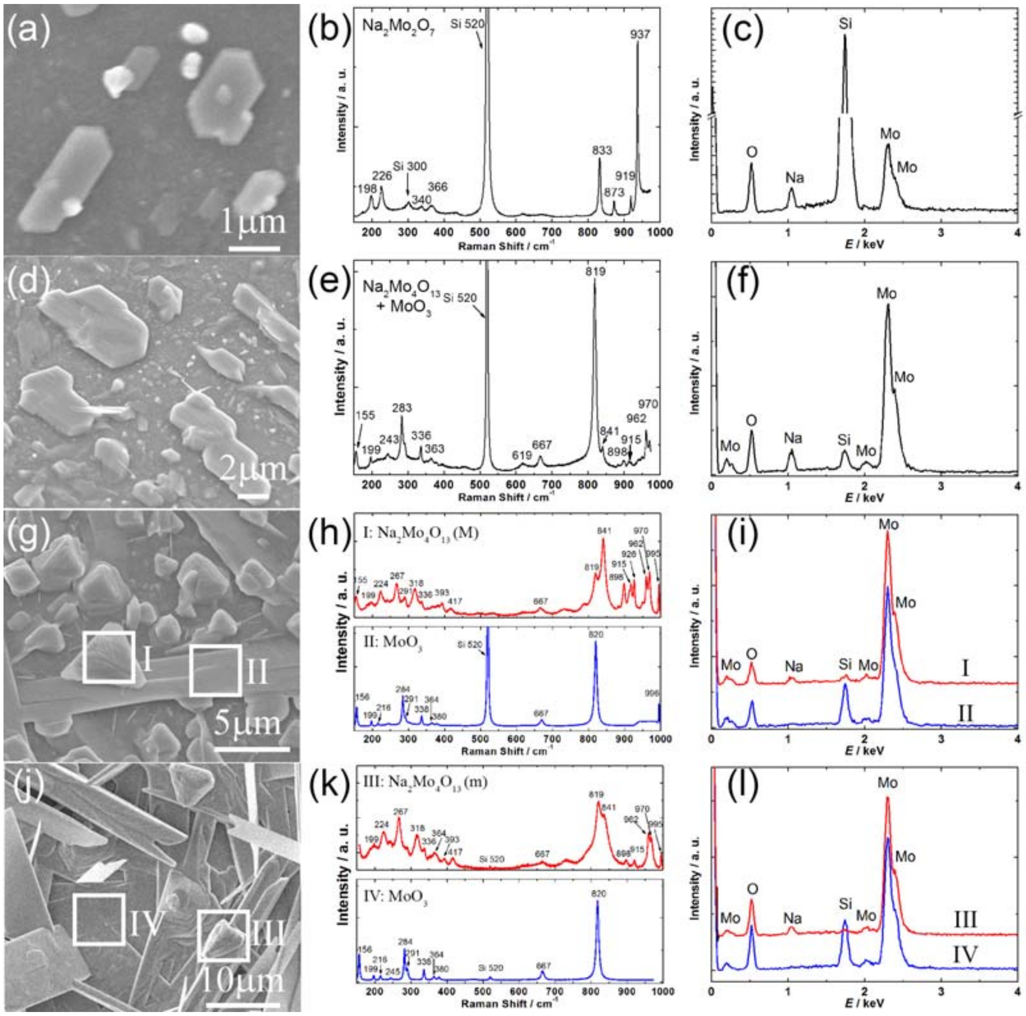

Figure 42: Evolution of the early stage for catalyst-assisted MoO_3 growth: SEM images, micro-Raman spectra, and EDX spectra of the specimens grown for 15 min with different O_2 flows of (a-c) 0.1 sccm, (d-f) 1 sccm, (g-i) 3 sccm, and (j-l) 10 sccm.

(Fig. 42c, f, i, and l). It is worth noting that the absence of Na signal in the forked MoO_3 plate indicated the doping level would be lower than the detection limit of 0.01 wt.% if the Na doping ever occurred. It should also be pointed out the existence of $Na_2Mo_3O_{10}$ phase is in doubt so far, and no Raman fingerprint is reported.[70] Table 16 compared the Raman spectra of sodium molybdates and MoO_3 between present work and literature reports. The morphologies of second series experiment at constant O_2 flow and varied growth time were shown in Fig. 43. The 15 min and 30 min growth show that dense arrays of MoO_3 forked

Table 16: Comparison of Raman shift (cm^{-1}) of sodium molybdates and molybdenum oxide

	$Na_2Mo_2O_7$			$Na_2Mo_2O_7$			MoO_3	
[155]	[70]	this work	[70]	[154]	this work	[127]	[126]	this work
939	939/935	937		995	995	995	996	996
921	920/918	919	970	971	970	819	819	820
873	875/869	873	960	963	962	666	666	667
833	836/828	833	940			471	473	
821	818/815		925		926	378	378	380
768	774/765		910	918	915	366	365	364
741	741/739		895	899	898	338	337	338
524	526/525		870			291	291	291
467	464/460		835	841	841	283	283	284
413	411/411			820	819	246	244	245
369	369/368	366	745			217	218	216
339	340/336	340	650	666		197	197	199
295	296/294			620	619	159	158	156
249	245/245		438			129	129	
226	228/227	226			417	117	117	
	215/215		405			100	98	
200	199/199	198		396	393	84	84	
176			382	381				
137	140/138			368				
120	120/120		348					
84	84/84		335	339	336			

nanoplates with a length of hundreds of micrometers covering the substrate areas at different temperatures. With the increase of the growth time, these nanoplates kept growing and became larger, longer, and denser. Long 1D MoO_3 structures started to grow on top of the nanoplate arrays. For 60 min growth, long nanobelts appeared on top of the nanoplates. For the growth time of 90 min, the nanobelts grew longer, and some grew into microbelts. Microtowers started to grow as well.

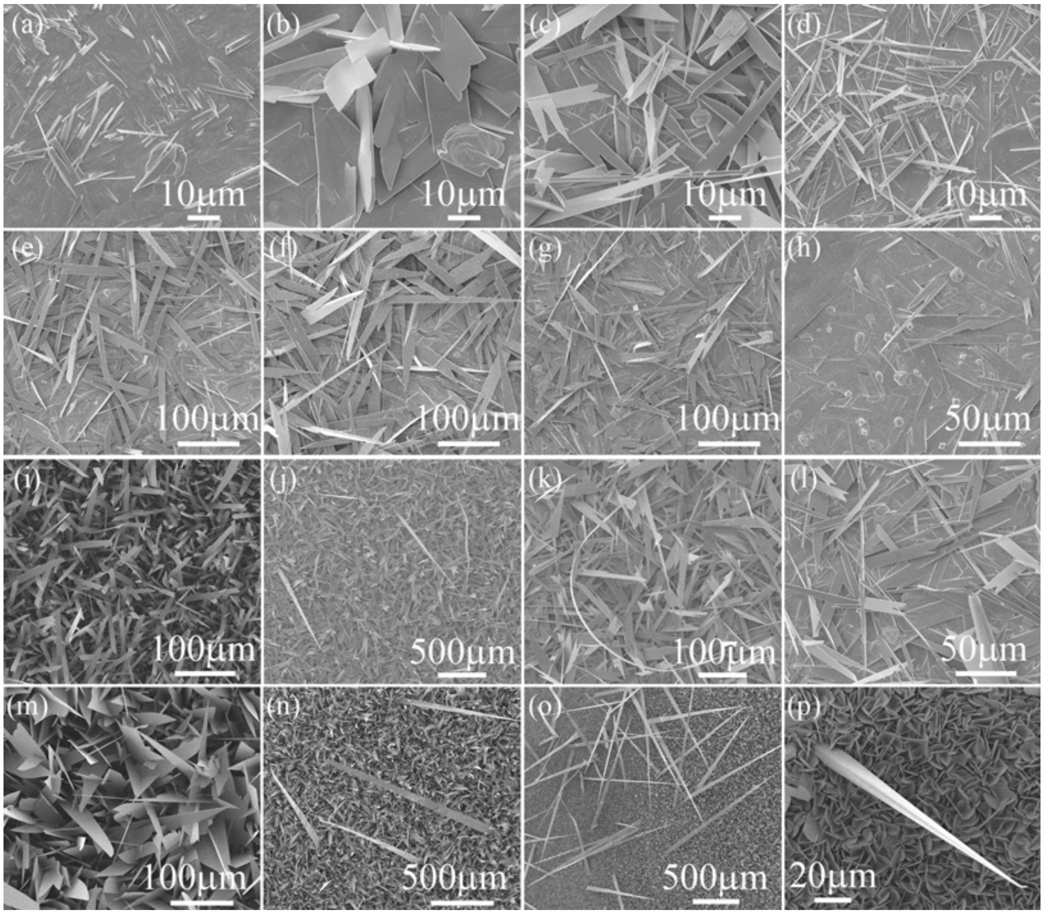

Figure 43: Growth evolution of the second stage of catalyst-assisted growth of MoO_3 1D structures: SEM images of the deposition with growth time of (a-d) 15 min, (e-h) 30 min, (i-l) 60 min, and (m-p) 90 min at growth temperature of 525 °C, 445 °C, 390 °C, and 340 °C, respectively.

To reveal the growth mechanisms for the long 1D structures in the second stage, specimens were carefully examined to locate the catalyst particles. Small catalyst particles ranging from several hundred nanometers to several micrometers were found at different locations of these long 1D structures. As shown in Fig. 44 and Fig. 45, EDX element analysis confirmed the presence of Na, Mo, and O in these particles, suggesting the particles were sodium molybdate catalysts.

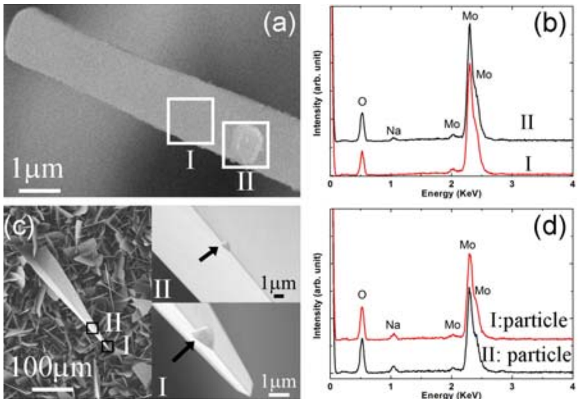

Figure 44: SEM images and EDS spectra identifying the location, morphology, and composition of the catalyst particles on the nanobelt structures: (a-b) a catalyst particle (I) in the middle of a nanobelt (II), (c-d) two catalyst particles (I and II) leading the growth of two perpendicular nanobelts.

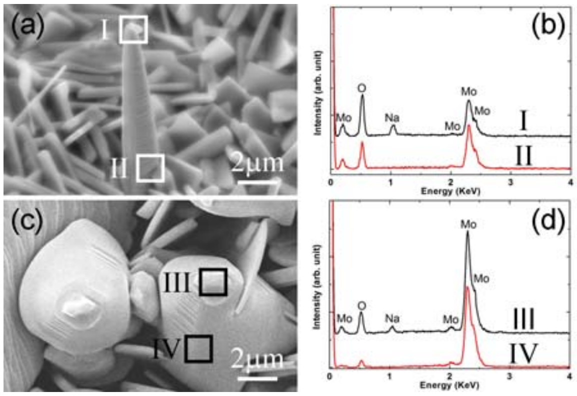

Figure 45: SEM images and EDS spectra for identifying the location, morphology, and composition of the catalysts on the microtower structures: (a-b) a tiny catalyst particle (I) on top of a small cone shaped microtower (II), and (c-d) a catalyst particle (III) on a large and short microtower (IV).

It could be of difficulty to observe the sodium molybdate particles on the as-synthesized belts and towers due to the following two factors, one is the consumption of catalysts, such as evaporation; the other is the unpredictable location of the catalyst. Unlike the conventional

VLS growth where the catalysts were predominantly found at the tip of 1D nanostructures, the catalyst in this study were mostly found at the side wall of long nanobelts, and the location could be on the tip or several microns away from the tip. As for the microtowers, it was even rare to observe Na element. Some observations under similar controlled growth conditions was also listed as following to support the proposed growth model:

1. When no Mo powder was used, NaOH still held onto substrate with some locations exhibiting etching.
2. 1 min growth show plates in high temperature end and irregular shapes in low temperature end.
3. 15 min growth show MoO_3 plates parallel to substrate, with some belts emerging and growing out of the substrate plane. This was presumably due to the growth direction mismatch between different plates. Morphology will also depend on local NaOH concentration. NaOH trace mark turned into connected plates at the original locations, showing the high concentration mediated the morphology evolution. The possible catalyst solid was sitting on the top of plate layer. Some belt-like growth was visible on reaction chamber walls, suggesting the evaporation and transport of Na_xMoO_3 vapor phase;
4. Using NaOH treated hydrophobic substrates, dense tower array growth was found along the edge areas or molten periphery of particles, where 5 min growth already show the initial stage of tower with diameter about 1 μ m, which increased to 10 μ m with prolonged growth.

The growth of MoO_3 on NaOH-Si can be divided into two stages delimited by the emerging of long nanobelts and microtowers. A growth model was proposed to account for the observed morphologies of MoO_3 long nanobelt and tower-like structures.

A transverse growth mode exists with growth direction perpendicular to the catalyst-deposition interface, promoting MoO_3 *nanoplate and nanobelt growth. A axial growth mode akin to conventional VLS process exists, and is responsible for* MoO_3 *tower-like growth.*

The first stage was dominated by transverse growth. The atomic steps in proposed growth model were depicted in the upper panel of Fig. 46. It has been verified that $Na_2Mo_4O_{13}$ formed during the early stage of growth and acted as catalysts. Although the exact phase (liquid or solid) of $Na_2Mo_4O_{13}$ was not known yet in current study, it can be deduced that the $Na_2Mo_4O_{13}$ existed as an active site for the adsorption of incoming MoO_3 growth species. Several pathways could occur after the accommodation of MoO_3 vapor and supersaturation. MoO_3 could precipitate at catalyst-deposition interface, or propagate along catalyst-environment boundary and spread on the already formed MoO_3 surface. Meanwhile, the VS process is not suppressed and MoO_3 adatoms could directly condense on MoO_3 surface. Some unique features of MoO_3 must be taken into consideration to properly evaluate the dominate pathway(s). It has been reported that MoO_3 can spontaneously spread over the surface of supports (*e.g.* Al_2O_3, SiO_2, and Au) to form a monolayer or submonolayer at a temperature (257 °C) well below the melting point.[156] This strong spreading behavior

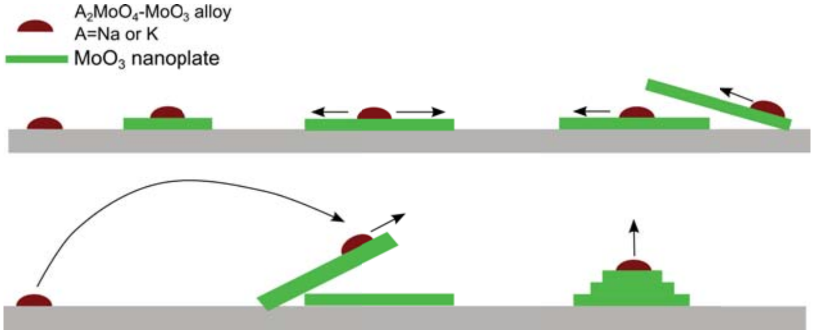

Figure 46: Schematic drawing on the growth steps of the proposed growth mode.

can be explained by the solid-solid wetting process, in which the driving force was the decrease in total surface free energy.[157] Although the detailed transport mechanisms of the spreading are still in debate, it is suggested that the high mobility of the Mo oxide species on substrates and MoO_3 islands can promote the spreading and the ambient gases could further enhance the spreading.[158, 159] Based on above analysis and the final morphology of MoO_3, the dominance of accommodation and spreading pathway in higher temperature part of the growth sample was most possible in this study. Hereby the transverse growth mode was attributed to the strong spreading capability of MoO_3. The final morphology of observed nanoplate and nanobelt was a combined result of VS and VLS growth. On the other hand, the tower-like structures in the second stage followed the axial growth mode in conventional VLS process. The molybdates can be evaporated from the higher temperature end and re-condense onto the lower temperature region. As illustrated in the lower panel of Fig. 46, this could initiate either belt growth or tower growth depending on the locations. The microtowers in this study primarily grew at the low temperature end of the substrate, where the spreading capability of the Mo oxide species was possibly limited. Thus the transverse growth pathway was probably suppressed and axial growth became dominant. The above analysis was substantiated by the multiple observation revealed by SEM imaging, as shown in Fig. 47.

The transport of molybdates in proposed growth model was verified by a side-by-side experiment, as schematically depicted in Fig. 48a. Two substrates, one with NaOH catalyst and one bare substrate, were loaded side-by-side at the same location for the growth. To avoid any possible catalyst transports through surface diffusion, the two substrates were separated with several millimeters gap in between. After the growth, besides the non-catalyst

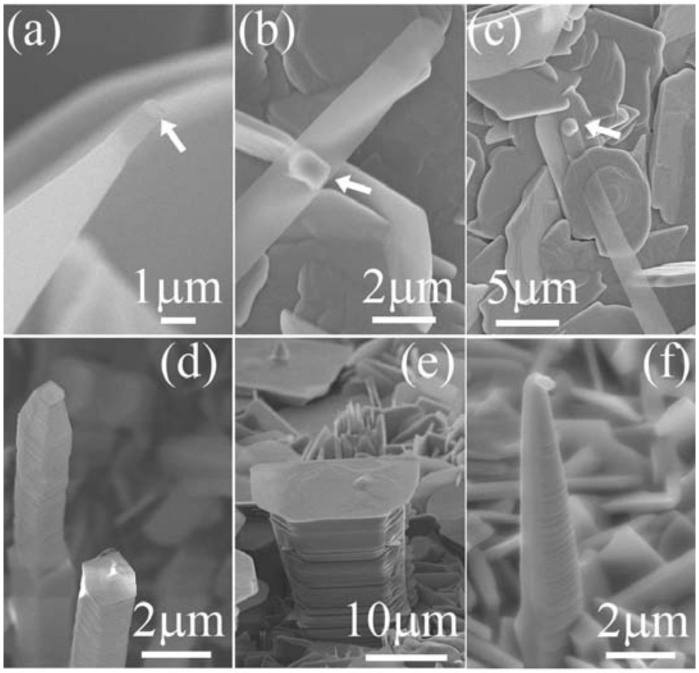

Figure 47: SEM images for catalytic MoO_3 growth: SEM images showing catalyst particles at different locations: (a) tip of a forked nanplate, (b) middle of a nanobelt, and (c) tip of another thin nanobelt; SEM images of microtowers with different morphologies: (d) cylindrical shape with tapered tip, (e) flat top, and (f) cone shape.

rectangular plates, catalyst induced 1D MoO_3 structures were also found on the bare substrate (Fig. 48b-i). This result clearly confirmed that the catalyst can be evaporated and transferred from the NaOH-treated substrate onto the bare one. The catalyst vapors can nucleate and form catalyst particles on the MoO_3 deposition promoting the VSS growth of different 1D structures. It is worth mentioning that catalyst particles were not observed on all the 1D structures. This fact can be explained by following reasons: *a*) Catalyst particles can nucleate at any locations along the 1D structures. Some particles may be invisible hiding on the backside of the 1D structures; *b*) Because of the evaporation, the catalyst particles may become too small to be detected. Some particles could even have disappeared terminating the catalyzed growth, which may explain the growth of the microtowers with a flat top. The evaporation and nucleation of catalyst not only promoted the growth of the 1D structures in

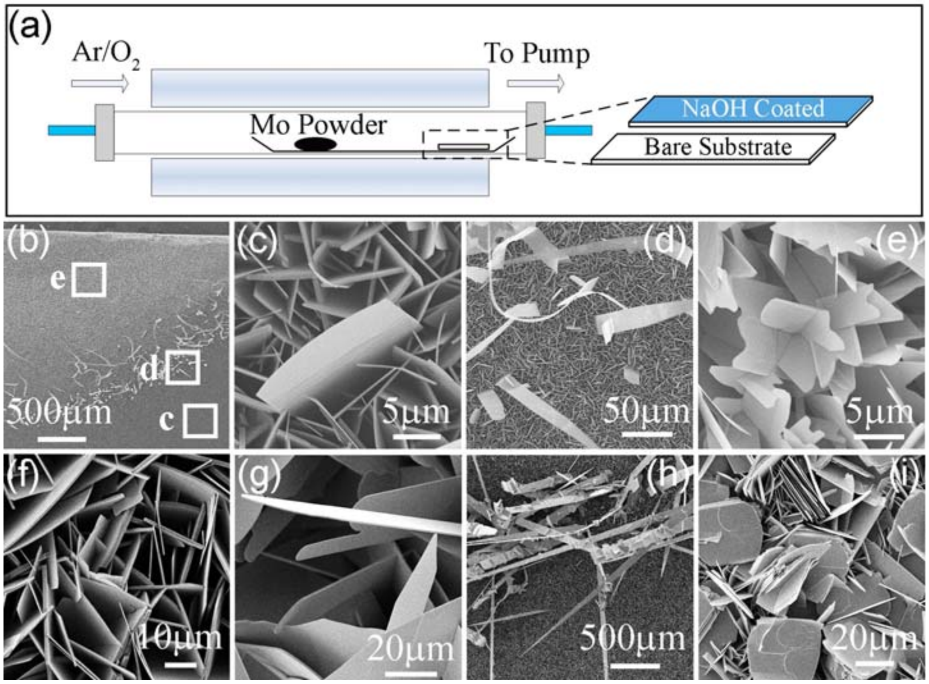

Figure 48: Side-by-side growth of MoO_3. (a) Schematic drawing of the side-by-side growth with one NaOH catalyst treated substrate and one bare substrate. SEM images of the growth on the untreated substrates at different growth times: (b-e) 30 min and (f-i) 120 min. For 30 min growth: (b) low magnification SEM image showing labeled growth areas with different morphologies, (c) rectangular nanoplates grown without catalyst, (d) nanobelts grown with catalyst, and (e) forked nanoplates grown with catalyst. For 120 min growth: (f) rectangular nanoplates without catalyst, (g) forked nanoplates with catalyst, (h) microbelts with catalyst, and (i) microtowers with catalyst.

the second stage growth, they also shaped the morphologies of these 1D structures. Many 1D structures in the second stage were found to have a tapered shape, such as triangular nanobelts (Fig. 39b and d), microtowers with tapered tips (Fig. 39f). Several factors can contribute to the tapering of the 1D structures. First, the reduction in catalyst size may induce the tapering. Owing to the evaporation, the size of the catalyst particles can shrink during the growth resulting in the tapered growth. The VS growth on the side surfaces was another possible mechanism, which promoted the radial growth of the 1D structures forming the tapered shape. Another important factor was the gradually reduced growth during the cooling process. During the cooling, the MoO_3 vapor supply reduced, and the growth temperature gradually decreased. Hence, the growth rate slowed down producing the tapered tips on the top of some 1D structures.

4.3.4 Growth with Other Alkali Metal Catalysts

In analogy to the Na_2MoO_4-MoO_3 binary phase diagram, other alkali metals, such as Li and K, could also form A-Mo-O alloy at elevated temperature. This has potential for using a variety of alkali metal based material as catalysta to promote VLS or VSS growth of MoO_3. Two groups of experiments have been performed in this study; the first one used KI and Na_2CO_3 treated Si substrate and the second one used alkali metal ions containing substrate, including ITO/glass, glass, and mica. Fig. 49a-b show the long belt growth on KI treated Si substrate and the forked plate growth on Na_2CO_3 treated Si, respectively. Compared to NaOH-Si growth, the belt on KI appeared with rough edge; whereas no long belt or tower was observed on the sample with Na_2CO_3.

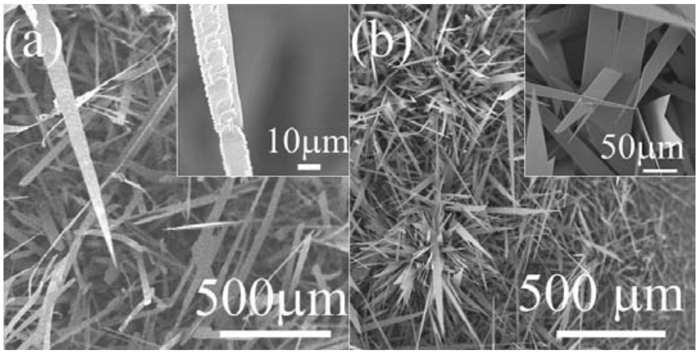

Figure 49: Alternative catalysts for MoO_3 growth. SEM images of MoO_3 1D structures: (a) nanobelts grown with KI on Si and (b) the forked plate growth with Na_2CO_3 on Si.

Fig. 50a-c illustrated microtowers grown on ITO glass, sword-shape belts on glass, and nanobelts growth on mica, respectively. The towers on ITO glass exhibited stacking features. The sword-shape belts on glass arose from a combination of VSS and VS mechanism. The long belts found on mica ($K(Al_2)(Si_3Al)O_{10}(OH)_2$) probably stemmed from potassiumcatalyzed VLS mechanism.[101]

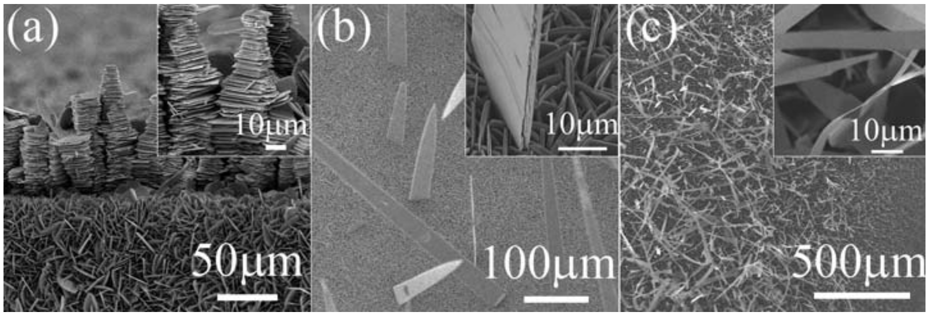

Figure 50: Alternative catalysts for MoO_3 growth. SEM images of MoO3 1D structures: (a) microtowers grown on ITO glass, (b) triangular microbelts grown on glass, and (c) nanobelts and microbelts grown on mica.

A rudimentary analysis on the Na^+ diffusion in glass was performed to understand the growth dynamics of MoO_3 on the alkali ions containing substrates. Because the alkali ions in glass can diffuse out at elevated temperature, the proposed VSS mechanism will modify the MoO_3 deposition. Therefore, the mass transport of sodium ions in silica glass was first estimated to evaluate the amount of catalyst available during the growth of MoO_3. The driving force could be external field or concentration gradient, and the dynamics was governed by diffusion equation

$$\frac{\partial C}{\partial t} = D\frac{\partial^2 C}{\partial x^2}, \tag{14}$$

where C is concentration in unit of mol/cm^3, and D is diffusion coefficient in unit of cm^2/s. Diffusion coefficient highly depends on the overall environment in which the ions reside. Typical values of D for Na ions were listed in Table 17

The substrates used in this work were glass and ITO/glass; the relevant parameters were as following:

- dimension: $25 \times 10 \times 1$ mm

Table 17: Mass transport of sodium ions in silica glass, with diffusion coefficient in unit of cm^2/s.

Composition	Na diffusion coefficient	Reference
Quartz	$3.8 \times 10^{-2} \exp(\frac{-24500}{RT})$	[160]
Sodalite	$6.6 \exp(\frac{-42500}{RT})$	[161]
Obsidian	$4.4 \times 10^{-2} \exp(\frac{-22900}{RT})$	[161]
silicate glass	3.1×10^{-8} at 420°C	[162]
SiO_2 glass	1.1×10^{-7} at 670°C	[163]

R is molar gas constant (8.315 J/mol/K), and T is temperature in K.

- density: 2.567 g/cm^3
- Na concentration: 0.01 mol/cm^3
- D: 1.1×10^{-7} cm^2/s

Substituting these values into Eq. 14, the net flux J was estimated to be

$$J = -D\frac{\Delta C}{\Delta x} = 2.0 \times 10^{-8} \text{mol cm}^{-2}\text{s}^{-1}. \tag{15}$$

In typical growth of 2 h, the net amount of Na diffusing out of substrate was then 1.44×10^{-4} mol, about 10% of total Na ions in the glass substrates. The diffusion length $\sqrt{Dt}$ was 190 μm. Note this result overestimated since the flux will reduce gradually. Meanwhile the molar amount of NaOH applied on Si substrate was about 5×10^{-7} mol. Considering the adjusted ratio, Na contents should be much more when using glass substrate than using NaOH-Si substrate. Another important factor was the evaporation of sodium molybdates; however, only one relevant report by Kazenas et al. could be found in literature.[164] The partial pressure of Na_2MoO_4 was calculated to be 0.2 mTorr at 800 °C and 3.5×10^{-3} mTorr at 670 °C.[12]

---

[12] $\log P(atm) = -13794/T + 6.19$

4.3.5 Optical Properties of Molybdenum Oxide

The optical properties of the as-grown specimen were evaluated using DRS method. Fig. 51a show the hemisphere diffuse reflection spectrum from 800 nm to 250 nm, where the diffuse reflection R_{dff} kept increasing from 27% to 33% when incident wavelength scanned from 800 nm to about 400 nm; then, R_{dff} dropped sharply to 15% between 400 nm and 300 nm. The KMT function fitting was used to estimated the energy gap, as displayed in Fig. 51b. Extrapolation indicated a gap of 3.2 eV, corresponding to absorption edge at 387 nm. This matched well with the DRS data. Another reflection peak was found at 260 nm, illustrating there is more complex electronic band structures for MoO_3 above 4 eV. As a comparison, the estimated energy gap and results from previous studies is summarized in Table 18.

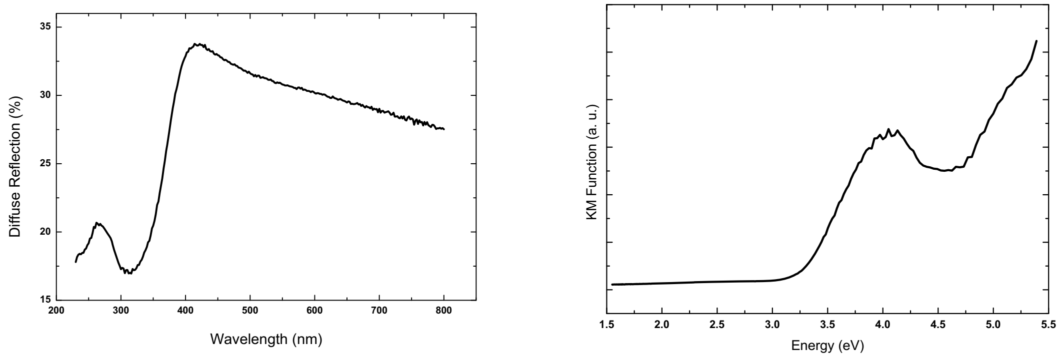

(a) (b)

Figure 51: DRS spectrum of MoO_3 nanostructures: (a) diffuse reflection spectrum, and (b) the associated KMT function.

4.4 Summary

In this chapter, a new growth model of MoO_3 using alkali metal ions as catalysts was discovered and investigated in depth. The growth kinetics were closely inspected using a series of controlled experiments. A modified vapor-solid-solid mechanism was proposed

Table 18: Optical band gaps of MoO_3

Reference	Band gap value(eV)	Band gap orientation	material states
[88]	2.96	$E \parallel c_0$	single crystal
[88]	2.80	$E \perp c_0$	single crystal
[165]	2.8~3.2	NA	films
this work	3.2	NA	nanoflakes

and favorably verified. Two growth modes, i.e., transverse growth and axial growth, were highlighted, which not only improved the yield but also allowed for versatile morphology control of 1D MoO_3 nanostructures. This methodology was further extended onto glass and ITO glass substrates, paving the way to a more integrated process of using MoO_3 nanostructures onto various solar energy saving and harvesting applications.

CHAPTER 5: TUNGSTEN OXIDE-TUNGSTEN DISULFIDE NANOWIRES

In this chapter, a TEM-Raman integrated study on WO_3-WS_2 core-shell nanostructures is presented. This study leverages a home-built micromanipulator apparatus to transfer the nanostructures from growth substrates to TEM grids. This transferring technique has allowed for correlating TEM and micro-Raman measurement on individual WO_3-WS_2 core-shell nanowires and enhancing the understanding of structure-property relations, which would otherwise be blurred in conventional ensemble averaged methods. WO_3-WS_2 heterostructure was chosen due to its potential applications in photocatalysis and hydrogen evolution reaction.[10, 166]

The remaining sections are arranged in the following order: a review on the growth of MS_2 (M = Mo, W) nanotubes (NTs) and 2D few-layer (FL) structures will be introduced first, followed by Raman spectroscopy summary on WS_2 NTs and FL. The thesis will then focus on synthesis of WO_3-WS_2 heterostructure and various characterizations on both ensemble and individual nanowires. This chapter is concluded with a brief summary and future work.

5.1 Introduction

5.1.1 Properties and Applications of Tungsten Disulfide

Tungsten disulfide (WS_2) is a group VI dichalcogenide semiconductor compound. The molecular weight is 249.97 g/mol. Almost all natural WS_2 belongs to P63/mmc space group (2H-WS_2), where a is 3.153 Å and c is 12.323 Å (PDF 04-003-4478). Two other crystal structures were found in man-made WS_2, i.e. 1T and 3R, where 3R can be prepared by bromine (Br) chemical vapor transport (CVT) method [167] and 1T was generally found in alkaline intercalated WS_2.[168, 169] As a reference, the lattice dimensions of MoS_2 and WS_2 are summarized in Table 19. WS_2 can also form tubular nanostructures in a similar way as do carbon nanotubes. The geometrical symmetry group of WS_2 NTs has been reported.[173] The basis/lattice vectors a_1 and a_2 are defined in transition metal plane with equal length $a_0 \approx 3$ Å. This monolayered sheet can be rolled up to form a tubular structure when the chiral/translation vector $c = n_1 a_1 + n_2 a_2$ becomes the circumference of the tube. The diameter of a nanotube is given by

Table 19: Lattices dimension of MS_2

		2H-MoS_2[170, 171]	2H-WS_2[167, 172]
Lattice constant	a(Å)	3.1604	3.171
	c(Å)	12.295	12.359
Within MS_2 layer	M-3S (Å)	2.37	2.405
	S-1S (Å)	3.11	3.14
Between MS_2 layer	S-3S (Å)	NA	3.53

$$d = \frac{|\, c \,|}{\pi} = \frac{a_0}{\pi}\sqrt{n_1^2 + n_1 n_2 + n_2^2} \tag{16}$$

Note that $a_1 \cdot a_2 = a_1 a_2 \cos \pi/3$, where $\cos \pi/3 \times 2 = 1$. In analogy with carbon nanotube, chiral angle θ is

$$\theta = \tan^{-1} \frac{\sqrt{3} n_2}{2n_1 + n_2} \tag{17}$$

Chiral angles from the interval $[0, \pi/6]$ is sufficient for all possible tube structures. Tubes $(n, 0)$ with zero chiral angle are named as zigzag; tubes (n, n) with $\pi/6$ chiral angle are armchair; consequently, all others are referred as chiral ones with $\theta \in (0, \pi/6)$. Fig. 52 illustrated basis vectors in the atomic plane of unfolded WS_2 and several nanotube indices.

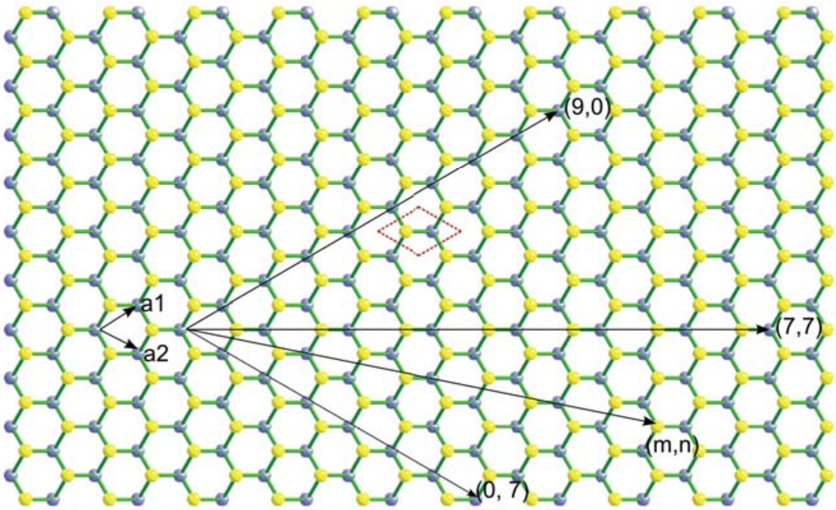

Figure 52: WS_2 nanotube rolling

5.1.2 Review of Synthesis Methods of Tungsten Disulfide

Shortly after the discovery of carbon nanotube (CNT) in 1991,[174] its transition metal dichalcogenides (TMDC) counterparts, i.e. WS_2, was synthesized in 1992.[175] In the following decades, other TMDC and several metal oxides nanotubes were demonstrated as well. Rao and Nath did an excellent work to review these inorganic nanotubes.[176] Hence, this study recapitulated the main categories of synthesis methods:

1. Reducing MO_3 in H_2 and H_2S atmosphere;[13]
2. Direct decomposition of MS_3;
3. Decomposition of the ammonium salt $(NH_4)_2MS_4$;
4. Using CNT as templates, arc discharge, or laser ablation.

Except the aforementioned methods, another important reaction in CVD domain was

---

[13] M = Mo, W in this work

$$WCl_6 + S \rightarrow WS_2 + Cl_2S_2 \tag{18}$$

$$MoCl_5 + S \rightarrow MoS_2 + S_2Cl_2 \tag{19}$$

$$S_2Cl_2 + NaOH \rightarrow NaCl + S + Na_2SO_3 + H_2O \tag{20}$$

This reaction has been explored by several authors[177] and could be used under atmospheric pressure.[178]

All these methods can be applied to the growth of TMDC few layer structures, directly or with some modifications. Among all the members of TMDC nanotubes, WS_2 and MoS_2 NTs were probably the most well investigated.[179–184] The reaction mechanism of WO_3 with H_2/H_2S was thoroughly studied,[185] and a high yield synthesis approach has been established.[186] For WO_3 nanoparticles precursor, it was found that the simultaneous reduction and sulfurization was essential for encapsulation of fullerene like WS_2 structures from the oxide nanoparticles. During the sulfurization process, remaining oxide core was gradually reduced and transformed into an ordered superlattice of {001} CS planes. Further reaction consumed the WO_x core, leading to multi-walled WS_2 NTs. For precursor of WO_3 nanowires, Feldman et al. proposed that TMDC nanotubes growth began with the reduced WO_3 phases, in particular $W_{18}O_{49}$.[187] It is worth noting that MS_2 can be prepared by direct sulfurization from its oxides phase, but reaction $MO_3 + Se \rightarrow MSe_2$ will not proceed unless other reducing agents, e.g. H_2, are used simultaneously.[188] This fact highlights that sulfur is chemically radical at elevated temperature.

Zhu et al. performed a detailed morphological and structural analysis on WS_2 NTs synthesized using WO_{3-x} NWs and H_2S.[189] Sulfur vacancy was found on the outer wall of NT. The tips exhibited various structures. Open-ended WS_2 was observed more frequently than did in carbon nanotubes (CNTs), which was often sealed. Zhu et al. suggested this open-ended tubes resulted from continuous growth on other nanotubes. And the closure configuration was rather complicated; flat caps often dominated. Zhu et al. maintained that this oxide-to-sulfides mechanism might apply to closed caps only, not to those open ended tubes.[189] TEM diffraction analysis could distinguish the chirality of NTs, as demonstrated on CNT[190] and MoS_2.[191] WS_2 NT chirality revealed by TEM SAED show armchair NTs often dominated. Sloan et al. investigated tungsten oxides structures incorporated in WS_2.[50] The encapsulated WO_x cores often exhibited W_3O_8 and W_5O_{14} phases, a feature of the W_nO_{3n-1} homogenous series, arising as a result of CS planes.[192] Some WO_x cores show oxygen vacancy instead of CS planes, leading to prominent streaking in SAED patterns. Although high yield growth method of WS_2 has been available, the extent to which one can control the NT configuration was still limited: single-walled WS_2 NT has not been routinely synthesized, and the electronic properties can only be predicted theoretically. Seifert et al. investigated the electronic structures of WS_2 nanotube using DFT calculation.[193] It was found that zigzag (n,0) NTs exhibted a direct gap at Γ point, whose size increased monotonically with tube diameter; whereas armchair (n,n) NTs, unlike its metallic counterpart of (n,n) CNT, show indirect band gap increasing with tube diameter. Zibouche et al. reached the same conclusion on WS_2 SWNT.[194] It was also found band gaps of armchair and zigzag NTs increased with diameter, going from values close to bulk and approaching that of monolayer; and for a given tube diameter, E_g of zigzag NTs were larger than those of armchair NTs.

Parallel with the scenario of CNT and graphene, TMDC few layer structures have attracted intensive research efforts recently. These atomic TMDC layers exhibits many appealing features, i.e., indirect-to-direct band gap transition,[195] and became a promising candidate in energy harvesting, optoelectronics, and photocatalytic applications. For scientific research purpose, exfoliation by liquid[196] or mechanical methods[197] can provide sufficient materials, yet CVD synthesis of thickness controllable 2D TMDC is stills highly desired, which holds the greatest potential for high yield production of MS_2. So this work focused on reviewing the CVD based methods. This study will review literatures to date on both WS_2 films and few layer structures and highlight several typical investigations using different synthesis methods, as summarized in Table 21. It is important to note that the synthesis of NTs is relevantly independent of substrates, which is in sharp contrast to the scenario of few layer growth. The WS_2 nucleation and interaction with substrates play dominant roles in the growth of 2D FL structures. Hence, it is reasonable to focus on the WS_2 films growth, which presumably could provide valuable insight into the nucleation process on various substrates.

Lee et al. studied the CVD of MoS_2 by $MoCl_5$ or MoF_6 and H_2S in great details. Phase diagrams for Mo−S−Cl−H and Mo−S−F−H system at 1 kPa were simulated.[198] Endler et al. also investigated the solid-phase diagram for Mo−S−Cl−H−Ar system.[199] It was found pure MoS_2 was main product when molar ratio of H_2S-$MoCl_5$ exceeded 2. More important, MoS_2 basal plane orientation can be parallel to substrate when the thickness was smaller than 50 nm. Ennaoui et al. grew tungsten disulfide film using sulfurization of WO_3 under N_2/H_2 gas flow.[200] The composition was found to be $WS_{2.13}$, and the excess of sulfur led to p-type conductivity. XRD peaks ratio was used as a measure of film orientation. Ni_3S_2 phase was found, and surfactant-mediated epitaxy was proposed. Regula et al. studied the Ni-W-S phase diagram and the role of Ni layer in promoting WS_2 film growth from amorphous WS_3.[201] *In-situ* TEM analysis confirmed the formation of NiS_x droplets and lateral growth of WS_2 from these droplets.[202] Recently, it has been shown that direct sulfurization of W coating (20 nm) at 750 °C on SiO_2-Si can also produce WS_2 film.[203] However, the film was of bulk in nature. Previous study of WS_2 growth on various substrates by Genut et al. was summarized in Table 20.[204] It was found that the WS_2 nucleated from an amorphous WS_3 phase and the substrate had a critical role in determining both the reaction onset temperature and the texture. The adhesion of tungsten to quartz was found to be much stronger than to glass. And oxygen-containing species, such as H_2O or OH, tended to cause WS_2 basal plane perpendicular to substrate.

Table 20: WS_2 growth on different substrates

precursor	substrate	conditions	film feature[a]
sputtered W + H_2S	glass	onset 400 °C	$\perp$ *c* at 500 °C, metastable WS_3 found
	quartz	onset 650 °C	$\|\|$ *c* below 950 °C
	Mo	onset NA	$\|\|$ *c* at 1000 °C
	W	onset NA	random orientation
WO_x + H_2S	quartz	onset 500 °C	predominantly $\perp$ *c* after 800 °C
	Mo	onset NA	$\|\|$ *c* dominant
	W	onset NA	random orientation

[a] $\perp$ *c*: the c axis is perpendicular to the substrate, $\|\|$ *c*: the c axis is parallel to the substrate;

For MoS_2, the reaction mechanism of MoO_3 to MoS_2 was studied by Weber et al.[205] This study presumably provided guidelines for the recent syntheses of MoS_2 by sulfurization of MoO_3.[108, 206–208] Similar studies on sulfurization of $WO_3 \cdot H_2O$ to WS_2 and decomposition of $(NH_4)_2WO_2S_2$ were also reported.[209, 210] In combination with the knowledge from WS_2, this thesis compared those insight from several recent reports on WS_2 FL. Cong et al. prepared monolayer WS_2 on 300 nm SiO_2-Si by sulfurization of WO_3 powders in a one-end sealed tube.[211] It was suggested that pre-cleaning the inner tube by isopropyl alcohol (IPA) and DI water could effectively increase the pressure of vapor source. This observation probably arose from the reduction of WO_3 assisted by IPA and water residuals, or due to the possible presence of H_2S. Intermediate phase WO_yS_{2-y} and WS_{2+x} was proposed in the growth mechanism. The apex of triangles could be active site of nucleation, and WS_{2+x} formation was confirmed by secondary ion mass spectrometry. Possible thick WS_{2+x} flakes decomposed subsequently, leading to monolayer (ML) WS_2. The substrates were thoroughly cleaned. It was mentioned that separate sulfur heating improved the photoluminescence (PL) uniformity. Sulfurization mechanism study of WO_3 suggested W^{6+} cannot be directly reduce to W^{4+} in WS_2.[209, 210] Tungsten oxysulfides was necessary as an intermediate phase.

Peimyoo et al. prepared WS_2 on SiO_2-Si using WO_3 powder and sulfur at 800 °C, aiming at the light emission studies to clarify several contradictory reports.[212] Uniform PL intensity was found on the triangular WS_2 flakes, in contrast to previous edge enhanced PL[213]. Raman spectra (532 nm) fit included $E^1_{2g}(M)$ mode at 343 cm^{-1}, according to the phonon dispersion calculation [214] and experimental observation.[215–217] However, none of these experimental reports specifically mentioned $E^1_{2g}(M)$ mode. Tentative assignments of multi-phonon bands were summarized in supporting information of Ref.[216]. As to the growth setup, similar tube furnace as in Ref [218] and [208] was used. To gain additional wisdom on MoS_2 growth, this thesis thus summarized the growth strategies in Ref [218] and [208] as following. Zande et al. prepared MoS_2 on 285 nm SiO_2-Si using MoO_3 and S as precursors.[218] In contrast to the seeding method adopted in Refs.[206, 217], Zande et al. stressed the importance of carefully cleaned substrates[14] and minimum exposure of precursor

---

[14] acetone, 2 h in H_2SO_4 and H_2O_2 (3:1) and 5 min oxygen plasma

to air.[15] Dirty substrates or old precursors led to hexagonal, 3-point star or irregular polycrystalline structures. The growth setup was similar to those in Ref.[206]. The substrate and MoO_3 source distance was critical in determining the growth density. The synthesis strategy in Refs.[206, 217] was briefly mentioned as well, where perylene-3,4,9,10-tetracarboxylic acid tetrapotassium salt (PTAS) treated substrate was found to promote the deposition, while KCl treated substrates did not; small carrier gas flow was preferred (1 sccm N_2). It was also noted that the MoS_2 flakes morphology seemed more uniform in Ref[218] than that in Ref[206]. On the other hand, Najmaei et al. also demonstrated MoS_2 FL growth by sulfurization of MoO_3 nanoribbons,[208] which was applied by dispersion and meant to control the source amount. It was found the diffusion of vapor $MoO_{3\text{-}x}$ was the rate-limiting step in MoS_2 growth. This indicated the amount of source was critical in successful synthesis. The nucleation event was more frequently observed at substrate edges, scratches, or rough surface. Step edges was then intentionally created to facilitate the nucleation. As to the growth dynamics, it was postulated the oxysulfides ($MoOS_2$ Raman spectra found), as intermediate phase, diffused across the bare substrates and formed triangular domains upon further sulfurization. The optimal growth conditions were 800-850 °C, 700 Torr, and sufficient sulfur.

Zhang et al. synthesized WS_2 on sapphire (0001) using WO_3 powder and sulfur as precursor under 900 °C.[219] Ar slightly mixed with H_2 was used to tailor the shape of WS_2 flakes. It was found the source substrate distance played an important role in determining the morphology of the as-grown flakes.[16] The edge termination was not well studied. Raman

---

[15] APCVD, 105 °C for 4 h, 700 °C hold for 5 min, and 10 sccm N_2 within 2 inch tube. rapid cooling from 570 °C

[16] There is a lattice mismatch between Al_2O_3 (4.785 Å) and WS_2 (3.153 Å)

spectra indicated a universal down-shift of A_{1g} peak (1L from 418 cm^{-1} on SiO_2-Si to 416.4 cm^{-1} on sapphire). PL signal of WS_2 on SiO_2-Si was stronger than that on sapphire. The visibility of WS_2 on Al_2O_3 was poor. FET on/off ratio was about 100, indicating low carrier mobility. The other conditions included 880 °C, 90 mm source-to-substrate distance, and 1 inch quartz tube. The growth conditions were probably adopted from Ref.[220].

It is worth noting the flake sizes on sapphire[219] seemed larger than that on SiO_2/Si,[212] either due to the nucleation barrier difference or the amount of growth vapor and growth time. The flake sizes in Ref.[211] was not quite uniform, though it could be even larger than that on sapphire from Ref.[219]. One common feature of aforementioned investigations was growth occurred on bare substrates and no catalyst or seeding promoter was employed. While there is another synthesis approach[217, 221] exclusively focused on using seeding promoter. Lee et al. obtained MoS_2 and WS_2 FL on PTAS-treated substrates ($C_{24}H_{12}K_4O_8$), where tiny (~ 200 nm) seeds were found under AFM. More recently, Ling et al. systemically investigated the role of seeding promoter in facilitating the nucleation of MoS_2 monolayer.[221] It was found various aromatic molecules were effective yet inorganic nanoparticles were not. The mechanism of thin film growth depended on the surface energy, chemical potentials of the deposited layers, and their substrates. Layer growth was preferred when surface adhesive force was stronger than adatoms cohesive force. Seeding promoter probably lowered the surface energy by wetting, thus provided heterogenous nucleation sites. Continuous MoS_2 ML was obtained by evaporating $F_{16}CuPc$ of 2 Å on desired receiving substrates. In each growth, about 10^{-10} mol PTAS was applied onto SiO_2-Si, which was rendered hydrophilic and gentle gas blow to distribute the solution evenly.

Table 21: Summary of TMDC few layer growth methods

TMDC	precursor	growth condition (default temperature unit °C)
MoS_2 films [198, 199]	$MoCl_5$, H_2S	1 kPa, temperature: 400-550 °C, 100/10/2.5 sccm for Ar, H_2S and $MoCl_5$ flow
MoS_2 FL [222]	1-5 nm Mo films on SiO_2, Sulfur	purging, RT-550@30 min, 550-750@90 min and hold for 10 min. Mo coating on Si did not work.
MoS_2 FL [108, 223]	4 nm MoO_3 coating on sapphire	reduced to MoO_2 in H_2 and Ar at 500 °C, sulfurization at 850-1000 °C
MoS_2 FL [207]	$(NH_4)_2MoS_4$ in DMF solution transport by Ar bubbler or dip-coating onto subs	annealing under Ar or Ar + Sulfur, total pressure 0.2-2 Torr,
MoS_2 FL [224]	MoS_2 powder	Ar flow, 900 °C heating, pressure 20 Torr, 650 °C growth
MoS_2 FL [208, 225, 226]	MoO_3 powders or ribbons, Sulfur	Ar flow, 530-850 °C, total pressure 0.2-2 Torr, 5-30 min, mica or SiO_2-Si
MoS_2 FL [206, 221]	18mg MoO_3 powders, Sulfur,various seeding promoter on sub	5sccm Ar, 650 °C, 3 min growth, atmospheric pressure, quick cooling
WS_2 films[8, 227]	sputtering WS_{3+x} on 10 nm Ni	annealing under Ar for 1 h at 850 °C
WS_2 FL [213]	~1nm WO_3 coating on 285 nm SiO_2-Si, 500 mg sulfur	800 °C for 30 min, 100 sccm Ar, atmospheric pressure in [228] and 450 mTorr in [229]. triangular flakes obtained
WS_2 ML [211]	1 mg WO_3 powder on SiO_2-Si covered by another sub, $d \sim 3$ mm, sulfur	750 °C, slow heating, hold for 5 min, one-end sealed inner tube, 100 sccm Ar
WS_2 ML [219]	WO_3 powders, sulfur (separate heating)	900 °C, sapphire subs, 225 mTorr, Ar 80 sccm and H_2 10 sccm, growth time 60 min, adjusting precursor and sapphire distance changing the coverage of WS_2, tube diameter: 1 in. 55 μm triangular flakes
WS_2 ML [212]	1 mg WO_3 powders, sulfur	SiO_2/Si subs. Recipe A: 200 mg S,RT-550, Sulfur begin to melt, 550-800 °C, 5K/min, hold 10mins, 200 sccm Ar. Recipe B: sulfur separated heated at 250 °C. Total pressure: maybe atmospheric, tube diameter: 2 in. 5 μm triangular flakes
WS_2 FL [217]	1g WO_3 powders, sulfur, SiO_2-Si subs treated with PTAS $C_{24}H_{12}K_4O_8$ and gentle gas blow	substrate facing down, APCVD, 800 °C, 5 min, 5 sccm Ar, fast heating.
WS_2 films [203]	20 nm W on SiO_2-Si, sulfur	750 °C, 200 sccm Ar, 1Torr. Annealing at 1000 °C, 25 nm thick WS_2 film obtained

5.1.3 Raman on Tungsten Disulfide: Bulk, Few Layer, and Nanotube

This section will discuss previous studies using Raman to characterize MS_2 films, nanotubes, and FL structures. In each morphology, one or two key points will be highlighted for study in this thesis. The previous Raman efforts on MS_2 film, especially the one using resonant conditions, provided critical insight into the electronic structure and lattice dynamics of these TMDC layered materials. A comparison of Raman between TMDC nanotubes and FL structures was given. For WS_2 NTs, the focus was on the asymmetry of A_{1g} mode and its origin. And for WS_2 FL structures, layer number dependent fingerprint was summarized, and some attempts on analysis the resonant Raman profiles of WS_2 were made. It is worth noting that Raman technique proves to be extreme useful in characterizing CNT and graphene, i.e., tube diameter by assigning the RBMs (radial breathing modes) and G peaks position.[230] And Raman spectroscopy also qualifies as an excellent tool to monitor tensile features of TMDC in both 2D and tubular forms.[231]

Raman spectra arise from the inelastic light scattering of optical phonons. In back scattering geometry, the photon wave-vector stands as $q = 4\pi\frac{n}{\lambda}$. The refractive index $\tilde{n}$ of WS_2 at 532 nm is about $4.726 - 0.737i$,[212, 232] corresponding to a wave-vector about 1×10^8 m^{-1}. Compared to the size of Brillouin zone ($\pi/a = 10^{10}$ m^{-1}), off-resonant Raman could only probe phonon at Γ point, where the phonon momentum ($\hbar k$) is close to zero.

Before discussing the Raman spectra features, this thesis briefly recapitulates some symmetry notations and vibration modes. MoS_2 was used as an example, and those definitions applied to WS_2 as well. Hexagonal MoS_2 belongs to space group D_{6h}^4, and the repeat unit in c axis contains two layers, where sulfur atoms in one layer are directly above the molybdenum atoms in adjacent layers, which is often referred as 2H-MoS_2. Group theory predicts two infrared- and four Raman-active modes for 2H-MoS_2, which are mutually exclusive when the center of inversion is present. First it should be emphasized that in few layer structures, MoS_2 with odd layers belongs to different space group from that of even layers. Bulk MoS_2 and 2L-MoS_2 belong to the space group $P6_3/_{mmc}$ (point group D_{6h}). There are 18 normal vibration modes. The factor group of bulk and 2L-MoS_2 at $\vec{\Gamma}$ is D_{6h}. The atoms site groups are a subgroup of the crystal factor group. The correlation of the Mo site group D_{3h}, S site group C_{3v}, and factor group D_{6h} allows one to derive the following irreducible representations for the 18 normal vibration modes at $\vec{\Gamma}$: $\vec{\Gamma}= A_{1g} + 2A_{2u} + 2B_{2g} + B_{1u} + E_{1g} + 2E_{1u} + 2E_{2g} + E_{2u}$, where A_{2u} and E_{1u} are translational acoustic modes, A_{1g}, E_{1g} and E_{2g} are Raman active, and A_{2u} and E_{1u} are infrared (IR) active. As a contrast, 1L-MoS_2 has D_{3h} symmetry with three atoms per unit cell. The irreducible representation of D_{3h} gives: $\vec{\Gamma}= 2A_2''+A_1'+2E'+E''$, with A_2'' and E' acoustic modes, A_2'' IR active, A_1' and E'' Raman active, and the other E' both Raman and IR active (See Fig. 53). NL-MoS_2 has $9N - 3$ optical modes: $3N - 1$ are vibrations along the c axis, and $3N - 1$ are doubly degenerate in-plane vibrations. For rigid-layer vibrations, there are $N - 1$ layer layer breathing modes (LBMs) along the c axis, and $N - 1$ doubly degenerate shear modes perpendicular to it. When N is even, there are 0 Raman active LBMs and $\frac{N}{2}$ doubly degenerate shear modes. When N is odd, there are $\frac{N-1}{2}$ LBMs and $N - 1$ doubly degenerate shear modes.[233, 234] This discussion can be visualized in Table 22.

The E type phonon branches correspond to in-plane normal modes; and the A type phonons result from out-of-plane vibrations. A_{1g} mode is an out-of-plane vibration involving only the S atoms, while the E_{2g}^1 mode involves in-plane displacement of transition metal and S

Table 22: Lattices vibration of MS_2, reproduced from Ref.[214]

D_{6h}	D_{3h}	Character	Direction	Atoms
A_{1g}	$A_1^{'}$	Raman	(out of plane)	S
E_{2g}^2			(in plane)	M + S
E_{2g}^1	E'		(in plane)	M + S
E_{1g}	E''		(in plane)	S
A_{2u}	A_2''	Infrared	(out of plane)	M + S
E_{1u}			(in plane)	M + S
A_{2u}	A_2''	Acoustic	(out of plane)	M + S
E_{1u}				
B_{2g}^2		Inactive	(out of plane)	M + S
B_{2g}^1			(out of plane)	M + S
B_{1u}			(out of plane)	S
E_{2u}			(in plane)	S

atoms. The E_{2g}^2 mode is a shear mode corresponding to the vibration of two rigid layers against each other and appears at very low frequencies (< 50 cm^{-1} [234]). The E_{1g} mode, which is an in-plane vibration of only the S atoms, is forbidden in the backscattering Raman configuration. In 2H-type TMDC, the A_{1g} mode is more sensitive to electrostatic doping; whereas E_{2g}^1 mode is more sensitive to strain, in which the FWHM of the peaks are indicator of external force quantity.[216]

Lattice vibration of natural MoS_2 crystal was studied by Wieting and Verble using infrared and Raman spectroscopy.[233] It was found the E_{1u} IR mode and one E_{2g} Raman mode were nearly degenerate in energy. Refractive indices from reflectivity measurement were n_0= 3.9 and $n_e = 2.5$. Stacy and Hodul studied MoS_2 and WS_2 Raman spectra using lasing energy close to the absorption edges.[236] Second order scattering from phonon with nonzero momentum was used to explain the rich Raman spectra. Sourisseau et al. investigated the resonant Raman profiles in 2H-WS_2 using ten different excitation wavelengths.[237] Dramatic

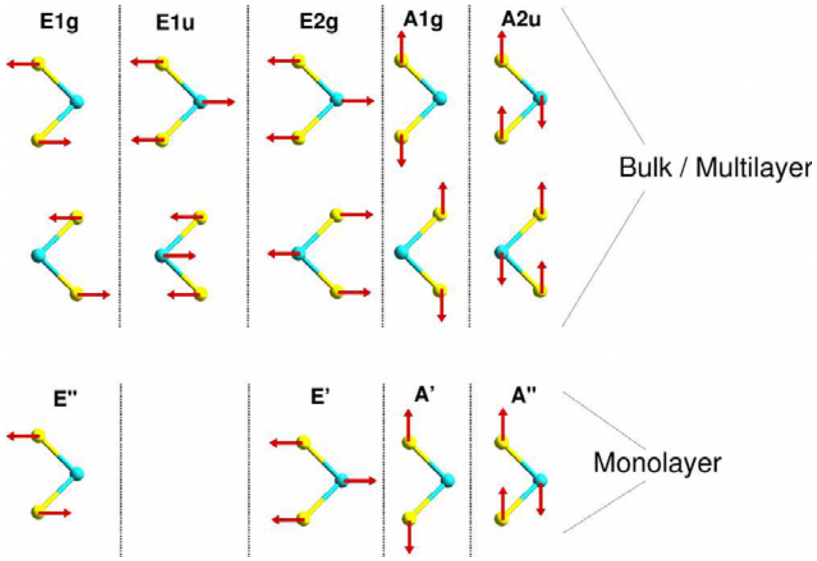

Figure 53: MS_2 vibration symmetry in bulk and monolayer, reproduced from Ref.[235]

intensity variation at 352 cm^{-1} was observed, which was assumed to be of two-phonon signal nature and corresponded to an overtone or combination band of phonons with non-zero momenta contributing to indirect gap absorption edge. Sourisseau et al. assigned this phonon with non-zero momenta as $LA(K_5)$ type (longitudinal acoustic (LA)). The enhancement of the total Raman cross section at excitonic resonance in which excitons served as the intermediate state was stronger compared to that of interband resonance. The strong enhancement at excitonic resonance was attributed to the characteristics of excitons in layered materials such as large binding energy, enhanced oscillator strength, and small damping constant.[216] Chung et al. grew WS_2 film using $W(CO)_6$ and H_2S precursor.[238] Raman spectra ($\lambda = 632$ nm) on films with non-parallel orientation revealed the presence of shoulder mode under A_{1g}, which was assigned to LA and transverse acoustic (TA) phonon coupling. This coupling process stemmed from disorder-activated zone boundary phonons. A further discussion on this non-symmetric feature of A_{1g} mode will be continued in section 5.1.3.

Raman technique has provided much insight into the few layer MS_2. MS_2 layer numbers

Table 23: WS$_2$ Raman symmetry assignment

Symmetry	Raman Shift (cm^{-1})		
	WS$_2$ ML[211]	WS$_2$ NT [239]	WS$_2$ bulk [237]
$E_{2g}^2(\Gamma)$	27.5^a		27.4
$LA(M) - E_{2g}^2(\Gamma)$	148.3		
TBD		153	
$E_{2g}^1(M) - LA(M)$		172	173
LA(M)	174.8	172	
LA(K)	192.4		193
$LA(M) + E_{2g}^2(\Gamma)$	203		
$LA(K) + E_{2g}^2(\Gamma)$	213.9		212
$A_{1g}(M) - LA(M)$	230.9	230	233
$2LA(M) - 3E_{2g}^2(\Gamma)$	264.2	262	267
$2LA(M) - 2E_{2g}^2(\Gamma)$	295.4	294	297
$2LA(M) - E_{2g}^2(\Gamma)$	322.9		325
$E_{2g}^1(M)$	343.1		
2LA(M)	350.8	350	352
$E_{2g}^1(\Gamma)$	355.4	350	356
$2LA(M) + 2E_{2g}^2(M)$		381	381
LA + TA [237] or $B_{1u}(\Gamma)$[240]			416
$A_{1g}(\Gamma)$	417.9	416^b	421
3LA(K)	577		
$LA(M) + A_{1g}(M)$	584	581	585
4LA(M)	704		703

^{a} Calculated from column values; ^{b} Frey et al. probably made incorrect assignment of 416 peak.[239]

were readily identified by the Raman shift distance between A_{1g} and E^1_{2g} mode for MoS_2[241] and WS_2.[213] Yet due to the relative small shift of A_{1g} mode and little shift of E^1_{2g} mode in WS_2 FL, the frequencies distance might not qualify as an unambiguous way to distinguish layer numbers. The resonant Raman profile on WS_2 exhibited unique features between the intensity of 2LA and A_{1g} mode,[213, 216] which provided another routine to assure the monolayer presence. However, this thesis notices some discrepancy in de-convolution of WS_2 resonant profile between 300 and 400 cm^{-1}, i.e., the presence of $E^1_{2g}(M)$ mode at about 344 cm^{-1}.[211–213] Rigid assignments of this mode still requires further theoretical[171] and experimental efforts. In addition, M and Late reported temperature dependent of 1L WS_2.[242] When the temperature increase from 77 K to 623 K, A_{1g} shift from 420 to 416.5 cm^{-1}. Interestingly, 2LA/A_{1g} ratio (514 nm excitation) seemed less than unit in this report. The spectra were obtained from mechanically exfoliated WS_2 lying on 300 nm SiO_2-Si substrate. Moreover, The A_{1g} and E^1_{2g} intensities ratio exhibited reverse behaviors under 532 and 632 nm excitation. This was caused by the different cross-section enhancement for a specific excitation condition. The A and B excitonic absorption in WS_2 mainly arose from the d_{xy} and $d_{x^2-y^2}$ states to d_{z^2} states of tungsten atoms. Thus, electrons excited by 633 nm laser had a character of tungsten d_{z^2} orbitals aligned along the c axis perpendicular to WS_2 basal plane. Since A_{1g} mode involves out of plane displacement along c axis, A_{1g} phonons could couple more strongly with d_{z^2} states than that of E^1_{2g} phonons. As a result, A_{1g} mode was stronger than E^1_{2g} mode at 633 nm resonance.[216] However, the reverse effect for 532 nm excitation could not be well explained using the above argument. This may be caused by electron-phonon coupling with other inter-band transition electrons.

Dobardžić et al. calculated MoS_2 single-walled nanotube (SWNT) phonon dispersion. The dependence of wavenumbers and their displacement on chirality and diameter were discussed. The calculation method enabled studying lattice dynamics with NT diameter up to 50 nm. The chiral vector (n_1, n_2) is defined within the molybdenum plane. Symmetry assignment is zigzag when $(n, 0)$, armchair when (n, n) and chiral when $(n_1, n_2), n_1 > n_2$. Dobardžić et al. theoretically presented Raman scattering of any polarization on SWNT of WS_2 and their dependence on diameter (1-20 nm) and chiral angle. The author assigned 351 cm^{-1} as E_u for WS_2 NT.[244] Ghorbani-Asl et al. discussed the electronic and vibrational properties for large diameter WS_2 NTs.[235] Single-walled NT was approximated by 1H monolayer and others by 2H bulk structure. It was found that large-diameter nanotubes can be approximated with layered systems as their properties should be nearly the same at the scale. Only hypothetical SWNTs and possibly MWNTs with alternating layer compositions, may show direct band gaps. Slight mechanical deformation of the SWNTs would result in a change of the direct band gap back to the indirect one, located between Γ and K high-symmetry points, similarly to the monolayers. As for 2D materials, quantum confinement to single-walled tubes would result in direct band-gap semiconductors with Δ occurring at the K point. Single-walled tubes exhibited slightly softer out-of-plane A' and stronger in-plane E' modes. Those results indicated that the weak interlayer interactions in MS_2 materials cannot be associated with the van der Waals interactions only, but most probably with Coulomb electrostatic interactions as well.

Raman signatures of WS_2 nanotubes show distinct features to the spectra of their bulk counterpart. Frey et al. observed a new line at 152 cm^{-1} in WS_2 NT, which was absent in 2H-WS_2.[239] Another feature was an emerging shoulder on the low energy side of A_{1g} mode at about 416 cm^{-1}. This has been attributed to a combination mode of LA +

TA phonons from the K point of Brillouin zone.[237] The shoulder mode associated with A_{1g} was attributed to LA + TA. As pressure increased from 0 GPa to 18 GPa, these two bands, both shifting to higher wavenumbers, first separated and then recombined. It was assumed the compression mainly occurs in c axis, so the stiffening of A_{1g} was anticipated. A more prominent feature was the resonance profile broadening the shape of E_{2g}^{1} mode, which was often assigned to 2LA mode. Yet there is different opinion on these assignments. Molina-Sánchez and Wirtz labeled the 350 cm^{-1} band as $\mathrm{E}_{1\mathrm{u}}$ instead of 2LA.[214] And recent theoretical investigations suggested 416 cm^{-1} peak is inactive B_{1u} mode,[171, 214] which is the Davydov doublet with A_{1g} mode. Staiger et al. adopted these assignments in studying the resonance Raman profile of WS_2 NTs.[240] It was found that *a*) B_{1u} mode arose from curvature and structural disorder; *b*) B_{1u}/A_{1g} intensity ratio strongly depended on excitation and exceeded unity when excitation energy less than 1.9 eV; and *c*) An excitonic transition energy of NT was found at a local minimum of about 50 nm (layer number probably >10) and increased either way, yet all energies stayed below the bulk value.

Krause et al. also measured the resonant Raman on WS_2 nanotubes and found a split within 420 cm^{-1} region, which was labeled as $D - A_{1g}$ mode in analogy with the similar defect mode of graphene.[245] This $D - A_{1g}$ mode was found enhanced as diameter of WS_2 NTs decreased. This thesis work will use $B_{1u}(\Gamma)$ mode to interpret this emerging line at about 416 cm^{-1} of WS_2 NTs and adopt the 350 cm^{-1} as 2LA(M). Krause et al. confirmed B_{1u} mode arose from the inherent structure of WS_2 nanomaterials instead of surface layer effect. It is also worth noting that A_{1g} appeared stronger than 2LA under 632 nm yet weaker under 532 nm excitation, similar to previous discussion of FL scenarios.[246] Similar observation of Raman spectra on the WS_2-WO_3 structures was found in this study, as discussed in

Sec. 5.3.2. Rafailov et al. estimated the orientation dependence of resonant Raman on one MWNT WS_2 attached to the cantilever tip of AFM.[247] Antenna effect led to optical transition occurring only for polarization parallel to nanotube axis; therefore, resonance Raman intensity of SWNT varied as nanotube orientation. This dependence may provide a routine to distinguish different chiral NTs. Polarized Raman spectra (632 nm excitation) was obtained showing A_{1g} and E_{2g} sharing the same polarization behavior. Viršek et al. investigated the Raman scattering (λ = 632 nm) of WS_2 NTs.[248] The silicon peak at 520 cm^{-1} was used for calibration. Up-shift of A_{1g} and E_{2g} modes (i.e., 420 to 423 cm^{-1} at A_{1g} mode) were observed, which was attributed to the strain in 3R stacking layers.

5.2 Experimental

The WO_3-WS_2 core-shell nanowires were fabricated using a sulfurization process based on the WO_3 NWs prepared from the seeded growth method in Chapter 3, Sec. 3.3.2. For the sake of completeness, schematic layout of the two-step growth is illustrated in Fig. 54, including the seeded growth and subsequent sulfurization process. In a representative seeded growth (Fig. 54a), 4N5 or 5N tungsten source powders as defined in Table 6 were positioned

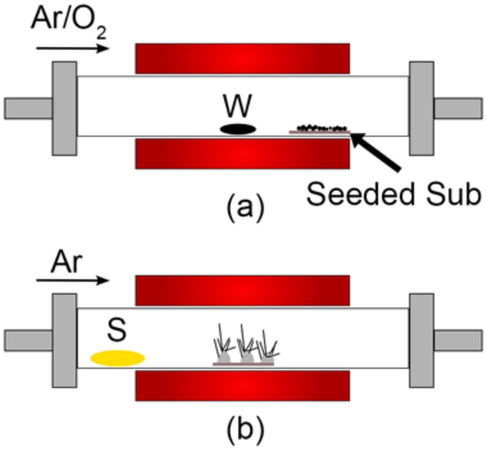

Figure 54: Schematic diagrams of (a) seeded growth of WO_3 NW and (b) sulfurization process.

in the upstream end of a quartz boat, and downstream about 2.5 inch the substrate was stationed. Additional tungsten seed powders (3N) were distributed evenly onto the substrate. After pumping down, 1 sccm oxygen and 10 sccm Ar were admitted into the chamber, respectively. The heating temperature was ramped up to 1000 °C in 30 min and lasted for 240 min. Subsequently the apparatus was allowed to naturally cool down to room temperature.

WO_3-WS_2 core-shell NWs were synthesized using direct sulfurization of WO_3 NWs. As depicted in Fig. 54b, the as-grown WO_3 NWs were loaded into the center of heating furnace, and ~ 200 mg sulfur (Alfa Aesar 10785, 99.5%) was positioned just outside the upstream edge of furnace, where the maximum temperature was about 240 °C. After pumping down, the reaction chamber was flushed two times to expel residual air. A cold trap filled with liquid nitrogen in downstream was used to collect possible sulfur condensation. Then, the furnace was heated to 750 °C in 30 min, held for 15 min, and allowed to naturally cool down to room temperature. During entire growth process, 30 sccm Ar was used as carrier gas.

5.3 Results and Discussion

5.3.1 Ensemble Measurements on Core-Shell Nanowires Array

The morphology of WO_3 NWs in micron scale almost stayed the same after sulfurization, as shown in the inset SEM imaging of Fig. 55. The length of individual nanowire were up to 15 μm, and the diameter varied from about 40 to 200 nm. The surface of the NWs were rather smooth without other attachments. The NWs array grew slightly larger than the W seeds (~12 μm), mostly due to the elongation of NW. The EDX spectrum in Fig. 55 revealed the presence of sulfur element, indicating the effectiveness of sulfurization. Compared to

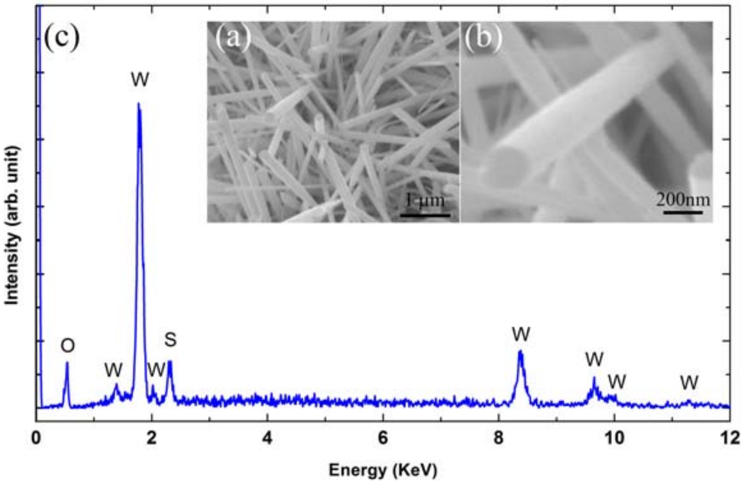

Figure 55: Morphology and composition analysis on the as-synthesized WO_3-WS_2 core-shell structures. (a) Low magnification and (b) high magnification SEM images showing the NWs morphologies after sulfurization. (c) EDX spectroscopy revealing the presence of sulfur element after sulfurization.

the XRD pattern on seeded growth WO_3 sample, post-sulfurization pattern (Fig. 56) show a much reduced WO_3 intensity with W phase becoming relatively prominent. The peaks at 23.44° and 24.36° were indexed to WO_3 (020) and (200) reflection, respectively. This result as well as the SEM imaging indicated WO_3 NWs preserved some long range order after the sulfurization process of 15 min at 750 °C. This observation can also be used to account for the extreme small peak at 13.87° in the post-sulfurization spectrum. In comparison to the reference 2H-WS_2 (002) peak (14.37°, ICDD PDF 04-003-4478), the redshift of specimen peak here indicated an increase of lattice spacing along *c* axis (from 6.16 Å to 6.38 Å). The FWHM of this (002) peak was about 1.1°, giving an estimation on the crystalline size of 7.5 nm according to Scherrer equation.

Owing to this small spacing, TEM was primarily utilized to observe the detailed morphology of WO_3-WS_2 core-shell NWs. Fig. 57c and d show HRTEM imaging on typical tip and body region of the core-shell NW, respectively. A comparison with the pre-sulfurization specimen (Fig. 33 on page 58) readily revealed the formation of core-shell morphology

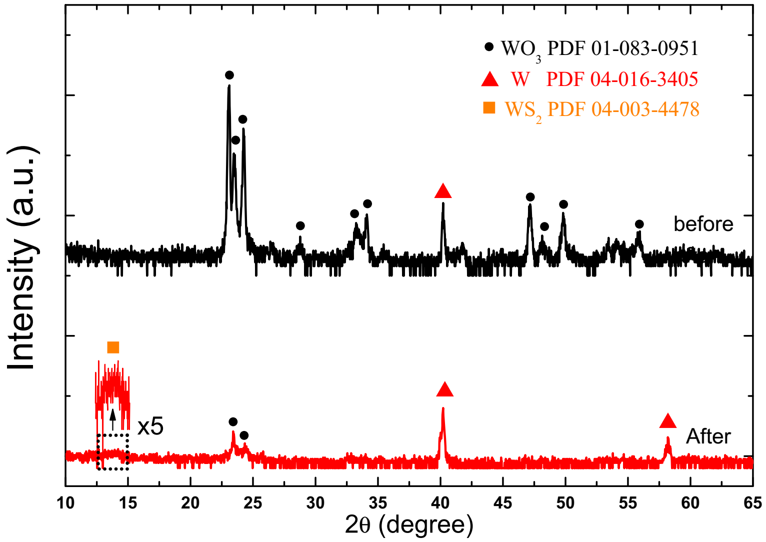

Figure 56: X-ray diffraction spectra before and after sulfurization. The reference spectra for *c*-W, 2H-WS_2 and *m*-WO_3 are included with major peaks labeled.

after sulfurization. The measured wall spacing of 6.5 Å appeared slightly larger than bulk 2H-WS_2 value of 6.16 Å, but matched well with the XRD result in Fig. 56. The sharp contrast in core region also proved the lattice structure of WO_3 was not seriously distorted upon sulfurization.

After examining dozens of core-shell NWs, this study found the WS_2 wall number at NW tip was usually the largest, reaching more than ten, and the wall number decreased to one along the NW body; but there also existed some wall number fluctuation and shape modification. Fig. 58 show a smooth transition of WS_2 wall number on the tip region of one NW. The wall number was about 7 on the tip corner, gradually decreased from 4 to 3 along the NW body, and stopped at 2 walls. Closer observation indicated the wall spacing was not quite uniform in the tip area, probably due to the complex curvature and bending. WS_2 fullerene also show similar structures. Since the closing of the tip region could be of great complexity and the induced strain could modify Raman signal considerably, the TEM-Raman

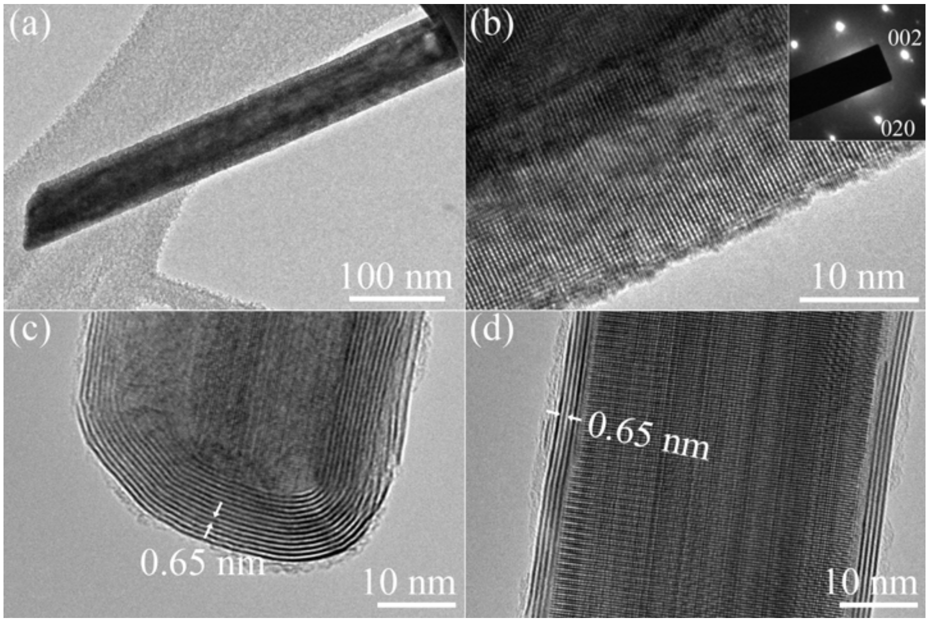

Figure 57: HRTEM imaging before and after sulfurization illustrating the presence of core-shell structure. (a) Low magnification and (b) HRTEM images on WO_3 NW specimen from seeded growth; HRTEM images on the core-shell nanowire of (c) tip region and (d) body region showing wall number variation. The contrast between (b) and (d) readily identify the formation of core-shell structure.

integrated measurement in this study focused on the body region of the core-shell NWs with smooth transition wall number. As illustrated in Fig. 59, complicated WS_2 encapsulation was observed on one tapered core-shell NW. This tapering probably arose from the sulfurization process but could be also due to the parent WO_3 NW. The diameter varied from about 200 nm to 15 nm, and the WS_2 wall number also changed in a nonlinear manner. On some

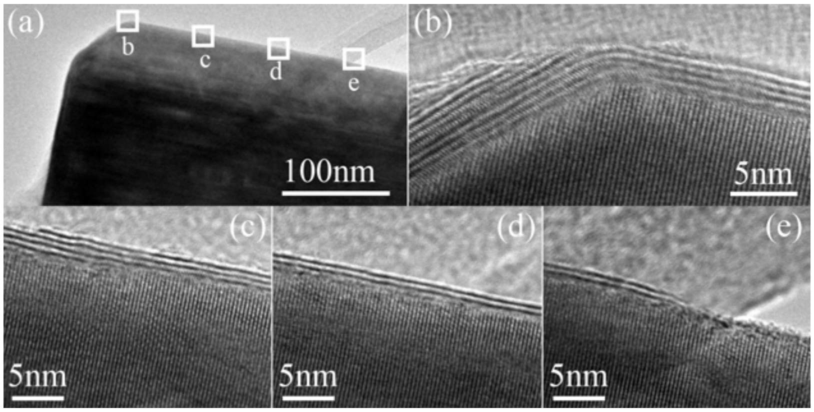

Figure 58: HRTEM imaging on the tip area of one core-shell nanowire.

turning region, the WS_2 seemed penetrating into the body of primary WO_3 NW.

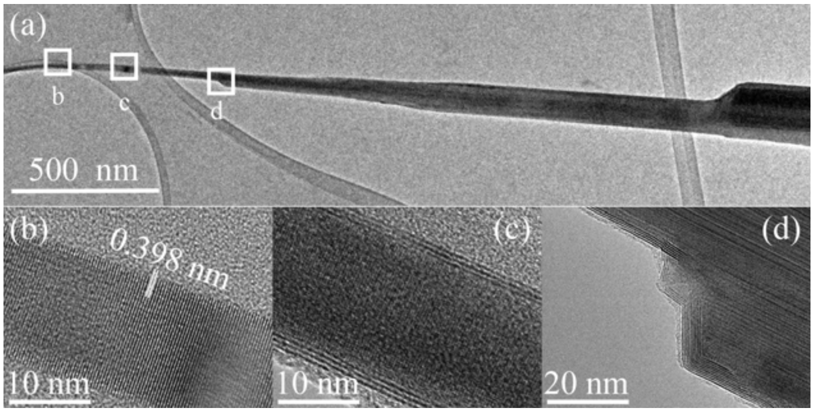

Figure 59: HRTEM imaging on one tapered core-shell nanowire showing fluctuation of wall numbers.

A systematic study on the sulfurization must be performed to understand the growth dynamics. The growth mechanism of WS_2 nanotubes from oxides has been thoroughly studied,[185] and it was generally agreed that the sulfurization of WO_3 was a diffusion limited reaction.[187] It was also suggested that the core WO_3 NWs became non-stoichiometric phases upon sulfurization.[187, 249] This study recognized this possibility but also considered two factors different from previous studies: one was the usage of sulfur as precursor instead of H_2 and/or H_2S as in previous reports, which accelerated the reduction of WO_3 significantly due to the formation of H_2O; the other was the short reaction time and light degree of sulfurization, which probably would not distort the WO_3 lattice significantly, as evidenced by the XRD and HRTEM analysis in this section. The sulfurization dynamic was then proposed as following: The tips of the NWs exposed directly to the sulfur vapors resulting in a high sulfurization rate. On the other hand, sulfurizaiton along the NWs is limited by the diffusion of the sulfur vapors through the dense NWs array. Therefore, the WS_2 wall number is not uniform along the as-grown core-shell NWs.

No obviously consumed core region was observed among most of the core-shell NWs

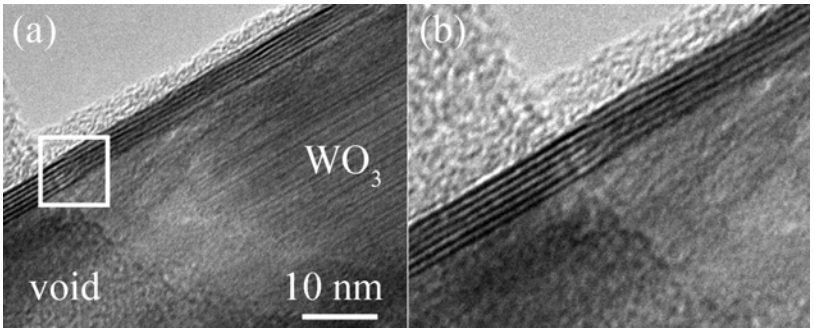

Figure 60: HRTEM imaging on one core-shell nanowire showing consumed core.

examined under TEM. An exception was shown in Fig. 60. Note the rectangular area show abrupt termination of one WS$_2$ wall, indicating a formation of dislocation.

5.3.2 An Integrated TEM-Raman Study on Individual Nanowire

To perform TEM-Raman integrated study, the core-shell specimen was first dispersed into ethanol solution; and then the solution was dipped onto polydimethylsiloxane (PDMS) support. A home-built micromanipulator with probe tip (tungsten, 100nm point radius, Micromaipulator) was used to pick up the core-shell NWs and transfer them onto TEM grids (Lacey C, 300 mesh, Cu, 01895-F Ted Pella, Inc) under 100X objective. The steps were visualized in Fig. 61. The transferred NWs were first examined using TEM to identify the WS$_2$ wall configuration and the associated geometrical orientation. Then, the core-shell NWs on TEM grids were probed under Raman in a location-resolved manner. Only those core-shell NWs exhibiting relative smooth WS$_2$ wall number[17] transition were used in subsequent Raman measurement. To perform TEM and Raman analysis on individual NWs, this study placed one NW only in each cell of the TEM grid (65 × 65 μm). And the low magnification TEM images and optical images were compared to map the NW location and orientation. The carbon film patterns served as a unique background to resolve possible

---

[17] wall number and layer number were used interchangeably in this work, but note that 1 wall is not equal to 1 layer due to the tubular structure

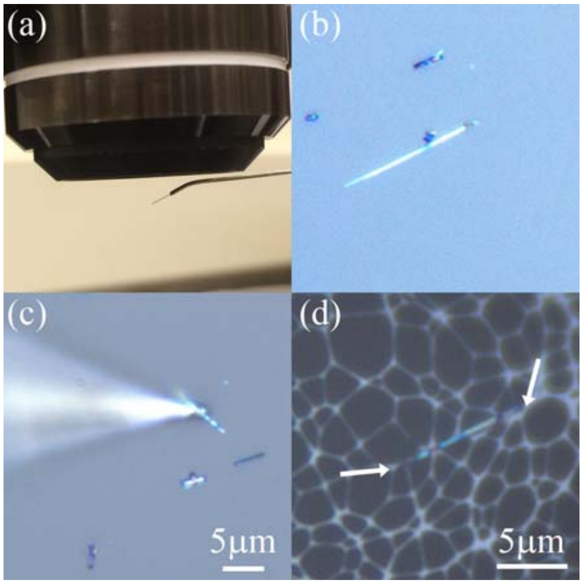

Figure 61: Core-shell nanowires transfer steps. (a) tungsten tip under X100 objective, (b) NWs dispersed onto PDMS, (c) one NW picked up using tungsten tip and (d) tranferred NW on TEM grid with two tips indicated by the arrows.

ambiguity. An example was given in Fig. 62.

Fig. 63a-d depicted typical morphologies of the WO_3-WS_2 NWs in the TEM-Raman integrated study. The diameter of these core-shell NWs was about 100 nm, and the length about 10 μm, allowing for up to five distinctive Raman scattering sites. Fig. 63e show the associated Raman spectra acquired on the core-shell NWs using 532 nm excitation wavelength. Two strong peaks were observed between 300 and 450 cm^{-1}. The resonant nature[236] of Raman shift was recognized by the broad band at about 350 cm^{-1}. Recent theoretical[214] and experimental[240] studies on 2D and tubular WS_2 agreed that this band consisted of first order mode E^1_{2g} and second order mode $2LA(M)$, although there was still discrepancy on the exact symmetry assignment, i.e., the presence of $E^1_{2g}(M)$ mode.[212, 213]. The other peak at about 420 cm^{-1} was assigned to A_{1g} mode in both bulk[250] and few layer WS_2. Tubular WS_2 structure can be viewed as rolling up the planar WS_2 sheet, and new Raman features arose subsequently, e.g., a shoulder mode emerged on the low

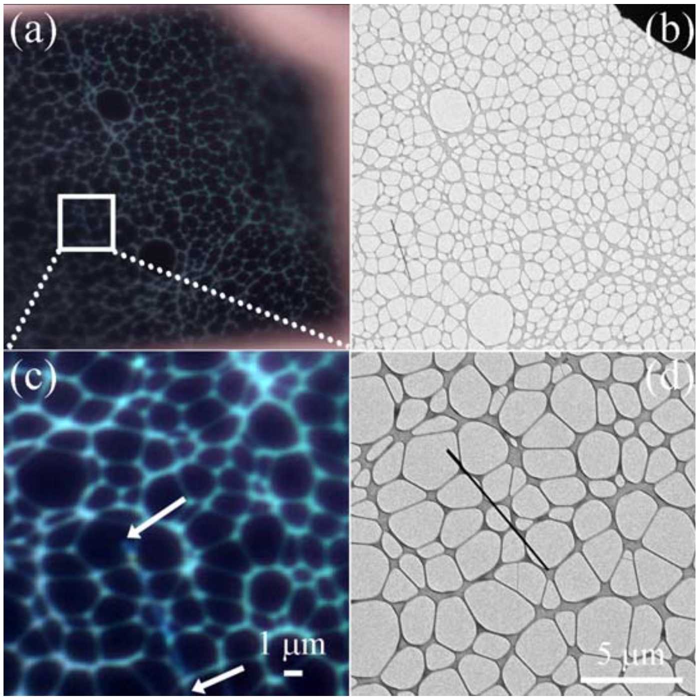

Figure 62: Core-shell nanowires mapping. Optical image of one NW on the lacey carbon TEM grid under (a) x100 magnification and (c) digital zoom-in view with two end indicated by the arrows, TEM images of (b) low magnification and (d) high magnification acquired on the same NW specimen.

frequency side of A_{1g} mode. Theoretical investigation suggested assigning this mode as B_{1u}, the Davydov doublet of A_{1g} mode.[171] And experimental study confirmed this B_{1u} mode arose from structural disorder of WS_2 layers, and the intensity ratio between B_{1u} and A_{1g} strongly depended on excitation wavelength.[240] This study observed B_{1u} mode under 532 nm was much less prominent than that of 632 nm, in consistent with previous reports.[245, 246]

Rigid analysis of the Raman spectra must be performed to reach solid conclusion. Hence, multi-peak Lorentzian fitting was employed on the spectra in Fig. 63e, and the result for one wall WS_2 core-shell NW was displayed in Fig. 64a. The de-convolution peaks compared favorably with original Raman spectrum, and similar operation were used for other three spectra. Fig. 64b show the wall number dependence on three group of intensity ratios

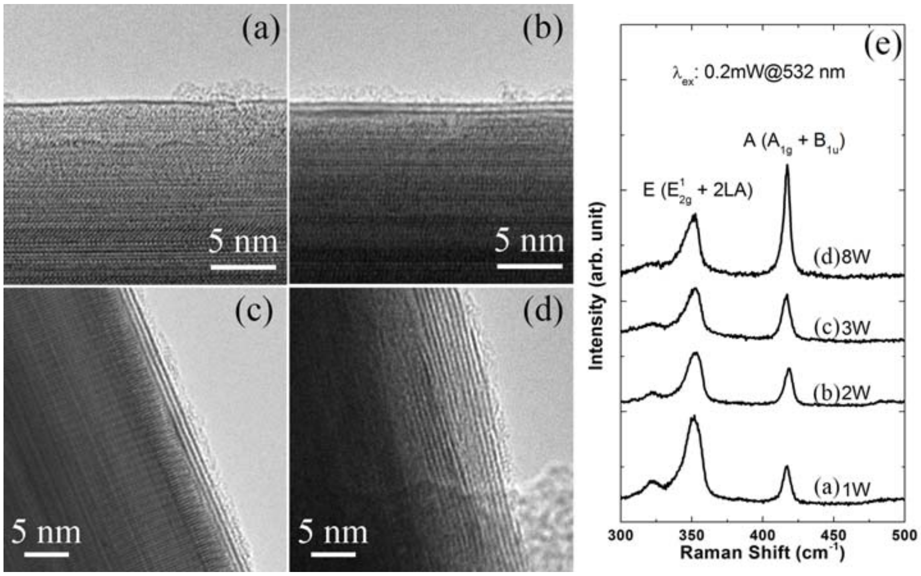

Figure 63: TEM-Raman integrated characterization on core-shell NWs. (a)-(d) HRTEM images on four NWs showing the WS_2 wall number variation from one to about ten. (e) Raman spectra acquired from the same core-shell NWs supported on TEM grids, indicating a sharp contrast between the in-plane and out-of-plane vibrations. Note that the Raman spectra primarily arise from the outer WS_2 shell, and only weak Raman shift at about 800 cm^{-1} were observed at some bare core region (not shown here).

extracted from apparent value, de-convoluted height, and integrated intensity, respectively. Similar trend was found among all three set of data, though the integrated intensity appeared more sensitive towards wall number variation. For a qualitative purpose, the apparent intensity ratio $I_{E/A}$ between in-plane E band ($E^1_{2g} + 2LA$) and out-of-plane A band ($A_{1g} + B_{1u}$) was used as a quick criterion to distinguish WS_2 few wall in this study. $I_{E/A}$ was then extracted to correlate with wall number variation on tens of core-shell NWs. As shown in Fig. 65, the mapping of WS_2 wall dependent $I_{E/A}$ almost followed the same trend in Fig. 64b with some variation attributed to the core-shell NW diameter difference. The intensity ratio $I_{E/A}$ decreased monotonically with the increase of WS_2 wall number, a similar trend as observed on two-dimensional (2D) few layer WS_2,[213] and the exact value of $I_{E/A}$ show modest difference with 2D sheet, which could be attributed to the suspended configuration

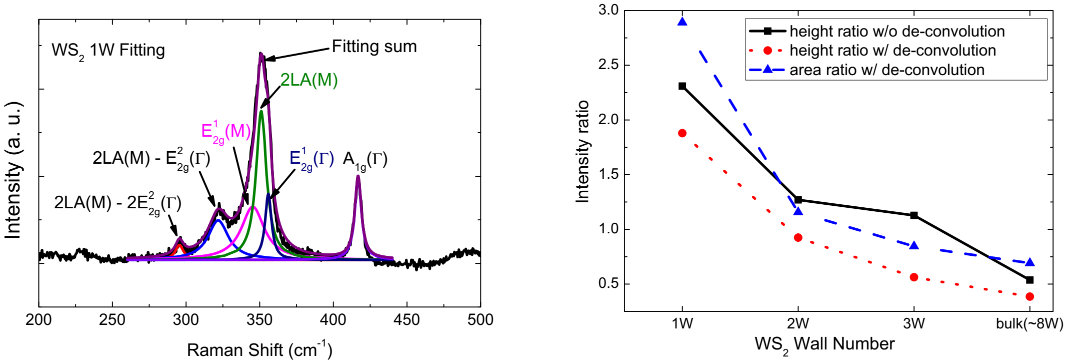

(a) (b)

Figure 64: (a) Multi-peak Lorentzian fitting on core-shell NWs, and (b) wall number dependence on averaged intensity ratio between the in-plane and out-of-plane Raman bands.

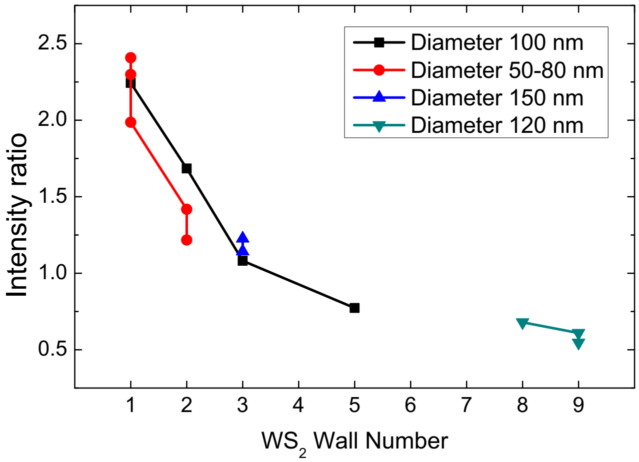

Figure 65: Mapping on the WS_2 wall dependent intensity ratio. The Raman spectra were acquired on individual NW suspended on 300 mesh lacey C TEM grid.

of current core-shell NWs specimen and the presence of WO_3 core. Furthermore, these results indicated that $I_{E/A} > 2$ for single-walled WS_2 core-shell NW, and when the WS_2 wall number was about 3, $I_{E/A} = 1$. These two values served as a quick determination of WS_2 wall number when the NW was suspended.

Before using this observation in more general scenarios, one should evaluate the influence of WO_3 and other dielectric substrates. It has been demonstrated that the optical interference from dielectric environment significantly modified the intensity of Raman scattering from layered MoS_2, regardless lattice vibration modes.[251] In this work, the author calculated the reflectivity of three different stacking scenarios to estimate the influence of WO_3 and insulating substrate, as shown in Fig. 66. It was concluded that under 532 nm excitation, the WO_3 core show little influence on the Raman intensity when WS_2 nanotube was suspended in air; whereas the SiO_2/Si substrates dramatically enhanced the Raman scattering of the core-shell NWs. It was further predicted that current Raman spectra on the core-shell NWs can be used to estimate WS_2 nanotube wall numbers.

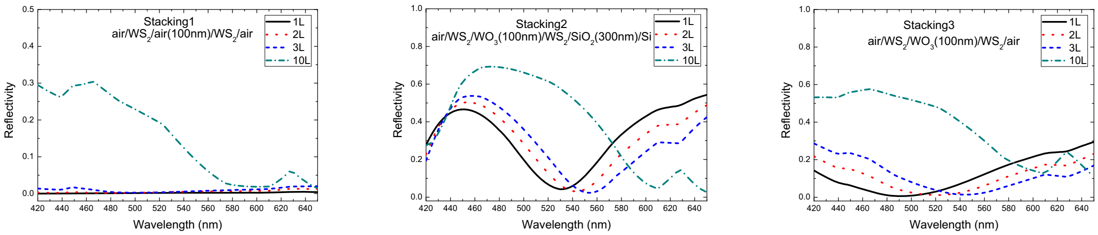

(a) (b) (c)

Figure 66: Optical reflectance simulation on three WS_2 wall stacking configurations.

PL was examined with core-shell NWs on insulating SiO_2-Si substrates. A typical Raman spectrum from 160 to 6000 cm^{-1} was presented in Fig. 67. This pattern was acquired on the middle spot of the core-shell NW shown as inset. Using 532 nm excitation, the multi-phonon resonant feature was clearly resolved. A broad PL peak was also observed with center at 628 nm and FWHM of 23 nm, corresponding to a photon energy of 1.974 eV with width of 72 meV. Another feature was the presence of three peaks centering at 1860, 3695, and 5500 cm^{-1}, respectively, where the latter two were probably the secondary and third overtones of the first peak. It was confirmed that this three peaks belonged to Raman shift instead of PL, since similar peaks were observed using different excitation wavelength of 441 nm and 532 nm. The origin of this peak family was still under research, and one

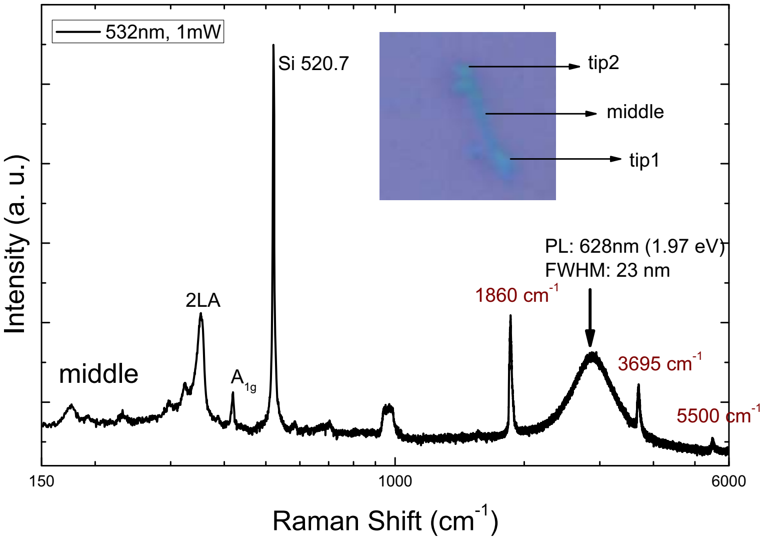

Figure 67: Raman spectrum acquired on the middle spot of core-shell NW (inset) using 532 nm. The x axis is in logarithmic scale.

possible candidate was the C=O bonding, which presumably came from the carbon impurity in tungsten powders as seeds. It was also possible that the C=O bonding arose from the hydrocarbon contamination attached onto the core-shell NWs. Interestingly, the intensity of this three-peak family attenuated significantly when using 441 nm excitation, as shown in Fig. 68. This comparison suggested there might be some enhancement mechanism from WS_2 resonant Raman vibrations.

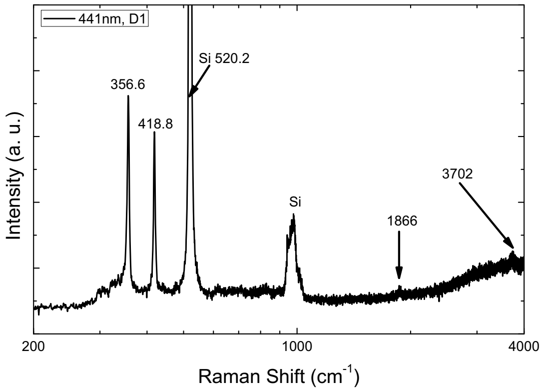

Figure 68: Raman spectrum acquired on the middle spot of core-shell NW shown in the inset of Fig. 67.

Three Raman sites were chosen to probe possible wall variation using both 532 and 441 nm excitation with the naming displayed in the inset of Fig. 67. The Raman patterns were shown in Fig. 69a-b. The off-resonance profile in Fig. 69b show only two modes: E_{2g}^{1} mode at about 357 cm^{-1} and A_{1g} mode at 418 ~ 419 cm^{-1}. In contrast, the on-resonance profile in Fig. 69a exhibited much richer spectra. The shoulder mode at tip2 spectrum was a manifestation of B_{1u} mode from curved WS$_2$ wall. According to previous analysis, the apparent ratio between in-plane and out-of-plane vibration indicated site tip2 had multi-wall WS$_2$, and the other two possibly had few-wall WS$_2$. This predication was confirmed by the associated PL measurement displayed in Fig. 70. Strong luminescent peaks were found at site mid and tip1, and an extremely weak peak were found from site tip2. The PL peaks centered at 1.958 and 1.934 eV for mid and tip1, respectively. The second and third order peaks also show up on all three Raman sites.

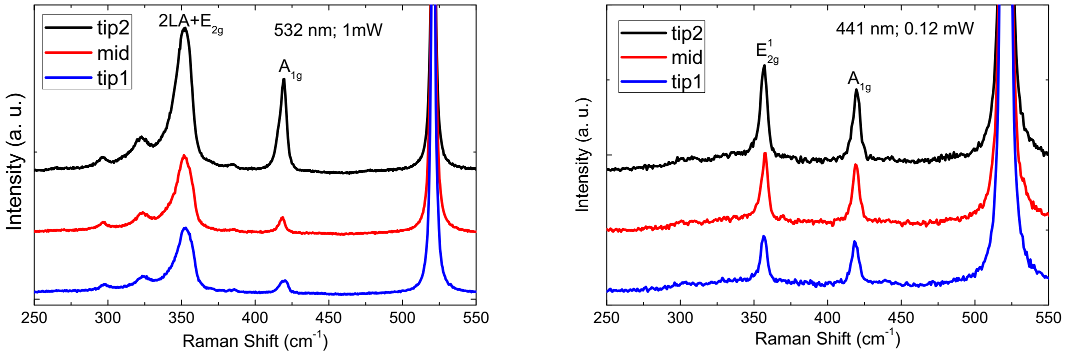

(a) (b)

Figure 69: Raman scattering from (a) 532 nm and (b) 441 nm excitation scanned along the core-shell NW.

5.4 Summary

A comprehensive understanding of the structure-property relation, which is essential to successful application of nanomaterials, is often hindered by the ensemble averaged

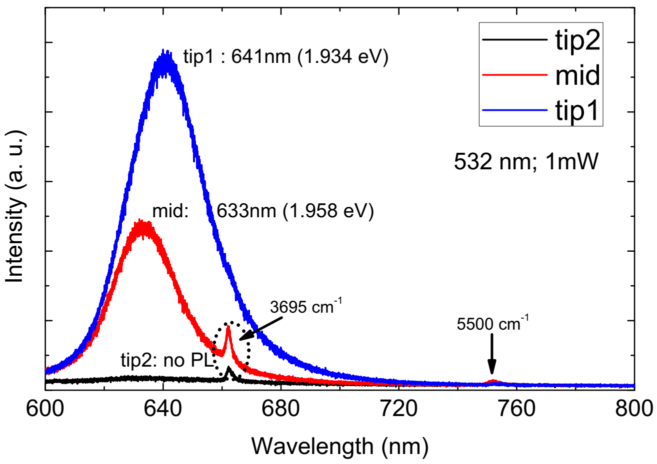

Figure 70: PL spectrum acquired on the core-shell NW shown in the inset of Fig. 67.

characterizations in conventional methods. The present work in this chapter, to some extent, circumvented this limitation by leveraging a home-built micromanipulator apparatus to transfer the nanostructures between TEM grids and other desired substrates. Considerable insight on the WO_3-WS_2 core-shell nanostructures was obtained: few-wall, even single-wall tubular WS_2 nanostructure were observed with WO_3 cores; wall number dependent Raman spectra were studied at on-resonance and off-resonance conditions; the fingerprint of few-wall WS_2 was revealed; and photoluminescence from core-shell NWs was identified. These results held great values to the application of WO_3-WS_2 heterostrucutres in photocatalysis and photoelectrochemical applications. More important, this technique of TEM-Raman integrated study could be readily applied to a variety of other nanomaterials, therefore opening a broad spectrum for the understanding of the structure-property relation, propelling the potential nano-engineering applications.

CHAPTER 6: SUMMARY AND FUTURE WORK

In summary, synthesis of WO_3 and MoO_3 nanostructures based on CVD method were thoroughly investigated in this study. Sodium impurity effect in tungsten powder source was revealed, and the formation of $Na_5W_{14}O_{44}$ nanowire was first reported. Partially enlightened by this discovery, a new VSS growth mechanism of MoO_3 was hypothesized, and the growth dynamics was systematically probed. Comprehensive electron microscopy characterizations were performed on both WO_3 and MoO_3. And the insight of growth kinetics can be used to establish a systematic connection between the interaction of transition metal oxide and alkali metal ions. As an example, preliminary results of WO_3 NWs growth using NaOH treated Si substrate and controlled MoO_3 1D nanostructures growth on glass were presented in Sec. 6.1 and Sec. 6.2, respectively. Seeded growth of WO_3 was demonstrated to be an effective and scalable approach for obtaining single crystalline 1D WO_3 NWs. Based on these WO_3 nanowires, WO_3-WS_2 heterostructure was synthesized using a simple sulfurization process, and single-walled WS_2 tubular core-shell nanowire was observed. More important, a TEM-Raman integrated approach was tested aiming at providing a location-resolved map between crystal structure and optical properties. As a result, wall number dependence of Raman spectra on WS_2 tubular nanostructure was fingerprinted, and direct band gap PL from WS_2 tubular structure was observed. These results indicated a broad space for band structure tuning of WO_3-WS_2. Moreover, the integration of TEM-Raman served as an excellent tool to correlate the structure-property relationship for other 1D nanomaterials.

6.1 Preliminary Results on Catalytic Growth of Tungsten Oxide

The growth conditions almost remained the same as that of the non-seeded WO_3 growth except that the substrate were located at 7.5 inch (refer to page 34 for details). As shown in Fig. 71, dense NWs were observed on NaOH treated substrate by SEM imaging, where the length ranged from 3 to 10 μm and diameter from 50 to 200 nm. Compared with the WO_3 NWs in seeded growth, the deposition here also exhibited some plausible plate morphology.

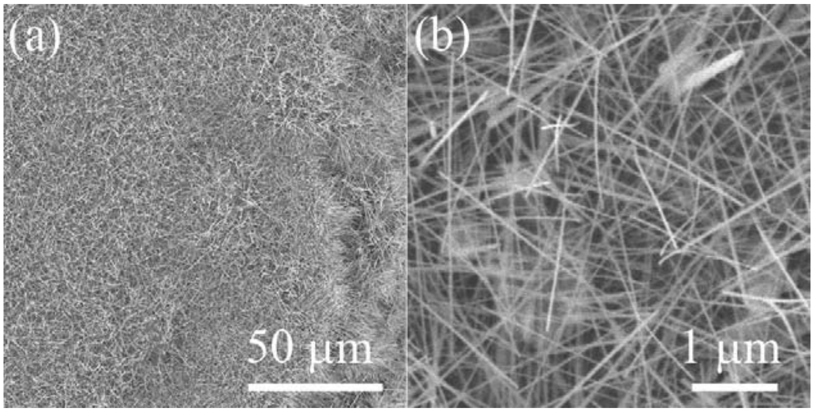

Figure 71: SEM characterization of NaOH catalyzed WO_3 growth. (a) Low-magnification SEM graphs showing dense WO_3 NWs, and (b) a high magnification view showing thin NW growth.

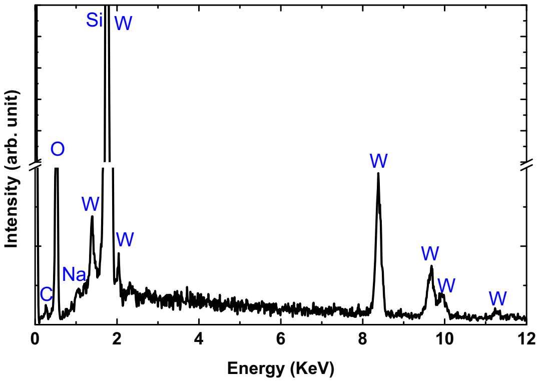

Figure 72: Composition analysis on NaOH catalyzed WO_3 growth NWs identifying small fraction Na content.

EDX analysis on the NaOH WO_3 sample was shown in Fig. 72. Tungsten, oxygen, and sodium elements were detected on the plate growth region with Na/W atomic ratio close to

0.05/1. Fig. 73a displayed the XRD pattern on one representative sample. The phase identification turned out to be ambiguous. One candidate was orthorhombic WO_3 phase (ICDD PDF 00-020-1324, *a*=7.384 Å, *b*=7.512 Å, *c*=3.846 Å); another one was monoclinic $W_{10}O_{29}$ phase (ICDD PDF 04-007-0501, *a*=12.1 Å, *b*=3.78 Å, *c*=23.4 Å, β=90.5°). Micro-Raman scattering spectroscopy was performed on the as-synthesized sample as well. As shown in Fig. 73b, five distinct bands were well resolved with peaks located at 230, 380, 428, 650 and 816 cm^{-1}, respectively. Another small hump was also observed at 946 cm^{-1}. This Raman spectrum deviated from typical features of WO_3,[76, 84] but matched well with $WO_3 \cdot H_2O$ in one previous study;[77] (also see Table. 9 on page. 43) however, the XRD pattern did not reveal tungsten oxide hydrates feature.[18] Further analysis was therefore required to confirm the exact phase of NaOH catalyzed WO_3 NWs.[252]

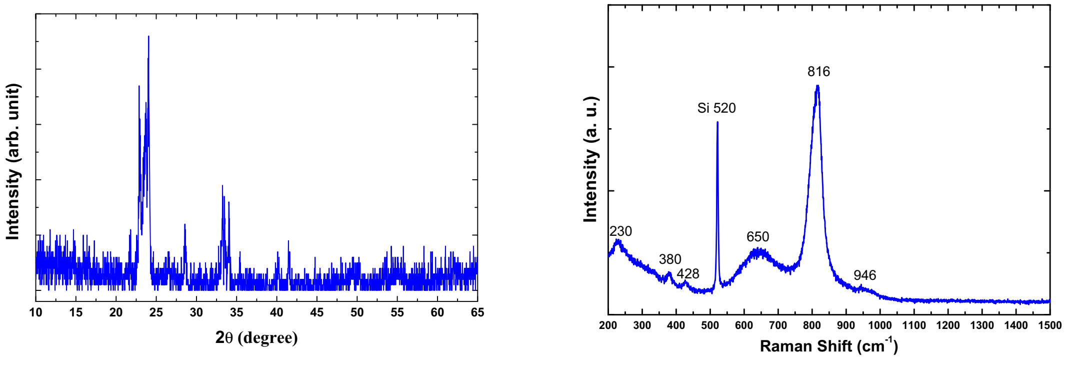

(a)

(b)

Figure 73: Characterization of NaOH catalyzed WO_3 NWs: XRD and Raman. (a) XRD pattern of the as-prepared sample, and (b) Raman spectrum on NWs region.

TEM specimen was prepared by using carbon grid to slightly scratch the as-grown sample. Fig. 74 show the feature of majority NWs. The growth direction was difficult to determined due to the presence of streaking in SAED pattern (not shown here), which presumably

---

[18] ICDD PDF 04-011-1708, *a*=7.35 Å, *b*=12.5 Å, *c*=7.70 Å

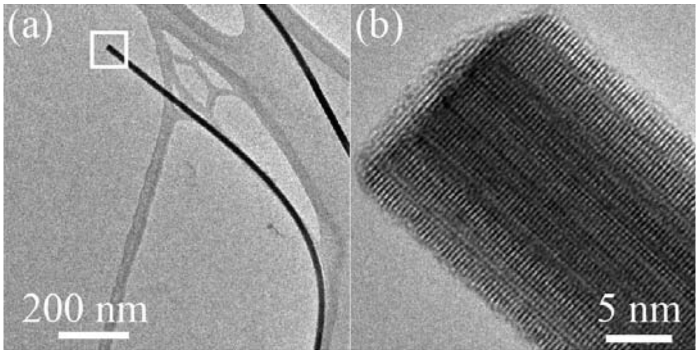

Figure 74: TEM Characterization of NaOH catalyzed WO_3: (a) TEM image of one nanowire with diameter ca. 20 nm, and (b) HRTEM images on the tip region showing absence of catalytic particle.

arose from stacking defaults during the NW growth. HRTEM revealed dominant plane spacings of 3.90 and 3.80 Å, in favorable comparison to the XRD peak at 22.92° and 23.66°. It was worth noting that catalyst particles were absent on the tip of NWs during the TEM observation. Based on the above characterizations, this thesis concluded that the majority

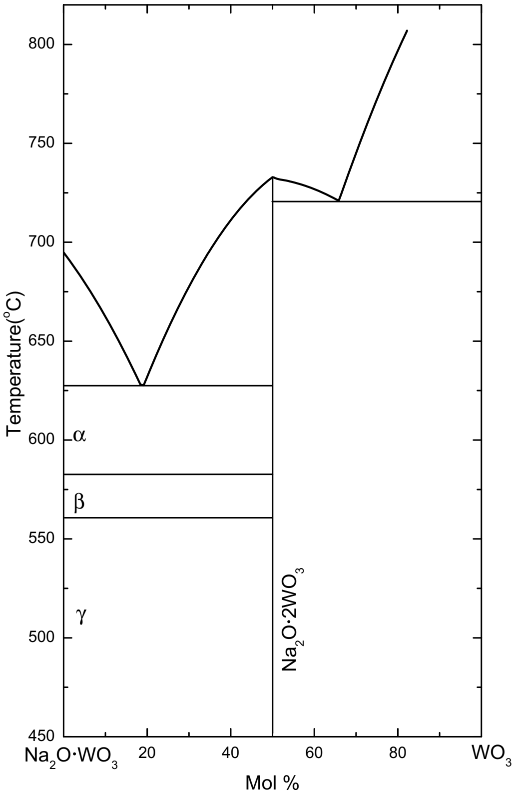

Figure 75: Phase diagram of Na_2WO_4-WO_3 reproduced from Ref. [152]

of NW belonged to tungsten oxide, although Na doping cannot be ruled out completely. According to the Na_2WO_4-WO_3 phase diagram in Fig. 75, the eutectic temperature is ca. 720 °C.[253] Further investigations are required to better understanding the growth mechanism. The author suggested using other alkali metal compound as catalyst to probe the WO_3 growth.

6.2 Preliminary Results on Molybdenum Oxide Growth Using Glass

The various growth morphologies found using alkali metal based materials as catalysts demonstrated the proposed VSS mechanism and transverse mode was a general phenomenon, and broad engineering space could be explored to control the dimension of MoO_3. As an example, this study further illustrated the tunable growth of MoO_3 nanoribbons on glass substrate. Achieving morphology controlled growth of MoO_3 on transparent substrates, e.g. glass, is an important progress towards process integration and device fabrication in photon-energy related applications.

This thesis studied the effect of temperature, oxygen partial pressure, and growth time towards MoO_3 deposition on glass substrates. Each factor was divided into two levels with T at 700 and 800 °C, O_2 flow at 1 and 10 sccm, and growth time of 15 and 60 min, respectively. And the morphological variations revealed by SEM imaging were summarized in Table 24. The 800-1-15 combination produced dense MoO_3 nanoplate with length about 10 μm, width 300 $\sim$ 500 nm and thickness less than 100 nm, as illustrated in Fig. 76. These MoO_3 nanoplates were of high crystalline quality and could potentially show enhanced photoelectrochemical and electrochromic activities.

For future work, the author suggested several following perspectives:

Table 24: MoO_3 growth on glass

Growth Conditions			
T (°C)	O_2 (sccm)	Time (min)	Morphology
700	10	15	about 50 μm belts, some towers
700	1	60	irregular shape, not too much growth
700	10	60	particle almost all on tip of belts, many towers
800	1	15	tens μm belts with sharp edge (100 nm thick and 1 micrometer wide) dominate
800	1	60	exhibiting ITO features, particles on tips of belt, many tower like structures
800	10	15	rounded edge flakes dominate, modest density tapering belt, and some possible tower
800	10	60	ITO/glass features, aggregated belts, some towers

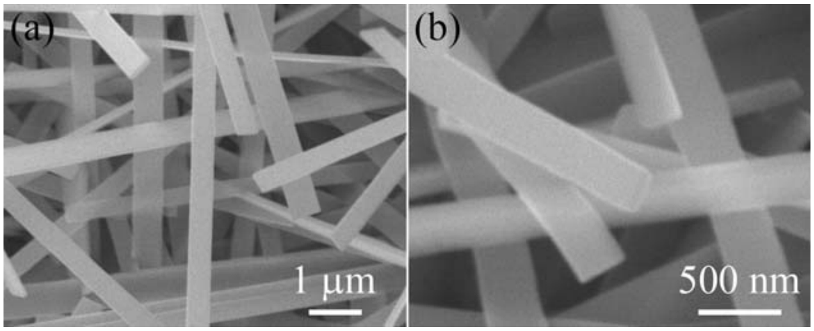

Figure 76: Optimized MoO_3 nanoplates growth on glass.

1. further investigation of WO_3 growth using alkali metal ions as catalysts;
2. probing the VSS growth method of MoO_3 using HRTEM and analyzing the catalyst state; and
3. applying TEM-Raman integrated study onto other nanostructures.

REFERENCES

[1] Jinzhan Su et al. "Vertically Aligned WO3 Nanowire Arrays Grown Directly on Transparent Conducting Oxide Coated Glass: Synthesis and Photoelectrochemical Properties". *Nano Letters* 11.1 (2010), 203–208 (see pp. 1, 33)

[2] Apichon Watcharenwong et al. "Anodic growth of nanoporous WO3 films: Morphology, photoelectrochemical response and photocatalytic activity for methylene blue and hexavalent chrome conversion". *Journal of Electroanalytical Chemistry* 612.1 (2008), 112–120 (see pp. 1, 5)

[3] Donald E. Macphee et al. "A tungsten oxide-based photoelectrocatalyst for degradation of environmental contaminants". *Journal of Solid State Electrochemistry* 15.1 (2010), 99–103 (see p. 1)

[4] Robert H Coridan et al. "Electrical and Photoelectrochemical Properties of WO3/Si Tandem Photoelectrodes". *The Journal of Physical Chemistry C* 117.14 (2013), 6949–6957 (see p. 1)

[5] Tetsuzo Yoshimura. "Oscillator strength of small-polaron absorption in WOx electrochromic thin films". *Journal of Applied Physics* 57.3 (1985), 911–919 (see p. 1)

[6] Roger J Mortimer. "Electrochromic Materials". *Annual Review of Materials Research* 41.1 (2011), 241–268 (see p. 1)

[7] L Britnell et al. "Strong Light-Matter Interactions in Heterostructures of Atomically Thin Films". *Science* 340.6138 (2013), 1311–1314 (see p. 1)

[8] C Ballif, M Regula, and F Lévy. "Optical and electrical properties of semiconducting WS2 thin films: From macroscopic to local probe measurements". *Solar Energy Materials and Solar Cells* 57.2 (1999), 189–207 (see pp. 1, 102)

[9] F K Perkins et al. "Chemical Vapor Sensing with Monolayer MoS2". *Nano Letters* 13.2 (2013), 668–673 (see p. 1)

[10] Zhebo Chen et al. "Core-shell MoO3-MoS2 nanowires for hydrogen evolution: A functional design for electrocatalytic materials". *Nano Letters* 11.10 (2011), 4168–4175 (see pp. 1, 6, 66, 92)

[11] U.S. Department of Energy. *Energy Efficiency Trends in Residential and Commercial Buildings*. Tech. rep. Department of Energy, 2008 (see p. 2)

[12] Carl M Lampert. "Smart switchable glazing for solar energy and daylight control". *Solar Energy Materials and Solar Cells* 52.3–4 (1998), 207–221 (see pp. 2, 3)

[13] Satyen K. Deb. “Opportunities and challenges in science and technology of WO3 for electrochromic and related applications”. *Solar Energy Materials and Solar Cells* 92.2 (2008), 245–258 (see pp. 2, 28, 30)

[14] Nada A O’Brien, J Gordon, H Mathew, and Bryant P Hichwa. “Electrochromic coatings-applications and manufacturing issues”. *Thin Solid Films* 345.2 (1999), 312–318 (see p. 2)

[15] C G Granqvist. “Electrochromic tungsten oxide films: Review of progress 1993-1998”. *Solar Energy Materials and Solar Cells* 60.3 (2000), 201–262 (see p. 3)

[16] D Dini, F Decker, and E Masetti. “A comparison of the electrochromic properties of WO3 films intercalated with H+, Li+ and Na+”. English. *Journal of Applied Electrochemistry* 26.6 (1996), 647–653 (see p. 4)

[17] Frank E. Osterloh. “Inorganic Materials as Catalysts for Photochemical Splitting of Water”. *Chemistry of Materials* 20.1 (2008), 35–54 (see p. 4)

[18] Fenggong Wang, Cristiana Di Valentin, and Gianfranco Pacchioni. “Doping of WO3 for Photocatalytic Water Splitting: Hints from Density Functional Theory”. *The Journal of Physical Chemistry C* 116.16 (2012), 8901–8909 (see pp. 4, 6)

[19] Michael Gratzel. “Photoelectrochemical cells”. *Nature* 414.6861 (2001), 338–344 (see p. 5)

[20] Michael Grätzel. “The artificial leaf, bio-mimetic photocatalysis”. *cattech* 3 (1999), 3–17 (see p. 5)

[21] Maria Hepel and Jin Luo. “Photoelectrochemical mineralization of textile diazo dye pollutants using nanocrystalline WO3 electrodes”. *Electrochimica Acta* 47.5 (2001), 729–740 (see p. 5)

[22] Jin Luo and Maria Hepel. “Photoelectrochemical degradation of naphthol blue black diazo dye on WO3 film electrode”. *Electrochimica Acta* 46.19 (2001), 2913–2922 (see p. 5)

[23] Federico M Pesci et al. “Charge Carrier Dynamics on Mesoporous WO3 during Water Splitting”. *The Journal of Physical Chemistry Letters* 2.15 (2011), 1900–1903 (see p. 5)

[24] Damián Monllor-Satoca et al. “Photoelectrochemical Behavior of Nanostructured WO3 Thin-Film Electrodes: The Oxidation of Formic Acid”. *ChemPhysChem* 7.12 (2006), 2540–2551 (see p. 5)

[25] Xianwei Sha et al. “Hydrogen Absorption and Diffusion in Bulk a-MoO3”. *The Journal of Physical Chemistry C* 113.26 (2009), 11399–11407 (see pp. 6, 63)

[26] Kai Huang et al. “The catalyst-free synthesis of large-area tungsten oxide nanowire arrays on ITO substrate and field emission properties”. *Materials Research Bulletin* 43.4 (2008), 919–925 (see pp. 6, 31)

[27] Maik R J Scherer and Ullrich Steiner. “Efficient Electrochromic Devices Made from 3D Nanotubular Gyroid Networks”. *Nano Letters* (2012) (see p. 6)

[28] Andrew Mills, Richard H Davies, and David Worsley. “Water purification by semiconductor photocatalysis”. *Chemical Society Reviews* 22.6 (1993), 417–425 (see p. 6)

[29] Daniel Merki and Xile Hu. “Recent developments of molybdenum and tungsten sulfides as hydrogen evolution catalysts”. *Energy and Environmental Science* 4.10 (2011), 3878–3888 (see p. 6)

[30] Sara B Habib, Eleazar Gonzalez, and Robert F Hicks. “Atmospheric oxygen plasma activation of silicon (100) surfaces”. *Journal of Vacuum Science and Technology A* 28.3 (2010) (see p. 11)

[31] Joseph Goldstein et al. *Scanning Electron Microscopy and X-Ray Microanalysis*. 3rd. Springer, 2007, 690. ISBN: 978-1-4615-0215-9 (see pp. 12, 13)

[32] JEOL. *Scanning Electron Microscope A To Z: Basic Knowledge For Using The SEM* (see p. 13)

[33] Peter J. Goodhew. *Electron Microscopy and Analysis*. 3rd ed. CRC Press, 2000, 254. ISBN: 0748409688 (see pp. 13, 16)

[34] A Tersigni et al. “Reciprocal-space mapping of lateral single-crystal domains with grazing-incidence x-ray diffraction for tetracene on H/Si(001)”. *Physical Review B* 84.3 (2011), 35303 (see p. 16)

[35] MS Goorsky and BK Tanner. “Grazing Incidence In-plane Diffraction Measurement of In-plane Mosaic with Microfocus X-ray Tubes”. *Crystal Research and Technology* (2002), 645–653 (see p. 16)

[36] David B Williams. and C.Barry Carter. *Transmission Electron Microscopy: a text book for material science*. 2nd. New York: Springer, 2009, 760. ISBN: 978-0387765020 (see pp. 17, 19)

[37] R. L. McCreery. *Raman Spectroscopy for Chemical Analysis*. 3rd. New York: Wiley, 2000, 452. ISBN: 978-0-471-25287-0 (see p. 19)

[38] Andrew Mills and Jishun Wang. “Photobleaching of methylene blue sensitised by TiO2: an ambiguous system?” *Journal of Photochemistry and Photobiology A: Chemistry* 127.1–3 (1999), 123–134 (see p. 20)

[39] G Maret and P E Wolf. “Multiple light scattering from disordered media. The effect of brownian motion of scatterers”. English. *Zeitschrift für Physik B Condensed Matter* 65.4 (1987), 409–413 (see p. 21)

[40] S P Tandon and J P Gupta. “Measurement of Forbidden Energy Gap of Semiconductors by Diffuse Reflectance Technique”. *physica status solidi (b)* 38.1 (1970), 363–367 (see pp. 21, 22)

[41] Paul Kubelka and F Munk. “Ein Beitrag zur Optik der Farbanstriche (An article on optics of paint layers)”. *Z. Tech. Phys* 31.1930 (1931), 1–16 (see p. 21)

[42] AE Morales, ES Mora, and U Pal. “Use of diffuse reflectance spectroscopy for optical characterization of un-supported nanostructures”. *Revista Mexicana de Fisica S* 53.5 (2007), 18–22 (see p. 22)

[43] Shimadzu. *UV-2600/2700 Integrating Sphere Attachment Instruction Manual*. 2012 (see p. 24)

[44] C G Granqvist. “Electrochromic materials: Microstructure, electronic bands, and optical properties”. English. *Applied Physics A* 57.1 (1993), 3–12 (see p. 25)

[45] Haidong Zheng et al. “Nanostructured Tungsten Oxide- Properties, Synthesis, and Applications”. *Advanced Functional Materials* 21.12 (2011), 2175–2196 (see pp. 26, 32)

[46] Ryan Chatten, Alan V Chadwick, Aline Rougier, and Philip J D Lindan. “The oxygen vacancy in crystal phases of WO3”. *The journal of physical chemistry. B* 109.8 (2005), 3146–56 (see pp. 26, 30)

[47] D B Migas, V L Shaposhnikov, V N Rodin, and V E Borisenko. “Tungsten oxides. I. Effects of oxygen vacancies and doping on electronic and optical properties of different phases of WO3”. *Journal of Applied Physics* 108.9 (2010), 93713 (see p. 26)

[48] M Boulova and G Lucazeau. “Crystallite Nanosize Effect on the Structural Transitions of WO3 Studied by Raman Spectroscopy”. *Journal of Solid State Chemistry* 167.2 (2002), 425–434 (see p. 26)

[49] M Gillet et al. “The structure and electrical conductivity of vacuum-annealed WO3 thin films”. *Thin Solid Films* 467.1–2 (2004), 239–246 (see p. 26)

[50] Jeremy Sloan et al. “Defect and Ordered Tungsten Oxides Encapsulated Inside 2H-WX2(X=S and Se) Fullerene-Related Structures”. *Journal of Solid State Chemistry* 144.1 (1999), 100–117 (see pp. 27, 96)

[51] Y Shingaya, T Nakayama, and M Aono. *Optical electric field enhancement element and probe using the same*. 2013 (see p. 27)

[52] J T Devreese. “Polarons” (1996). arXiv: `0004497v2 [arXiv:cond-mat]` (see p. 29)

[53] Maria Hepel. “Electrochromic WO3 Films: Nanotechnology Experiments in Instrumental Analysis and Physical Chemistry Laboratories”. *Journal of Chemical Education* 85.1 (2008), 125 (see p. 29)

[54] LF Zhu, JC She, and JY Luo. “Study of Physical and Chemical Processes of H2 Sensing of Pt-Coated WO3 Nanowire Films”. *Journal of Physical ch* (2010), 15504–15509 (see p. 31)

[55] Jun Zhou et al. “Three-Dimensional Tungsten Oxide Nanowire Networks”. *Advanced Materials* 17.17 (2005), 2107–2110 (see p. 31)

[56] Baobao Cao, Jiajun Chen, Xiaojun Tang, and Weilie Zhou. “Growth of monoclinic WO3 nanowire array for highly sensitive NO2 detection”. *Journal of Materials Chemistry* 19.16 (2009), 2323–2327 (see p. 31)

[57] Yun-Tsung Hsieh et al. “Growth and optical properties of uniform tungsten oxide nanowire bundles via a two-step heating process by thermal evaporation”. *Thin Solid Films* 519.5 (2010), 1668–1672 (see pp. 31, 33, 51)

[58] Gang Gu et al. “Tungsten Oxide Nanowires on Tungsten Substrates”. *Nano Letters* 2.8 (2002), 849–851 (see pp. 31, 33)

[59] Chi Lingfei et al. “An approach for synthesizing various types of tungsten oxide nanostructure”. *Nanotechnology* 17.22 (2006), 5590 (see p. 31)

[60] Jyothish Thangala et al. “Large-Scale, Hot-Filament-Assisted Synthesis of Tungsten Oxide and Related Transition Metal Oxide Nanowires”. *Small* 3.5 (2007), 890–896 (see pp. 31, 33)

[61] Mu-Tung Chang et al. “Nitrogen-Doped Tungsten Oxide Nanowires: Low-Temperature Synthesis on Si, and Electrical, Optical, and Field-Emission Properties”. *Small* 3.4 (2007), 658–664 (see pp. 31, 33)

[62] S. J. Wang et al. “Electronic transport property of single-crystalline hexagonal tungsten trioxide nanowires”. *Applied Physics Letters* 94.26 (2009), 263106 (see p. 31)

[63] Christian Klinke et al. "Tungsten Oxide Nanowire Growth by Chemically Induced Strain". *The Journal of Physical Chemistry B* 109.38 (2005), 17787–17790 (see pp. 31, 33, 58)

[64] Yunho Baek and Kijung Yong. "Controlled Growth and Characterization of Tungsten Oxide Nanowires Using Thermal Evaporation of WO3 Powder". *The Journal of Physical Chemistry C* 111.3 (2007), 1213–1218 (see p. 31)

[65] Karuppanan Senthil, Kijung Yong, Senthil Karuppanan, and Yong Kijung. "Growth and characterization of stoichiometric tungsten oxide nanorods by thermal evaporation and subsequent annealing". *Nanotechnology* 18.39 (2007), 395604 (see pp. 31, 51)

[66] S V Pol et al. "Synthesis of WO3 Nanorods by Reacting WO(OMe)4 under Autogenic Pressure at Elevated Temperature Followed by Annealing". *Inorganic Chemistry* 44.26 (2005), 9938–9945 (see p. 32)

[67] Kwangyeol Lee, Won Seok Seo, and Joon T Park. "Synthesis and Optical Properties of Colloidal Tungsten Oxide Nanorods". *Journal of the American Chemical Society* 125.12 (2003), 3408–3409 (see pp. 32, 33)

[68] Zhanjun Gu et al. "Large-scale synthesis of single-crystal hexagonal tungsten trioxide nanowires and electrochemical lithium intercalation into the nanocrystals". *Journal of Solid State Chemistry* 180.1 (2007), 98–105 (see p. 32)

[69] S Rajagopal et al. "Controlled Growth of WO3 Nanostructures with Three Different Morphologies and Their Structural, Optical, and Photodecomposition Studies". *Nanoscale Research Letters* 4.11 (2009), 1335–1342 (see p. 33)

[70] V V Fomichev, M E Poloznikova, and O I Kondratov. "Structural features and spectroscopic and energy characteristics of alkali metal molybdates and tungstates". *Russian Chemical Reviews* 61.9 (1992), 877 (see pp. 41, 43, 64, 78, 79)

[71] Franklin D Hardcastle and Israel E Wachs. "Determination of the molecular structures of tungstates by Raman spectroscopy". *Journal of Raman Spectroscopy* 26.6 (1995), 397–405 (see p. 42)

[72] S. T. Triantafyllou and P. C. Christidis. "Triclinic sodium tungsten oxide, Na5W14O44". *Acta Crystallographica Section C Crystal Structure Communications* 55.6 (1999), 838–841 (see p. 42)

[73] Yuan-Ron Ma, Chi-Ming Lin, Chun-Liang Yeh, and Rong-Tan Huang. "Synthesis and characterization of one-dimensional WO2 nanorods". *Journal of Vacuum Science and Technology B: Microelectronics and Nanometer Structures* 23.5 (2005), 2141–2145 (see p. 43)

[74] Chongshen Guo et al. “Morphology-Controlled Synthesis of W18O49 Nanostructures and Their Near-Infrared Absorption Properties”. *Inorganic Chemistry* 51.8 (2012), 4763–4771 (see p. 43)

[75] Jian-wei Liu et al. “Ultrathin W18O49 Nanowire Assemblies for Electrochromic Devices”. *Nano Letters* (2013), 1–8 (see p. 43)

[76] E Salje. “Lattice dynamics of WO3”. *Acta Crystallographica Section A: Crystal Physics, ...* 31.3 (1975), 360–363 (see pp. 43, 57, 128)

[77] M F Daniel et al. “Infrared and Raman study of WO3 tungsten trioxides and WO3xH2O tungsten trioxide hydrates”. *Journal of Solid State Chemistry* 67.2 (1987), 235–247 (see pp. 43, 128)

[78] C Luz Lima et al. “Temperature-induced phase transformations in Na2WO4 and Na2MoO4 crystals”. *Journal of Raman Spectroscopy* 42.4 (2011), 799–802 (see p. 43)

[79] F Knee. “The Raman spectrum of sodium ditungstate, Na2W2O7”. *Journal of Physics and Chemistry of Solids* (1979) (see p. 43)

[80] E A Gulbransen and K F Andrew. “Kinetics of the Oxidation of Pure Tungsten from 500° to 1300°C”. *Journal of The Electrochemical Society* 107.7 (1960), 619–628 (see p. 51)

[81] Anna Warren, Anders Nylund, and Ingemar Olefjord. “Oxidation of tungsten and tungsten carbide in dry and humid atmospheres”. *International Journal of Refractory Metals and Hard Materials* 14.5–6 (1996), 345–353 (see pp. 51, 58)

[82] Yan Qiu YQ Zhu et al. “Tungsten oxide tree-like structures”. *Chemical Physics Letters* 309.5–6 (1999), 327–334 (see p. 51)

[83] Erik; Wolf-Dieter Schubert Lassner. *Tungsten : properties, chemistry, technology of the element, alloys, and chemical compounds*. Springer, 1999, 422. ISBN: 978-0306450532 (see pp. 54, 58)

[84] Lalji Dixit, D L Gerrard, and H J Bowley. “Laser Raman Spectra of Transition Metal Oxides and Catalysts”. *Applied Spectroscopy Reviews* 22.2-3 (1986), 189–249 (see pp. 57, 69, 128)

[85] G F You and John T L Thong. “Thermal oxidation of polycrystalline tungsten nanowire”. *Journal of Applied Physics* 108.9 (2010) (see p. 58)

[86] V K Sarin. “Morphological changes occurring during reduction of WO3”. English. *Journal of Materials Science* 10.4 (1975), 593–598 (see p. 58)

[87] Tao Sheng et al. “Growth of ultra-long sodium tungsten oxide and tungsten oxide nanowires: Effects of impurity and residue deposition”. *Journal of Crystal Growth* 395 (2014), 61–67 (see p. 59)

[88] S K Deb. “Physical Properties of a Transition Metal Oxide: Optical and Photoelectric Properties of Single Crystal and Thin Film Molybdenum Trioxide”. *Proceedings of the Royal Society of London. Series A. Mathematical and Physical Sciences* 304.1477 (1968), 211–231 (see pp. 62, 91)

[89] Petre Badica. “Preparation through the Vapor Transport and Growth Mechanism of the First-Order Hierarchical Structures of MoO3 Belts on Sillimanite Fibers”. *Crystal Growth and Design* (2007), 2–9 (see pp. 62, 65)

[90] Tao He and Jiannian Yao. “Photochromism of molybdenum oxide”. *Journal of Photochemistry and Photobiology C: Photochemistry Reviews* 4.2 (2003), 125–143 (see pp. 63, 65)

[91] J N Yao, K Hashimoto, and A Fujishima. “Photochromism induced in an electrolytically pretreated MoO3 thin film by visible light”. *Nature* 355.6361 (1992), 624–626 (see p. 63)

[92] Paul E Sheehan and Charles M Lieber. “Nanotribology and Nanofabrication of MoO3 Structures by Atomic Force Microscopy”. *Science* 272.5265 (1996), 1158–1161 (see p. 63)

[93] Yuping Chen et al. “Single-crystalline orthorhombic molybdenum oxide nanobelts: synthesis and photocatalytic properties”. *CrystEngComm* 12.11 (2010), 3740–3747 (see p. 63)

[94] E Comini, L Yubao, Y Brando, and G Sberveglieri. “Gas sensing properties of MoO3 nanorods to CO and CH3OH”. *Chemical Physics Letters* 407.4–6 (2005), 368–371 (see p. 63)

[95] Antonella M Taurino et al. “Synthesis, electrical characterization, and gas sensing properties of molybdenum oxide nanorods”. *Applied Physics Letters* 88.15 (2006), 152111–152113 (see p. 63)

[96] Supab Choopun et al. “Orthorhombic Molybdenum Trioxide Whiskers by Vapor Transport Method”. *Japanese Journal of Applied Physics* 43.1A/B (2004), pages (see p. 63)

[97] Y B Li, Y Bando, D Golberg, and K Kurashima. “Field emission from MoO3 nanobelts”. *Applied Physics Letters* 81.26 (2002), 5048–5050 (see pp. 63, 65)

[98] Jun Zhou et al. “Synthesis and field-emission properties of aligned MoO3 nanowires”. *Applied Physics Letters* 83.13 (2003), 2653–2655 (see pp. 63, 65, 66)

[99] M E Spahr, P Novák, O Haas, and R Nesper. “Electrochemical insertion of lithium, sodium, and magnesium in molybdenum(VI) oxide”. *Journal of Power Sources* 54.2 (1995), 346–351 (see p. 63)

[100] Weiyang Li, Fangyi Cheng, Zhanliang Tao, and Jun Chen. “Vapor-Transportation Preparation and Reversible Lithium Intercalation Deintercalation of a-MoO3 nanorods”. *J. Phys. Chem. B* (2006), 119–124 (see p. 63)

[101] Zhibin Hu et al. “K-Enriched MoO3 Nanobundles: A Layered Structure with High Electric Conductivity”. *The Journal of Physical Chemistry C* 116.6 (2011), 3962–3967 (see pp. 63, 88)

[102] Tarsame S Sian and G B Reddy. “Effect of Size and Valency of Intercalant Ions on Optical Properties of Polycrystalline MoO3 Films”. *Journal of The Electrochemical Society* 152.12 (2005), A2323–A2326 (see p. 63)

[103] L. Q. Mai et al. “Lithiated MoO3 Nanobelts with Greatly Improved Performance for Lithium Batteries”. *Advanced Materials* 19.21 (2007), 3712–3716 (see p. 63)

[104] Srirama Hariharan, Kuppan Saravanan, and Palani Balaya. “a-MoO3: A high performance anode material for sodium-ion batteries”. *Electrochemistry Communications* 31 (2013), 5–9 (see p. 63)

[105] S H Elder et al. “The Discovery and Study of Nanocrystalline TiO2-(MoO3) Core-Shell Materials”. *Journal of the American Chemical Society* 122.21 (2000), 5138–5146 (see p. 63)

[106] D.-T. Nguyen et al. “Effect of the thickness of the MoO3 layers on optical properties of MoO3/Ag/MoO3 multilayer structures”. *Journal of Applied Physics* 112.6 (2012), 63505–63508 (see p. 63)

[107] Xiao Lin Li and Ya Dong Li. “Formation of MoS2 Inorganic Fullerenes (IFs) by the Reaction of MoO3 Nanobelts and S”. *Chemistry – A European Journal* 9.12 (2003), 2726–2731 (see p. 63)

[108] Yu-Chuan Lin et al. “Wafer-scale MoS2 thin layers prepared by MoO3 sulfurization”. *Nanoscale* 4.20 (2012), 6637–6641 (see pp. 63, 98, 102)

[109] A K Geim and I V Grigorieva. “Van der Waals heterostructures”. *Nature* 499.7459 (2013), 419–425 (see p. 63)

[110] Minoru Itoh, Kousuke Hayakawa, and Shuji Oishi. “Optical properties and electronic structures of layered MoO3 single crystals”. *Journal of Physics: Condensed Matter* 13.31 (2001), 6853 (see pp. 64, 69)

[111] J Dumas, C Schlenker, J Marcus, and R Buder. “Nonlinear Conductivity and Noise in the Quasi One-Dimensional Blue Bronze K0.30MoO3”. *Physical Review Letters* 50.10 (1983), 757–760 (see p. 64)

[112] M Sing et al. “Electronic structure of metallic K0.3MoO3 and insulating MoO3 from high-energy spectroscopy”. *Physical Review B* 60.12 (1999), 8559–8568 (see p. 65)

[113] Xiao-Lin Li, Jun-Feng Liu, and Ya-Dong Li. “Low-temperature synthesis of large-scale single-crystal molybdenum trioxide MoO3 nanobelts”. *Applied Physics Letters* 81.25 (2002), 4832–4834 (see p. 65)

[114] Tian Xia et al. “Morphology-Controllable Synthesis and Characterization of Single-Crystal Molybdenum Trioxide”. *The Journal of Physical Chemistry B* 110.5 (2006), 2006–2012 (see p. 65)

[115] Guicun Li et al. “Molybdenum trioxide nanostructures: the evolution from helical nanosheets to crosslike nanoflowers to nanobelts”. *The journal of physical chemistry. B* 110.48 (2006), 24472–5 (see p. 65)

[116] G A Camacho-Bragado and M Jose-Yacaman. “Self-assembly of molybdite nanoribbons”. English. *Applied Physics A* 82.1 (2006), 19–22 (see p. 65)

[117] H C Zeng. “Vapour phase growth of orthorhombic molybdenum trioxide crystals at normal pressure of purified air”. *Journal of Crystal Growth* 186.3 (1998), 393–402 (see p. 65)

[118] Jianqiang Li, Pan Wei, Jian Chen, and Li Rongti. “Preparation and Growth Mechanism of Molybdenum Trioxide Whisker”. *Journal of the American Ceramic Society* 85.8 (2002), 2116–2118 (see p. 65)

[119] Bin Yan et al. “Orientation Controllable Growth of MoO3 Nanoflakes : Micro-Raman , Field Emission , and Birefringence Properties”. *J. Phys. Chem. C* (2009), 20259–20263 (see pp. 65, 66)

[120] Xiaohui Chen et al. “Synthesis and Characterization of Hexagonal and Truncated Hexagonal Shaped MoO3 Nanoplates”. *The Journal of Physical Chemistry C* 113.52 (2009), 21582–21585 (see p. 66)

[121] Bin Hu, Liqiang Mai, Wen Chen, and Fan Yang. “From MoO3 Nanobelts to MoO2 Nanorods: Structure Transformation and Electrical Transport”. *ACS Nano* 3.2 (2009), 478–482 (see p. 66)

[122] Lili Cai, Pratap M Rao, and Xiaolin Zheng. "Morphology-controlled flame synthesis of single, branched, and flower-like α-MoO3 nanobelt arrays." *Nano letters* 11.2 (2011), 872–7 (see p. 66)

[123] A Chithambararaj, N S Sanjini, S Velmathi, and A Chandra Bose. "Preparation of h-MoO3 and alpha-MoO3 nanocrystals: comparative study on photocatalytic degradation of methylene blue under visible light irradiation". *Physical Chemistry Chemical Physics* 15.35 (2013), 14761–14769 (see p. 66)

[124] William M. Haynes, ed. *CRC Handbook of Chemistry and Physics*. Ohio: CRC Press, 1977. ISBN: 0-8493-0549-8 (see p. 67)

[125] Jose V Silveira et al. "Temperature-dependent Raman spectroscopy study in MoO3 nanoribbons". *Journal of Raman Spectroscopy* 43.10 (2012), 1407–1412 (see p. 69)

[126] T. Siciliano et al. "Characteristics of molybdenum trioxide nanobelts prepared by thermal evaporation technique". *Materials Chemistry and Physics* 114.2-3 (2009), 687–691 (see pp. 70, 79)

[127] Kazuo Eda. "Raman spectra of hydrogen molybdenum bronze, H0.30MoO3". *Journal of Solid State Chemistry* 98.2 (1992), 350–357 (see pp. 70, 79)

[128] Tao Sheng, Baobao Cao, Yong Zhang, and Haitao Zhang. "New growth modes of molybdenum oxide layered 1D structures using alternative catalysts: transverse mode vs. axial mode". *CrystEngComm* 17.5 (2015), 1139–1150 (see p. 71)

[129] D. Wang, D. S. Su, and R. Schlögl. "Electron Beam Induced Transformation of MoO3 to MoO2 and a New Phase MoO". *Zeitschrift für anorganische und allgemeine Chemie* 630.7 (2004), 1007–1014 (see p. 72)

[130] Torsten Brezesinski, John Wang, Sarah H Tolbert, and Bruce Dunn. "Ordered mesoporous alpha-MoO3 with isooriented nanocrystalline walls for thin-film pseudocapacitors". *Nat Mater* 9.2 (2010), 146–151 (see p. 73)

[131] Kourosh Kalantar-zadeh et al. "Synthesis of nanometre-thick MoO3 sheets". *Nanoscale* (2010), 429–433 (see p. 73)

[132] Padmanabha pradeep Chavvakula. "Synthesis of one-dimensional nanostructures of transition metal oxides for nanoscale smart devices". Master thesis. University of North Carolina at Charlotte, 2011 (see p. 73)

[133] R S Wagner and W C Ellis. "Vapor-Liquid-Solid Mechanism of Single Crystal Growth". *Applied Physics Letters* 4.5 (1964), 89–90 (see p. 74)

[134] E I Givargizov. “Fundamental aspects of VLS growth”. *Journal of Crystal Growth* 31 (1975), 20–30 (see p. 74)

[135] Charles M Lieber. “One-dimensional nanostructures: Chemistry, physics and applications”. *Solid State Communications* 107.11 (1998), 607–616 (see p. 74)

[136] Allon I Hochbaum, Rong Fan, Rongrui He, and Peidong Yang. “Controlled growth of Si nanowire arrays for device integration.” *Nano letters* 5.3 (2005), 457–60 (see p. 74)

[137] Dan Dalacu, Alicia Kam, D Guy Austing, and Philip J Poole. “Droplet Dynamics in Controlled InAs Nanowire Interconnections”. *Nano Letters* 13.6 (2013), 2676–2681 (see p. 74)

[138] Hong-Di Xiao et al. “Structure and growth mechanism of quasi-aligned GaN layer-built nanotowers”. *Applied Physics Letters* 100.21 (2012), 213101–213103 (see p. 74)

[139] V G Dubrovskii et al. “New Mode of Vapor-Liquid-Solid Nanowire Growth”. *Nano Letters* 11.3 (2011), 1247–1253 (see p. 74)

[140] Yufeng Hao et al. “Periodically Twinned Nanowires and Polytypic Nanobelts of ZnS: The Role of Mass Diffusion in Vapor-Liquid-Solid Growth”. *Nano Letters* 6.8 (2006), 1650–1655 (see p. 74)

[141] M H Huang et al. “Catalytic Growth of Zinc Oxide Nanowires by Vapor Transport”. *Advanced Materials* 13.2 (2001), 113–116 (see p. 74)

[142] Niranjan S Ramgir et al. “Reactive VLS and the Reversible Switching between VS and VLS Growth Modes for ZnO Nanowire Growth”. *The Journal of Physical Chemistry C* 114.23 (2010), 10323–10329 (see p. 74)

[143] A H HEUER and P BURNETT. “Evidence for MgO Whisker Growth by a Vapor-Liquid-Solid Mechanism”. *Journal of the American Ceramic Society* 50.11 (1967), 627–628 (see p. 74)

[144] Kazuki Nagashima, Takeshi Yanagida, Hidekazu Tanaka, and Tomoji Kawai. “Control of magnesium oxide nanowire morphologies by ambient temperature”. *Applied Physics Letters* 90.23 (2007), 233103 (see p. 74)

[145] Zheng Wei Pan, Zu Rong Dai, Chris Ma, and Zhong L Wang. “Molten Gallium as a Catalyst for the Large-Scale Growth of Highly Aligned Silica Nanowires”. *Journal of the American Chemical Society* 124.8 (2002), 1817–1822 (see p. 74)

[146] Fuwei Zhuge et al. “Fundamental strategy for creating VLS grown TiO2 single crystalline nanowires”. *Journal of Physical Chemistry C* 116.45 (2012), 24367–24372 (see p. 74)

[147] Alfredo M Morales and Charles M Lieber. “A Laser Ablation Method for the Synthesis of Crystalline Semiconductor Nanowires”. *Science* 279.5348 (1998), 208–211 (see p. 74)

[148] Yi Cui et al. “Diameter-controlled synthesis of single-crystal silicon nanowires”. *Applied Physics Letters* 78.15 (2001), 2214–2216 (see p. 74)

[149] Mark S Gudiksen et al. “Growth of nanowire superlattice structures for nanoscale photonics and electronics”. *Nature* 415.6872 (2002), 617–620 (see p. 74)

[150] M T Björk et al. “One-dimensional Steeplechase for Electrons Realized”. *Nano Letters* 2.2 (2002), 87–89 (see p. 74)

[151] Lincoln J Lauhon, Mark S Gudiksen, Deli Wang, and Charles M Lieber. “Epitaxial core-shell and core-multishell nanowire heterostructures”. *Nature* 420.6911 (2002), 57–61 (see p. 74)

[152] Fritz Hoermann. “Beitrag zur Kenntnis der Molybdate und Wolframate. Die binaren Systeme”. *Zeitschrift fur anorganische und allgemeine Chemie* 177.1 (1929), 145–186 (see pp. 75, 129)

[153] Kittitat Subannajui et al. “ZnO Nanowire Growth: A Deeper Understanding Based on Simulations and Controlled Oxygen Experiments”. *Crystal Growth and Design* 10.4 (2010), 1585–1589 (see p. 76)

[154] Keith Schofield. “New Method To Minimize High-Temperature Corrosion Resulting from Alkali Sulfate and Chloride Deposition in Combustion Systems. II. Molybdenum Salts”. *Energy and Fuels* 19.5 (2005), 1898–1905 (see pp. 77, 79)

[155] G D Saraiva et al. “Temperature-dependent Raman scattering studies on Na2Mo2O7 disodium dimolybdate”. *Journal of Raman Spectroscopy* 42.5 (2011), 1114–1119 (see pp. 77, 79)

[156] Jürgen Leyrer, Daniela Mey, and Helmut Knözinger. “Spreading behavior of molybdenum trioxide on alumina and silica: A Raman microscopy study”. *Journal of Catalysis* 124.2 (1990), 349–356 (see p. 83)

[157] J Leyrer, R Margraf, E Taglauer, and H Knözinger. “Solid-solid wetting and formation of monolayers in supported oxide systems”. *Surface Science* 201.3 (1988), 603–623 (see p. 84)

[158] S Gunther et al. “Transport mechanisms during spreading of MoO3 on Al2O3 supports investigated by photoelectron spectromicroscopy”. *The Journal of Chemical Physics* 112.12 (2000), 5440–5446 (see p. 84)

[159] Zhen Song et al. “Molecular Level Study of the Formation and the Spread of MoO3 on Au (111) by Scanning Tunneling Microscopy and X-ray Photoelectron Spectroscopy”. *Journal of the American Chemical Society* 125.26 (2003), 8059–8066 (see p. 84)

[160] Ladislaus Rybach and Fritz Laves. “Sodium diffusion experiments in quartz crystals”. *Geochimica et Cosmochimica acta* 31.4 (1967), 539–545 (see p. 89)

[161] Robert F RF Sippel. “Sodium self diffusion in natural minerals”. *Geochimica et Cosmochimica Acta* 27.1 (1963), 107–120 (see p. 89)

[162] O Jbara, J Cazaux, and P Trebbia. “Sodium diffusion in glasses during electron irradiation”. *Journal of Applied Physics* 78.2 (1995), 868–875 (see p. 89)

[163] GÜNTHER H FRISCHAT. “Sodium Diffusion in SiO2 Glass”. *Journal of the American Ceramic Society* 51.9 (1968), 528–530 (see p. 89)

[164] E K Kazenas et al. “Thermodynamics of sodium molybdate evaporation”. English. *Russian Metallurgy* 2010.5 (2010), 389–392 (see p. 89)

[165] C Julien, A Khelfa, O M Hussain, and G A Nazri. “Synthesis and characterization of flash-evaporated MoO3 thin films”. *Journal of Crystal Growth* 156.3 (1995), 235–244 (see p. 91)

[166] A Di Paola, L Palmisano, A M Venezia, and V Augugliaro. “Coupled Semiconductor Systems for Photocatalysis. Preparation and Characterization of Polycrystalline Mixed WO3/WS2 Powders”. *The Journal of Physical Chemistry B* 103.39 (1999), 8236–8244 (see p. 92)

[167] W J Schutte, J L De Boer, and F Jellinek. “Crystal structures of tungsten disulfide and diselenide”. *Journal of Solid State Chemistry* 70.2 (1987), 207–209 (see p. 93)

[168] D Yang and R F Frindt. “Li-intercalation and exfoliation of WS2”. *Journal of Physics and Chemistry of Solids* 57.6–8 (1996), 1113–1116 (see p. 93)

[169] Andrey N Enyashin et al. “New Route for Stabilization of 1T-WS2 and MoS2 Phases”. *The Journal of Physical Chemistry C* 115.50 (2011), 24586–24591 (see p. 93)

[170] R Coehoorn et al. “Electronic structure of MoSe2, MoS2, and WSe2. I. Band-structure calculations and photoelectron spectroscopy”. *Physical Review B* 35.12 (1987), 6195–6202 (see p. 93)

[171] C Ataca, H Şahin, and S Ciraci. "Stable, Single-Layer MX2 Transition-Metal Oxides and Dichalcogenides in a Honeycomb-Like Structure". *The Journal of Physical Chemistry C* 116.16 (2012), 8983–8999 (see pp. 93, 108, 110, 119)

[172] Karsten Albe and Andreas Klein. "Density-functional-theory calculations of electronic band structure of single-crystal and single-layer WS2". *Physical Review B* 66.7 (2002), 73413 (see p. 93)

[173] I Milosević, T Vuković, M Damnjanović, and B Nikolić. "Symmetry based properties of the transition metal dichalcogenide nanotubes". English. *The European Physical Journal B - Condensed Matter and Complex Systems* 17.4 (2000), 707–712 (see p. 93)

[174] Sumio Iijima. "Helical microtubules of graphitic carbon". *Nature* 354.6348 (1991), 56–58 (see p. 94)

[175] R Tenne, L Margulis, M Genut, and G Hodes. *Polyhedral and cylindrical structures of tungsten disulphide*. 1992 (see p. 94)

[176] C N R Rao and Manashi Nath. "Inorganic nanotubes". *Dalton Transactions* 1 (2003), 1–24 (see p. 94)

[177] E. Stoffels et al. "MoS2 nanoparticle formation in a low pressure environment". *Journal of Applied Physics* 86.6 (1999), 3442 (see p. 95)

[178] Xiao-Lin Li, Jian-Ping Ge, and Ya-Dong Li. "Atmospheric Pressure Chemical Vapor Deposition: An Alternative Route to Large-Scale MoS2 and WS2 Inorganic Fullerene-like Nanostructures and Nanoflowers". *Chemistry – A European Journal* 10.23 (2004), 6163–6171 (see p. 95)

[179] M Homyonfer et al. "Intercalation of Inorganic Fullerene-like Structures Yields Photosensitive Films and New Tips for Scanning Probe Microscopy". *Journal of the American Chemical Society* 119.11 (1997), 2693–2698 (see p. 95)

[180] R Tenne, M Homyonfer, and Y Feldman. "Nanoparticles of Layered Compounds with Hollow Cage Structures (Inorganic Fullerene-Like Structures)". *Chemistry of Materials* 10.11 (1998), 3225–3238 (see p. 95)

[181] G L Frey et al. "Optical-absorption spectra of inorganic fullerenelike MS2 (M=Mo, W)". *Physical Review B* 57.11 (1998), 6666–6671 (see p. 95)

[182] Gitti L Frey et al. "Raman and resonance Raman investigation of MoS2 nanoparticles". *Physical Review B* 60.4 (1999), 2883–2892 (see p. 95)

[183] A Rothschild, J Sloan, and R Tenne. “Growth of WS2 Nanotubes Phases”. *Journal of the American Chemical Society* 122.21 (2000), 5169–5179 (see p. 95)

[184] A Zak et al. “Growth Mechanism of MoS2 Fullerene-like Nanoparticles by Gas-Phase Synthesis”. *Journal of the American Chemical Society* 122.45 (2000), 11108–11116 (see p. 95)

[185] Y Feldman, V Lyakhovitskaya, and R Tenne. “Kinetics of Nested Inorganic Fullerene-like Nanoparticle Formation”. *Journal of the American Chemical Society* 120.17 (1998), 4176–4183 (see pp. 95, 116)

[186] A Margolin et al. “Study of the growth mechanism of WS2 nanotubes produced by a fluidized bed reactor”. *Journal of Materials Chemistry* 14.4 (2004), 617–624 (see p. 95)

[187] Y Feldman et al. “Bulk Synthesis of Inorganic Fullerene-like MS2 (M = Mo, W) from the Respective Trioxides and the Reaction Mechanism”. *Journal of the American Chemical Society* 118.23 (1996), 5362–5367 (see pp. 95, 116)

[188] T Tsirlina et al. “Synthesis and characterization of inorganic fullerene-like WSe2 material”. *Fullerene Science and Technology* 6.1 (1998), 157–165 (see p. 95)

[189] Y Q Zhu et al. “Morphology, structure and growth of WS2 nanotubes”. *Journal of Materials Chemistry* 10.11 (2000), 2570–2577 (see pp. 95, 96)

[190] X.F. Zhang et al. “Carbon nano-tubes; their formation process and observation by electron microscopy”. *Journal of Crystal Growth* 130.3-4 (1993), 368–382 (see p. 96)

[191] L MARGULIS, P DLUZEWSKI, Y FELDMAN, and R TENNE. “TEM study of chirality in MoS2 nanotubes”. *Journal of Microscopy* 181.1 (1996), 68–71 (see p. 96)

[192] Toshio Miyano, Masazumi Iwanishi, Chihiro Kaito, and Makoto Shiojiri. “High-Resolution Electron Microscopic Studies of CS Structure in Reduced WO3 Thin Crystals”. *Japanese Journal of Applied Physics* 22.Part 1, No. 5 (1983), pages (see p. 96)

[193] Gotthard Seifert et al. “On the electronic structure of WS2 nanotubes”. *Solid State Communications* 114.5 (2000), 245–248 (see p. 96)

[194] N Zibouche, A Kuc, and T Heine. “From layers to nanotubes: Transition metal disulfides TMS2”. English. *The European Physical Journal B* 85.1 (2012), 1–7 (see p. 96)

[195] Andrea Splendiani et al. “Emerging photoluminescence in monolayer MoS2”. *Nano letters* 10.4 (2010), 1271–5 (see p. 97)

[196] Ronan J Smith et al. “Large-Scale Exfoliation of Inorganic Layered Compounds in Aqueous Surfactant Solutions”. *Advanced Materials* 23.34 (2011), 3944–3948 (see p. 97)

[197] Changgu Lee et al. “Anomalous Lattice Vibrations of Single- and Few-Layer MoS2”. *ACS Nano* 4.5 (2010), 2695–2700 (see p. 97)

[198] Woo Y Lee, Theodore M Besmann, and Michael W Stott. “Preparation of MoS2 thin films by chemical vapor deposition”. 9.6 (1994) (see pp. 97, 102)

[199] I Endler et al. “Chemical vapour deposition of MoS2 coatings using the precursors MoCl5 and H2S”. *Surface and Coatings Technology* 120–121 (1999), 482–488 (see pp. 97, 102)

[200] A Ennaoui et al. “Preparation of textured and photoactive 2H-WS2 thin films by sulfurization of WO3”. *Thin Solid Films* 261.1–2 (1995), 124–131 (see p. 97)

[201] M Regula, C Ballif, M Remskar, and F Levy. “Crystallinity and texture promotion in WS2 thin films”. *Journal of Vacuum Science and Technology A: Vacuum, Surfaces, and Films* 15.4 (1997), 2323–2329 (see p. 97)

[202] M Regula, C Ballif, and F Lévy. “In situ TEM observation of nickel promoted WS2 thin-film crystallization”. *Journal of Crystal Growth* 193.1–2 (1998), 109–113 (see p. 98)

[203] Mariyappan Shanmugam, Tanesh Bansal, Chris A Durcan, and Bin Yu. “Schottky-barrier solar cell based on layered semiconductor tungsten disulfide nanofilm”. *Applied Physics Letters* 101.26 (2012), 263902–263905 (see pp. 98, 102)

[204] M. Genut, L. Margulis, R. Tenne, and G. Hodes. “Effect of substrate on growth of WS2 thin films”. *Thin Solid Films* 219.1-2 (1992), 30–36 (see p. 98)

[205] Th. Weber et al. “Basic Reaction Steps in the Sulfidation of Crystalline MoO3 to MoS2, As Studied by X-ray Photoelectron and Infrared Emission Spectroscopy”. *The Journal of Physical Chemistry* 100.33 (1996), 14144–14150 (see p. 98)

[206] Yi-Hsien Lee et al. “Synthesis of Large-Area MoS2 Atomic Layers with Chemical Vapor Deposition”. *Advanced Materials* 24.17 (2012), 2320–2325 (see pp. 98–100, 102)

[207] Keng-Ku Liu et al. “Growth of Large-Area and Highly Crystalline MoS2 Thin Layers on Insulating Substrates”. *Nano Letters* 12.3 (2012), 1538–1544 (see pp. 98, 102)

[208] Sina Najmaei et al. “Vapour phase growth and grain boundary structure of molybdenum disulphide atomic layers”. *Nat Mater* advance on (2013) (see pp. 98–100, 102)

[209] A J van der Vlies, R Prins, and Th. Weber. “Chemical Principles of the Sulfidation of Tungsten Oxides”. *The Journal of Physical Chemistry B* 106.36 (2002), 9277–9285 (see pp. 98, 99)

[210] A J van der Vlies et al. “Basic Reaction Steps in the Sulfidation of Crystalline Tungsten Oxides”. *The Journal of Physical Chemistry B* 106.13 (2002), 3449–3457 (see pp. 98, 99)

[211] Chunxiao Cong et al. “Synthesis and optical properties of large-area single-crystalline 2D semiconductor WS2 monolayer from chemical vapor deposition”. *Advanced Optical Materials* 2.2 (2014), 131–136. arXiv: `1312.1418` (see pp. 98, 101, 102, 107, 108)

[212] Namphung Peimyoo et al. “Nonblinking, intense two-dimensional light emitter: Monolayer WS 2 Triangles”. *ACS Nano* 7.12 (2013), 10985–10994 (see pp. 99, 101–103, 108, 118)

[213] Ayse Berkdemir et al. “Identification of individual and few layers of WS2 using Raman spectroscopy.” *Scientific reports* 3 (2013), 1755 (see pp. 99, 102, 108, 118, 120)

[214] A Molina-Sánchez and L Wirtz. “Phonons in single-layer and few-layer MoS2 and WS2”. *Physical Review B* 84.15 (2011), 155413 (see pp. 99, 105, 110, 118)

[215] Hualing Zeng et al. “Optical signature of symmetry variations and spin-valley coupling in atomically thin tungsten dichalcogenides”. *Sci. Rep.* 3 (2013), 1608 (see p. 99)

[216] Weijie Zhao et al. “Lattice dynamics in mono- and few-layer sheets of WS2 and WSe2”. *Nanoscale* (2013) (see pp. 99, 105, 106, 108)

[217] Yi-Hsien Lee et al. “Synthesis and Transfer of Single-Layer Transition Metal Disulfides on Diverse Surfaces”. *Nano Letters* 13.4 (2013), 1852–1857 (see pp. 99–102)

[218] Arend M van der Zande et al. “Grains and grain boundaries in highly crystalline monolayer molybdenum disulphide”. *Nat Mater* 12.6 (2013), 554–561 (see pp. 99, 100)

[219] Yu Zhang et al. "Controlled Growth of High-Quality Monolayer WS2 Layers on Sapphire and Imaging Its Grain Boundary". *ACS Nano* 7.10 (2013), 8963–8971 (see pp. 100–102)

[220] Jing-kai Huang et al. "Large-Area Aiming Synthesis of WSe2 Monolayers" (2013), 1–3. arXiv: `1304.7365` (see p. 101)

[221] Xi Ling et al. "Role of the Seeding Promoter in MoS2 Growth by Chemical Vapor Deposition". *Nano Letters* (2014) (see pp. 101, 102)

[222] Yongjie Zhan et al. "Large-area vapor-phase growth and characterization of MoS2 atomic layers on a SiO2 substrate." *Small (Weinheim an der Bergstrasse, Germany)* 8.7 (2012), 966–71 (see p. 102)

[223] Xinsheng Wang, Hongbin Feng, Yongmin Wu, and Liying Jiao. "Controlled Synthesis of Highly Crystalline MoS2 Flakes by Chemical Vapor Deposition". *Journal of the American Chemical Society* 135.14 (2013), 5304–5307 (see p. 102)

[224] Sanfeng Wu et al. "Vapor–Solid Growth of High Optical Quality MoS2 Monolayers with Near-Unity Valley Polarization". *ACS Nano* 7.3 (2013), 2768–2772 (see p. 102)

[225] John Mann et al. "Facile growth of monolayer MoS2 film areas on SiO2". English. *The European Physical Journal B* 86.5 (2013), 1–4 (see p. 102)

[226] Qingqing Ji et al. "Epitaxial Monolayer MoS2 on Mica with Novel Photoluminescence". *Nano Letters* (2013) (see p. 102)

[227] S Brunken, R Mientus, S Seeger, and K Ellmer. "The mechanism of nickel sulfide induced rapid crystallization of highly textured tungsten disulfide (WS2) thin films: An in situ real-time diffraction study". *Journal of Applied Physics* 103.6 (2008), 63501–63506 (see p. 102)

[228] Humberto R Gutiérrez et al. "Extraordinary Room-Temperature Photoluminescence in Triangular WS2 Monolayers." *Nano letters* (2012), 1–8 (see p. 102)

[229] Ana Laura Elías et al. "Controlled Synthesis and Transfer of Large-Area WS2 Sheets: From Single Layer to Few Layers." *ACS nano* Xx (2013) (see p. 102)

[230] Francesco Bonaccorso, Ping-Heng Tan, and Andrea C Ferrari. "Multiwall Nanotubes, Multilayers, and Hybrid Nanostructures: New Frontiers for Technology and Raman Spectroscopy". *ACS Nano* 7.3 (2013), 1838–1844 (see p. 103)

[231] Dai-Ming Tang et al. "Revealing the Anomalous Tensile Properties of WS2 Nanotubes by in Situ Transmission Electron Microscopy". *Nano Letters* 13.3 (2013), 1034–1040 (see p. 103)

[232] AR Beal and WY Liang. “Excitons in 2H-WSe2 and 3R-WS2”. *Journal of Physics C: Solid State Physics* 2459 (1976) (see p. 103)

[233] T J Wieting and J L Verble. “Infrared and Raman Studies of Long-Wavelength Optical Phonons in Hexagonal MoS2”. *Physical Review B* 3.12 (1971), 4286–4292 (see pp. 104, 105)

[234] X. Zhang et al. “Raman spectroscopy of shear and layer breathing modes in multilayer MoS2”. *Physical Review B* 87.11 (2013), 115413 (see pp. 104, 105)

[235] Mahdi Ghorbani-Asl et al. “Electromechanics in MoS2 and WS2: nanotubes vs. monolayers”. *Sci. Rep.* 3 (2013) (see pp. 106, 109)

[236] A M Stacy and D T Hodul. “Raman spectra of IVB and VIB transition metal disulfides using laser energies near the absorption edges”. *Journal of Physics and Chemistry of Solids* 46.4 (1985), 405–409 (see pp. 105, 118)

[237] C Sourisseau, F Cruege, M Fouassier, and M Alba. “Second-order Raman effects, inelastic neutron scattering and lattice dynamics in 2H-WS2”. *Chemical Physics* 150.2 (1991), 281–293 (see pp. 105–107, 110)

[238] J-W. Chung et al. “Raman scattering and high resolution electron microscopy studies of metal-organic chemical vapor deposition-tungsten disulfide thin films”. *Thin Solid Films* 335.1–2 (1998), 106–111 (see p. 106)

[239] G L Frey et al. “Optical Properties of MS2 (M = Mo, W) Inorganic Fullerenelike and Nanotube Material Optical Absorption and Resonance Raman Measurements”. *Journal of Materials Research* 13.09 (1998), 2412–2417 (see pp. 107, 109)

[240] Matthias Staiger et al. “Excitonic resonances in WS2 nanotubes”. *Physical Review B* 86.16 (2012), 165423 (see pp. 107, 110, 118, 119)

[241] Michele Buscema, Gary A Steele, Herre S. J. van der Zant, and Andres Castellanos-Gomez. “The effect of the substrate on the Raman and photoluminescence emission of single layer MoS2” (2013), 10. arXiv: `1311.3869` (see p. 108)

[242] Thripuranthaka M and Dattatray J Late. “Temperature Dependent Phonon Shifts in Single-Layer WS2”. *ACS Applied Materials and Interfaces* 6.2 (2013), 1158–1163 (see p. 108)

[243] Edib Dobardžić, Borivoje Dakić, Milan Damnjanović, and Ivanka Milošević. “Zero m phonons in MoS2 nanotubes”. *Physical Review B* 71.12 (2005), 121405 (see p. 108)

[244] E Dobardžić, I Milošević, B Dakić, and M Damnjanović. “Raman and infrared-active modes in MS2 nanotubes (M=Mo,W)”. *Physical Review B* 74.3 (2006), 33403 (see p. 109)

[245] Matthias Krause et al. “Diameter and Morphology Dependent Raman Signatures of WS2 Nanostructures”. *ChemPhysChem* 10.13 (2009), 2221–2225 (see pp. 110, 119)

[246] Matthias Krause et al. “Diameter dependent Raman scattering of WS2 nanotubes”. *physica status solidi (b)* 246.11-12 (2009), 2786–2789 (see pp. 110, 119)

[247] P M Rafailov et al. “Orientation dependence of the polarizability of an individual WS2 nanotube by resonant Raman spectroscopy”. *Physical Review B* 72.20 (2005), 205436 (see p. 111)

[248] Marko Viršek et al. “Raman scattering of the MoS2 and WS2 single nanotubes”. *Surface Science* 601.13 (2007), 2868–2872 (see p. 111)

[249] A ZAK et al. “INSIGHT INTO THE GROWTH MECHANISM OF WS2 NANOTUBES IN THE SCALED-UP FLUIDIZED-BED REACTOR”. *Nano* 04.02 (2009), 91–98 (see p. 116)

[250] T Sekine et al. “Raman scattering in layered compound 2H-WS2”. *Solid State Communications* 35.4 (1980), 371–373 (see p. 118)

[251] Song-Lin Li et al. “Quantitative Raman Spectrum and Reliable Thickness Identification for Atomic Layers on Insulating Substrates”. *ACS Nano* 6.8 (2012), 7381–7388 (see p. 122)

[252] R Azimirad, O Akhavan, and A Z Moshfegh. “Simple Method to Synthesize NaxWO3 Nanorods and Nanobelts”. *The Journal of Physical Chemistry C* 113.30 (2009), 13098–13102 (see p. 128)

[253] Meirav Mann, Gennady Shter, George Reisner, and Gideon Grader. “Synthesis of tungsten bronze powder and determination of its composition”. *Journal of Materials Science* 42.3 (2007), 1010–1018 (see p. 130)